공학석사학위논문

Bayesian Model of Low-Temperature Fatigue Crack Growth Rate of Alloy 182 Dissimilar Metal Weld

이종 금속 용접부 합금 182의 저온 피로 균열 성장 속도 베이지안 모델 연구

2016년 2월

서울대학교 대학원

에너지시스템공학부

최 산 해

Bayesian Model of Low-Temperature Fatigue Crack Growth Rate of Alloy 182 Dissimilar Metal Weld

지도 교수 황 일 순

이 논문을 공학석사학위논문으로 제출함
2015년 10월

서울대학교 대학원
에너지시스템공학부
최 산 해

최산해의 공학석사학위논문을 인준함
2015년 12월

위 원 장 _____ 권 동 일 _____ (인)

부위원장 _____ 황 일 순 _____ (인)

위 원 _____ 장 창 희 _____ (인)

Abstract

Bayesian Model of Low-Temperature Fatigue Crack Growth Rate of Alloy 182 Dissimilar Metal Weld

Sanhae Choi
Department of Energy Systems Engineering
The Graduate School
Seoul National University

In the next 10 years, more than half of the world's nuclear power plants (NPPs) will exceed their design life of 40 years. Therefore, aging management of NPPs will be one of the most important issues in the nuclear industry. The integrity of the structural materials of NPPs is evaluated by Paris' law fitted deterministically from fatigue crack growth rate data based on ASME Boiler and Pressure Vessel Code Section XI during in-service inspections (ISIs).

To reduce costs, dissimilar metal welds are widely used between pressure vessels made of low-alloy steel and pipes made of stainless steel. The mechanical properties of the welded metals depend on the welding conditions and the NPP environment. In

particular, cracks have been detected in alloy 182 dissimilar metal welds in the Davis-Besse and V. C. Summer NPPs. Laboratory tests performed in low-temperature water and the dissolved hydrogen showed that the fracture toughness of this weld was drastically decreased because of hydrogen embrittlement.

In this study, alloy 182 dissimilar metal weld referred to as a pressurizer surge line nozzle used in the Kori NPP Unit 1 was manufactured. Fatigue crack growth rate test specimens were made using electrical discharge machining (EDM) wire cutting. The constant load fatigue crack growth test of the specimens was performed at 25℃ air and in low-temperature water at 54℃. The hydrogen concentration was 30 cc H_2/kg H_2O at atmospheric pressure, which is similar to the NPP shutdown conditions. Through this experiment, it was found that the fatigue crack growth rate increased as a result of hydrogen embrittlement, and the Paris law constants were obtained with this data.

Next, constant stress intensity factor range (ΔK) tests under shutdown conditions were performed to obtain the fatigue crack growth rates. Normal distribution of the differences between this data and the fatigue crack growth rate determined by Paris' law was assumed in order to obtain the likelihood of each constant value. Normal distribution was assumed in order to use Bayesian inference for the uncertainties of the Paris law constants, C and m. C and m were sampled using a Monte Carlo simulation with each distribution. With each sampled constant value, the likelihood and probability

density could be calculated. Posterior probability density was calculated by multiplying the normalized likelihood and probability density of each constant value. Therefore, the posterior distribution confirmed that the standard deviations of the constant values were greatly reduced. In other words, if the likelihood can be calculated using sampled constant values and several constant ΔK tests in cases where the data on the fatigue crack growth rate is limited, the uncertainties can be decreased by updating the Paris law constants using Bayesian inference considering the welding conditions and the surrounding environment.

Finally, it was confirmed that the fatigue crack growth rate increased upon reducing the loading frequency to one-tenth because a low-temperature water environment had a greater influence on the material corrosion.

Through this study, updated Paris law constants can be obtained using field data and carrying out constant ΔK tests in the laboratory under the same environment. If a probabilistic method using Bayesian inference is included in the structural integrity evaluation of nuclear power plants, the evaluation of the fatigue crack growth rate would be more accurate.

Keywords: Alloy 182 dissimilar metal weld, Fatigue crack growth rate, Hydrogen embrittlement, Paris' law, Bayesian inference, Monte Carlo simulation
Student Number: 2014-20531

Table of Contents

List of Tables

List of Figures

Chapter 1 Introduction

There are 441 operational nuclear reactors in the world. The ages of the reactors are shown in Figure 1.1 [1]. The design life of nuclear power plants (NPPs) is 30 or 40 years. Therefore, in 10 years, approximately 250 NPPs will have been in operation for more than 40 years. Thus, the degradation of NPPs will be more important than ever.

To solve this problem, the reliability of the structural materials of NPPs is evaluated by a deterministically derived model named Paris' law, in accordance with ASME Boiler and Pressure Vessel Code Section XI fatigue crack growth data during in-service inspections (ISIs). Figure 1.2 shows the fatigue crack growth behavior of carbon and low-alloy ferritic steels exposed to air and water environments and stainless steel exposed to an air environment [2].

Alloy 182 is nickel-based alloy. It has a coefficient of thermal expansion between that of the low-alloy ferritic steel and austenitic stainless steel. It also prevents carbon diffusion from a low-alloy steel (LAS) to stainless steel (SS) [3]. Therefore, pressure vessels of pressurized water reactor (PWR) NPPs in South Korea are mostly made of LAS, whereas the pipes are of SS or carbon steel [4]. Thus, alloy 182 is widely used as a dissimilar metal weld that connects LAS and SS. Dissimilar metal welds are joints between two different types of metals, and thus they may have more mechanical defects than welds between similar metals. However, dissimilar metal welds are used extensively in NPPs because of corrosion and the economic feasibility of such welds.

However, cracks of alloy 182 dissimilar metal welds have been

detected in the J-groove weld region of the Davis-Besse reactor pressure vessel head and in the V. C. Summer hot-leg nozzle-to-pipe weld in the reactor coolant system (RCS), as shown in Figure 1.3. Also, reliability assessments of NPP structural materials are required because of the Fukushima accident [5].

With alloy 182 welds, it is known that hydrogen-induced cracks occur in low-temperature (<150℃) environments, an environment that imitates an NPP shutdown [6].

In this study, a low-temperature water environment containing dissolved hydrogen was created and constant load and constant stress intensity factor range (ΔK) tests were performed. The constant load test was used to check the fatigue crack growth behavior of alloy 182 welds. The results were fitted to the Paris law model to obtain the Paris law constants.

There are uncertainties because the Paris law constants are derived deterministically from experimental data. Therefore, with the constant ΔK test, Bayesian updating was carrying out probabilistically to reduce the uncertainty of the Paris law constants.

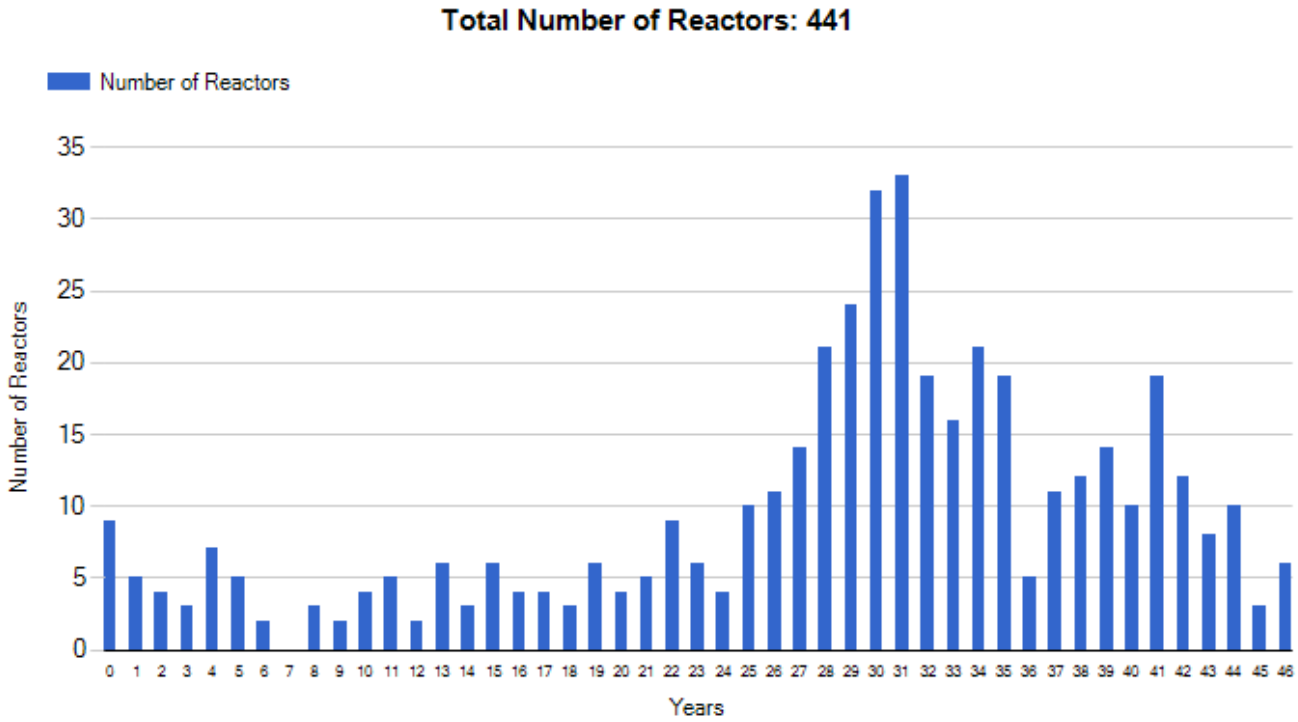

(Note: Age of reactor is determined by its first grid connection. Reactors connected in the current year are assigned an age of 0 years.)

Figure 1.1 Operational reactors by age [1].

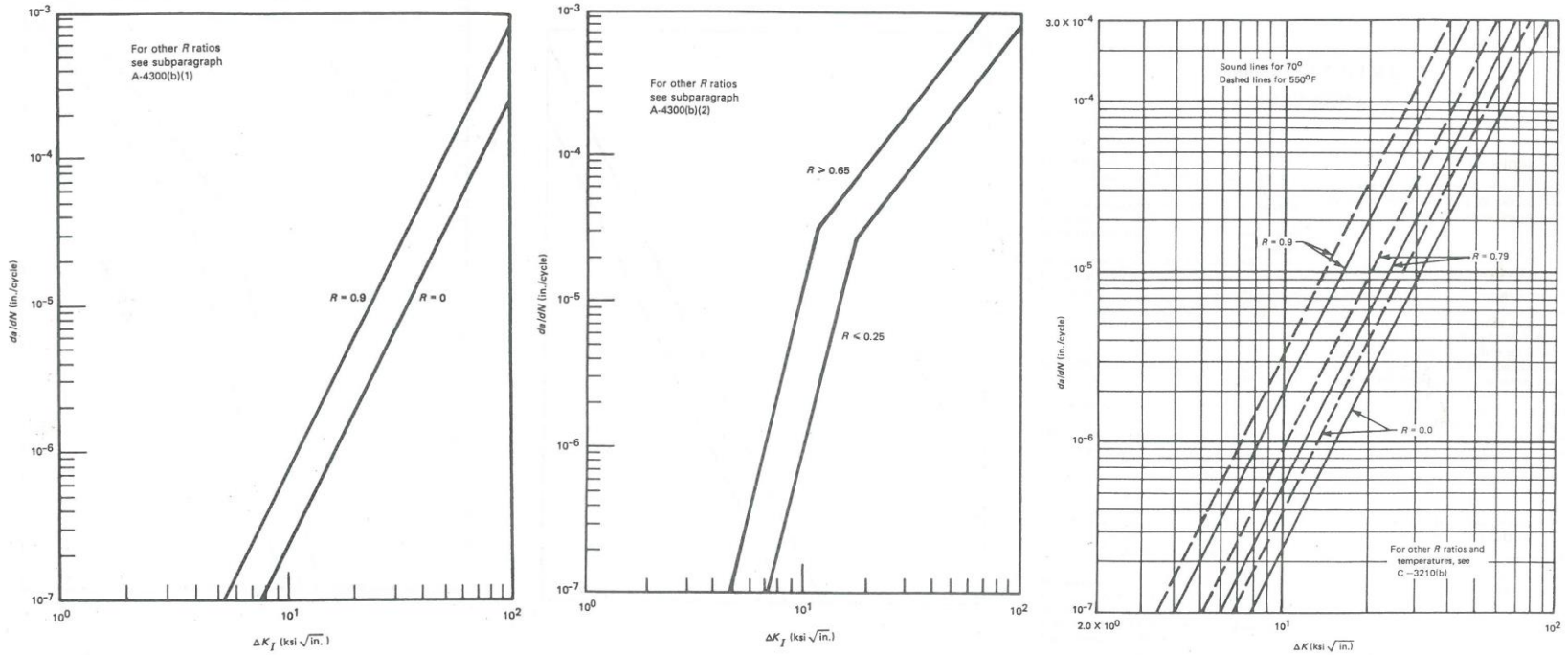

(a) (b) (c)

Figure 1.2 Reference fatigue crack growth curves for (a) carbon and low-alloy ferritic steels exposed to air environments (subsurface flaws), (b) carbon and low-alloy ferritic steels exposed to water environments, and (c) austenitic stainless steels in air environments [2].

(a)

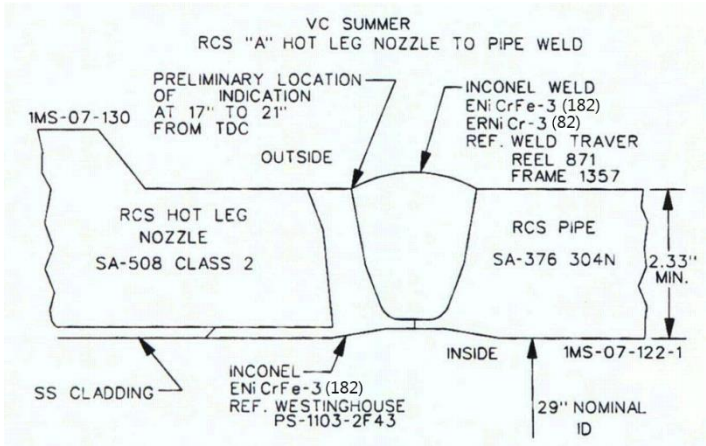

(b)

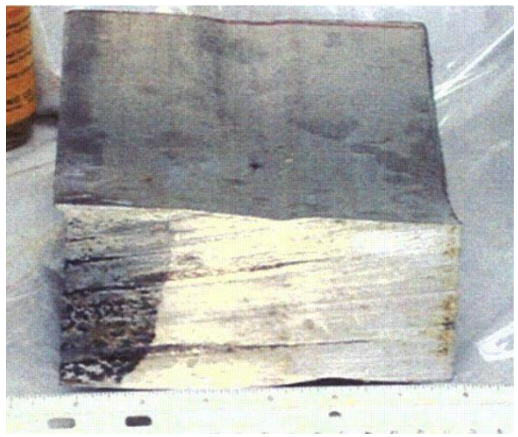

(c)

Figure 1.3 (a) Photograph of the Davis–Besse reactor pressure vessel head sample with J-groove weld from nozzle #11, (b) schematic diagram of the V. C. Summer hot-leg nozzle-to-pipe weld in the RCS, and (c) photograph of the V.C. Summer spool piece [5].

Chapter 2 Literature Review

2.1 Fatigue

2.1.1 Fatigue parameters

Fatigue is defined as "a degradation of mechanical properties leading to failure of a material or component under cyclic loading" [7]. The parameters used in the fatigue test are shown in Figure 2.1. Their equations are as follows.

$$\text{Cyclic stress range} \equiv \Delta\sigma = \sigma_{\max} - \sigma_{\min} \tag{2.1}$$

$$\text{Cyclic stress amplitude} \equiv \sigma_a = \frac{\sigma_{\max} - \sigma_{\min}}{2} \tag{2.2}$$

$$\text{Mean stress} \equiv \frac{\sigma_{\max} + \sigma_{\min}}{2} \tag{2.3}$$

$$\text{Stress ratio} \equiv R = \frac{\sigma_{\min}}{\sigma_{\max}} \tag{2.4}$$

2.1.2 Mechanisms of fatigue

Fatigue cracks are generated in singular points or discontinuities present in the materials. Discontinuities exist in the materials or on the surface, whereas singularities are present structurally as inclusions or second-phase particles or geometrically as scratches or steps. Surface singularities are produced in the form of intrusions and extrusions by cyclic deformation. These are called persistent slip bands (PSBs). These

PSBs move dislocations, whereas intrusions and extrusions at the surface create slip bands, as shown in Figure 2.2. Inclusions, second-phase particles, and grain boundaries are normally the dominant nucleation sites in materials, as shown in Figure 2.3 [7].

Crack growth occurs as follows. First, several cracks are generated on the surface, and these cracks propagate along the crystallographic slip planes, as shown in Figure 2.4. In stage I, it is difficult to know whether cracks will propagates as the crack growth rate is less than a few micrometers per cycle [7].

In stage II, cracks are generated in the slip bands on the surface. The crack growth rate is a few tens of millimeters per cycle and the crack growth direction is perpendicular to the direction of the tensile stress, mode I. Striation markings can be detected in this stage, as shown in Figure 2.5. In the figure, striation intervals increase from the early stage to the late stage. There is a local plastic deformation zone at the crack tip because of the stress intensity at the crack tip [7].

The plastic zone size increases with increasing crack growth. When the plastic zone size is more than 25% of the width or the thickness of the specimen, stage III starts. The cracks grow at a faster rate and the direction of the crack growth is perpendicular to the direction of tensile stress. The fracture surface also shows striation markings [7].

It is easy to think of each striation in one cycle but striation actually refers to the crack front position in each cycle. Therefore, there is a one-to-one relationship between striation spacing that means macroscopic growth rate and the stress intensity factor range (ΔK) [7].

In the high stress intensity factor range (ΔK), the striations are less important to the overall crack growth rate. At this time, fatigue

crack growth follows a plastic blunting mechanism. In this model, blunting and sharpening of the crack tip occur repeatedly. As shown in Figure 2.6(b), plastic strain on the crack tip leads to localized slip on the maximum shear plane at the tensile load. This is maximized, as shown in Figure 2.6(c), and the compressive cycle starts as shown in Figure 2.6(d). In Figure 2.6(e), maximum compressive load is applied. At this time, the new surface generated by the tensile part is not completely healed. However, it is known that most of the slips made under compressive load create many new slip planes. The crack tip assumes a bent form called an "ear". It is important to note that the absence of striations does not always confirm that it is not under cyclic loading [7].

2.1.3 The Paris law model

Paris found that log-scale plots of fatigue crack growth rate and the stress intensity factor range under cyclic conditions show a linear relationship in region II, as shown in Figure 2.7. He therefore proposed the following empirical formula, called Paris law model [7]:

$$\frac{da}{dN} = C(\Delta K)^m \tag{2.5}$$

where a is the crack length (mm), N is the number of cycles (cycle), ΔK is the stress intensity factor range ($\mathrm{MPa}\sqrt{m}$), and C and m are constants that depend on the material, environment, and test conditions (such as R, temperature, waveform, etc.).

The fatigue crack growth behavior in air of the alloy 182 weld used in this study is shown in Figure 2.8 [8]. Also, equation (2.6)

shows the calculation for the Paris law model of alloys 82, 182, 52, and 152 in air [9].

$$\frac{da}{dN} = C_{Niweld}(1-0.82R)^{-2.2}(\Delta K)^{4.1}$$
$$C_{Niweld} = 8.659\times10^{-14} - (5.272\times10^{-17})T + (2.129\times10^{-18})T^2 - (1.965\times10^{-20})T^3 + (6.038\times10^{-23})T^4 \quad (2.6)$$

where da/dN is the fatigue crack growth rate (mm/cycle), C_{Niweld} is a constant, R is the stress ratio, ΔK is the stress intensity factor range ($\mathrm{MPa}\sqrt{m}$), and T is the temperature (℃). Figure 2.9 was drawn based on this equation with R = 0.1 and T = 25℃, which is one of the experimental conditions.

2.2 Low-Temperature Crack Propagation

Low-temperature crack propagation (LTCP), which is a form of hydrogen embrittlement, has not been found in commercial NPPs yet. However, it was confirmed in laboratory tests that LTCP can cause severe degradation of the fracture resistance of certain nickel-based alloys under specific conditions [6].

This phenomenon may occur when certain nickel-based alloys are exposed to water, which contains dissolved hydrogen at low temperatures below 150℃. This condition exists when a PWR NPP is being shut down by decreasing the water temperature. The affected alloys ranked by decreasing susceptibility are X-750, 82 and 182, 52 and 152, 690, and 600. It was found that fracture toughness of these alloys increased as the water temperature increased and the hydrogen concentration in water decreased [6].

Fracture toughness can be greatly reduced, as shown in Figure 2.10, as the dissolved hydrogen concentration increases [10].

It was found that the water temperature is 54℃ and hydrogen concentration is 30 cc H_2/kg H_2O at PWR shutdown conditions. Therefore, it was confirmed that there is a possibility of generating an LTCP when an NPP shuts down [11].

2.3 Bayesian Inference and Monte Carlo Simulation

Bayesian inference is a method of analysis that combines knowledge gained prior to an experiment with subsequent experimental data. If the prior knowledge can be represented statistically, the uncertainties of such knowledge can be expressed as a distribution. Therefore, prior information distribution can be updated with any new information using Bayesian inference [12].

Bayesian statistics provide a method of updating the uncertainties. When using Bayesian statistics, data should be assumed by a distribution belonging to a known parametric family. By assuming proper distribution, it could be said that this method has validity [12].

The Bayesian approach merges information from two sources: (1) prior knowledge generated by theory and experiment and (2) likelihood functions contain information of the data. Basically, the prior distribution represents our initial understanding; the information in the data can be expressed in a likelihood function. Combining prior distribution and likelihood functions, posterior distribution can be obtained. This distribution represents the revised knowledge [12].

Bayes' rule can be expressed as a conditional probability as per the following equation (2.7) [13]:

$$p(\theta \mid y) = \frac{p(\theta \bigcap y)}{p(y)} = \frac{p(y \mid \theta) p(\theta)}{\int p(y \mid \theta) p(\theta) d\theta} \propto p(y \mid \theta) p(\theta) \tag{2.7}$$

where $p(\theta|\, y)$ is the posterior distribution, $p(y|\, \theta)$ is the likelihood, which is the probability of data y given our prior beliefs, and $p(\theta)$ is the prior distribution. Because $p(y)$ (which is the likelihood accumulated over all possible prior values) is independent of θ, we can express the posterior distribution as proportional ($\propto$) to $p(y|\, \theta)\, p(\theta)$ [12].

Using Monte Carlo simulation, the value of any continuous distribution can be found through random sampling. A random variable ξ between a < x < b can be obtained from a probability density function (PDF) of $p(x)$. Then this ξ value can be obtained from the following equation (2.8) [14].

$$\int_a^{\xi} p(x) dx = \gamma \tag{2.8}$$

In other words, if we can get a consecutive value of γ, the corresponding value of ξ can be obtained using equation (2.8), as shown in Figure 2.11. Therefore, if the cumulative distribution function (CDF) that is integrating the PDF is y, the value of y can be obtained by the following equation (2.9) [14]:

$$y = \int_a^{x} p(x) dx \tag{2.9}$$

Thus, the method for random sampling of the values of the PDF is as follows. First, values of γ between 0 < y < 1 are obtained by using uniform distributed random sampling. This γ value is then put into the y−axis of the CDF to obtain the corresponding ξ value.

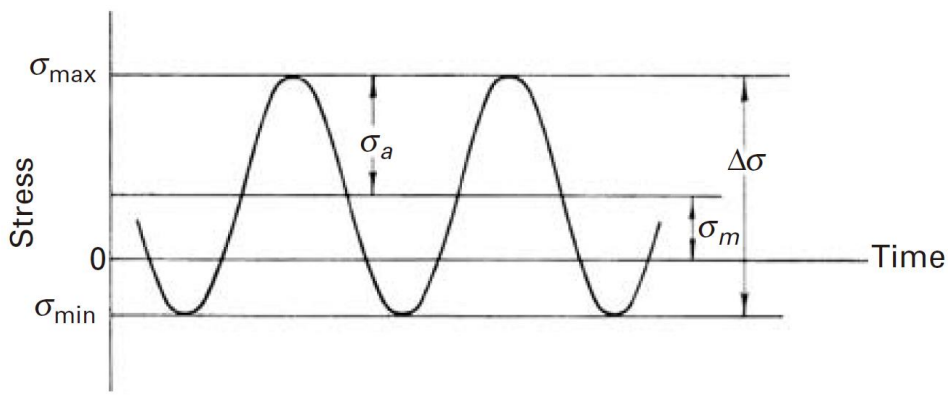

Figure 2.1 Fatigue parameters [7].

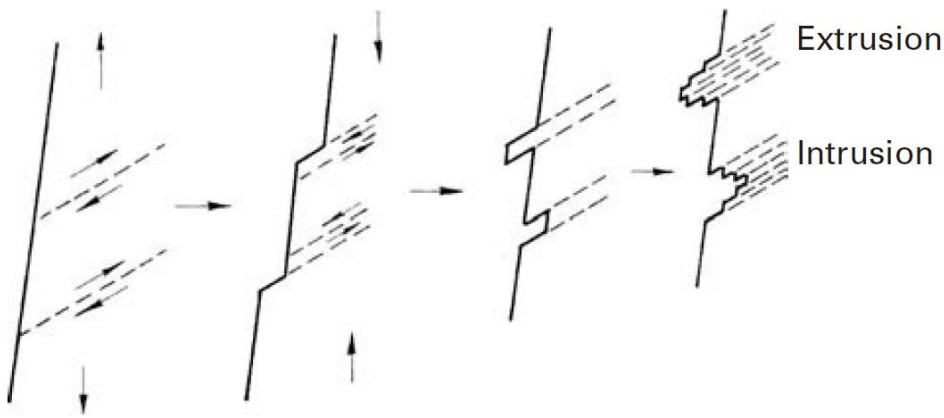

Figure 2.2 Fatigue crack nucleation at slip bands [7].

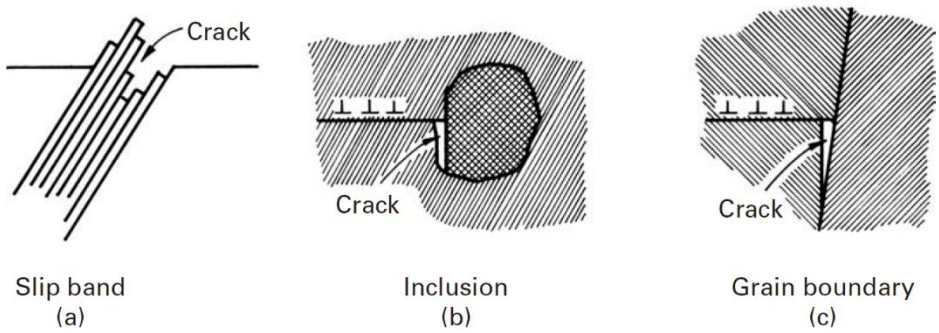

Figure 2.3 Some mechanisms of fatigue crack nucleation [7].

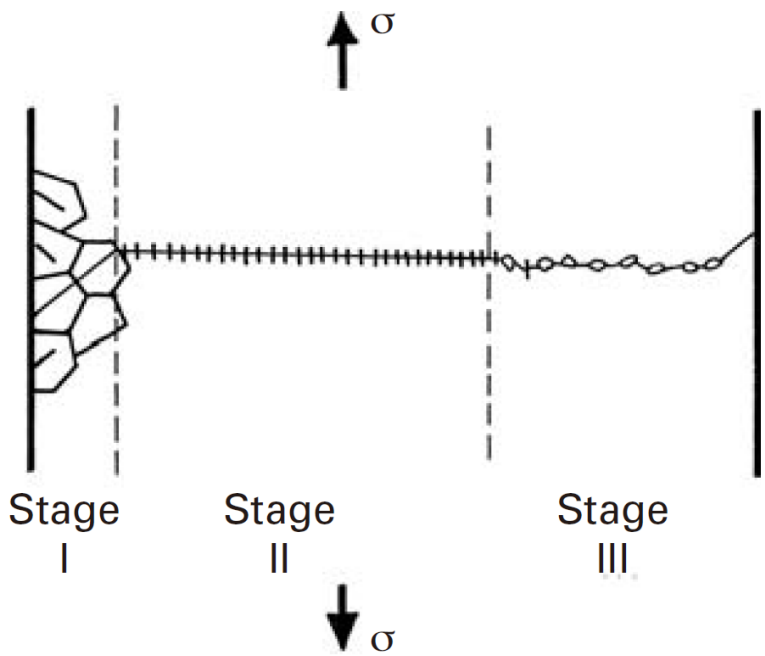

Figure 2.4 Stages I, II, and III of fatigue crack propagation [7].

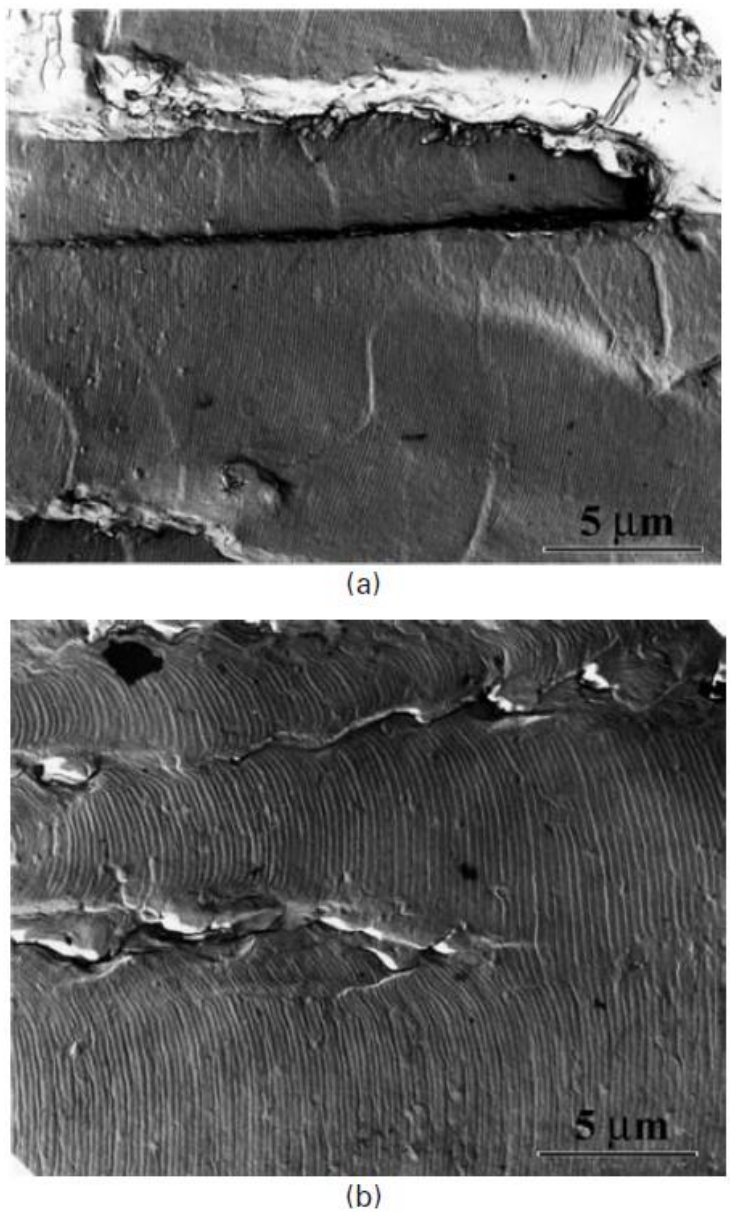

Figure 2.5 Fatigue striations in 2014-T6 aluminum alloy. Two-stage carbon replica viewed in TEM: (a) early stage and (b) late stage [7].

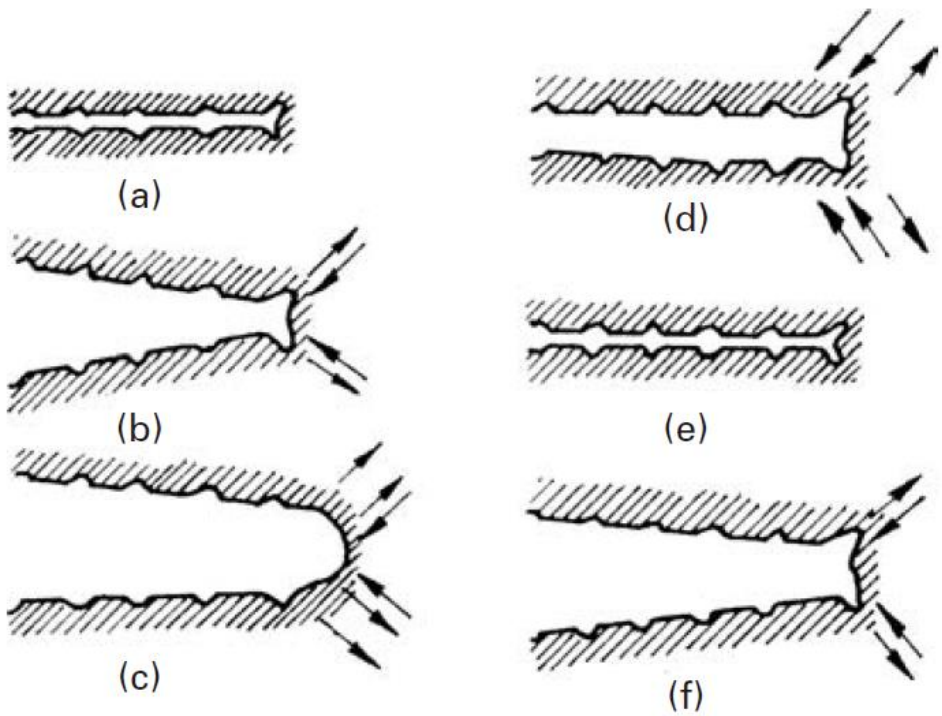

Figure 2.6 Fatigue crack growth by a plastic blunting mechanism: (a) zero load, (b) small tensile load, (c) maximum tensile load, (d) small compressive load, (e) maximum compressive load, and (f) small tensile load. The loading axis is vertical [7].

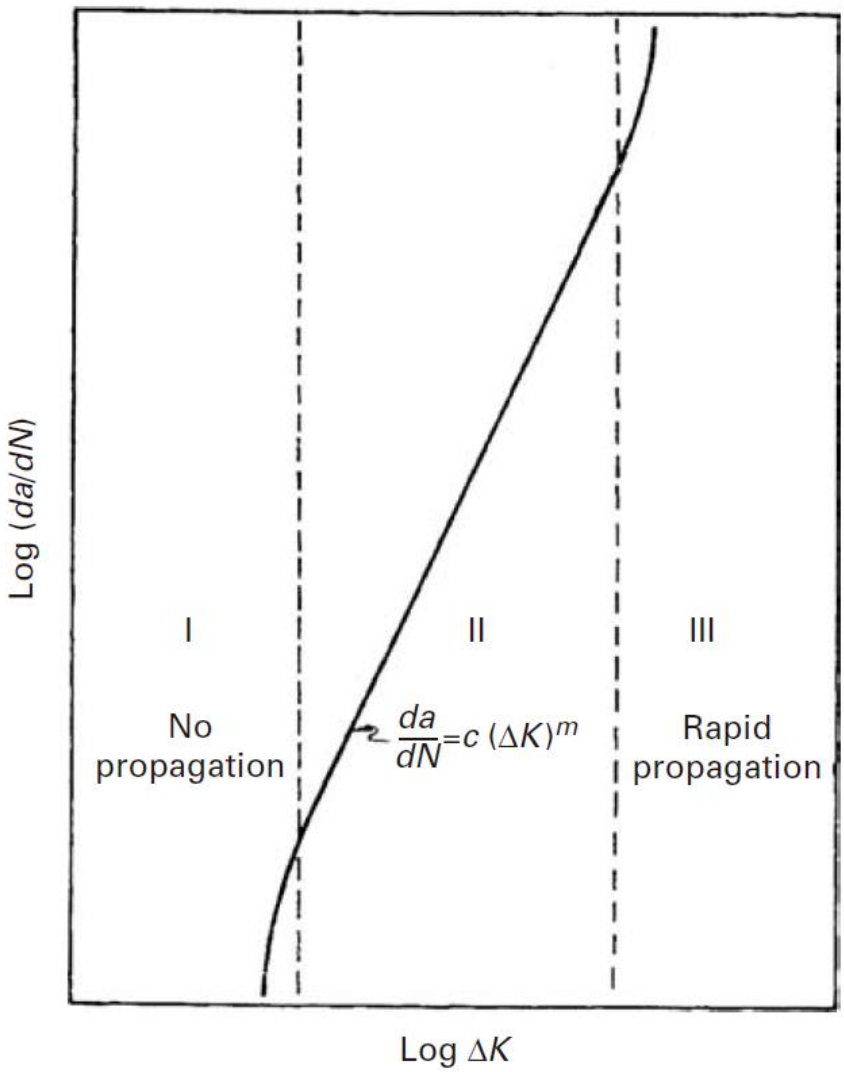

Figure 2.7 Schematic of fatigue crack growth rate (*da/dN*) versus stress intensity factor range (ΔK) [7].

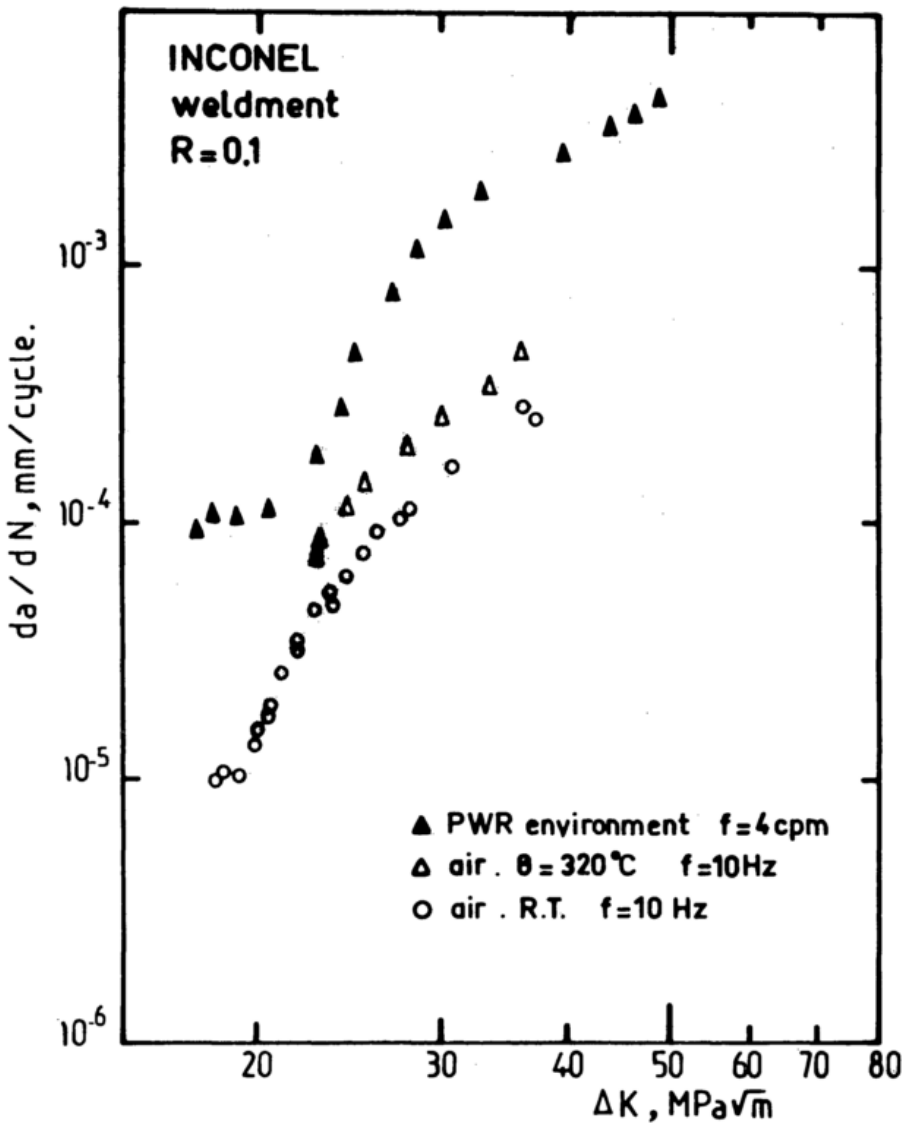

Figure 2.8 Schematic of crack propagation rate (*da/dN*) versus stress intensity factor range (ΔK) of alloy 182 weld [8].

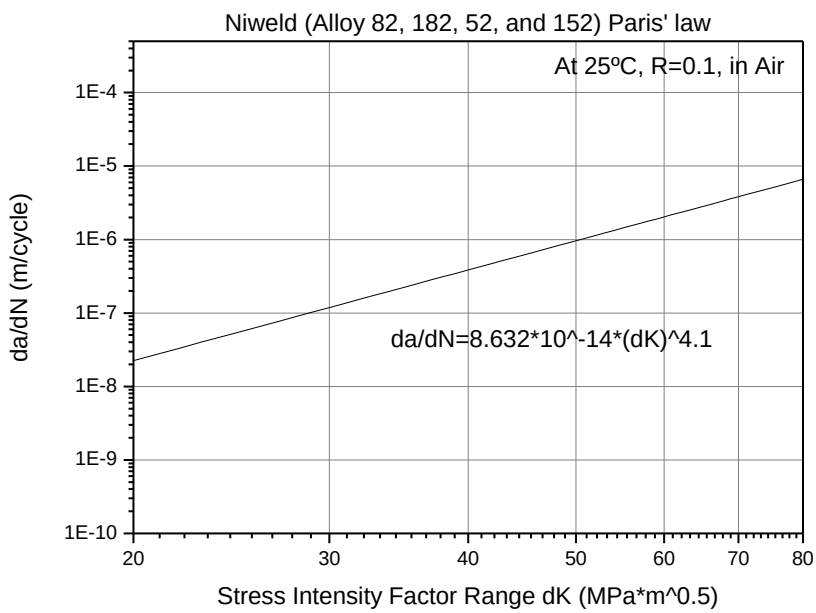

Figure 2.9 Paris' law for alloys 82, 182, 52, and 152 in air.

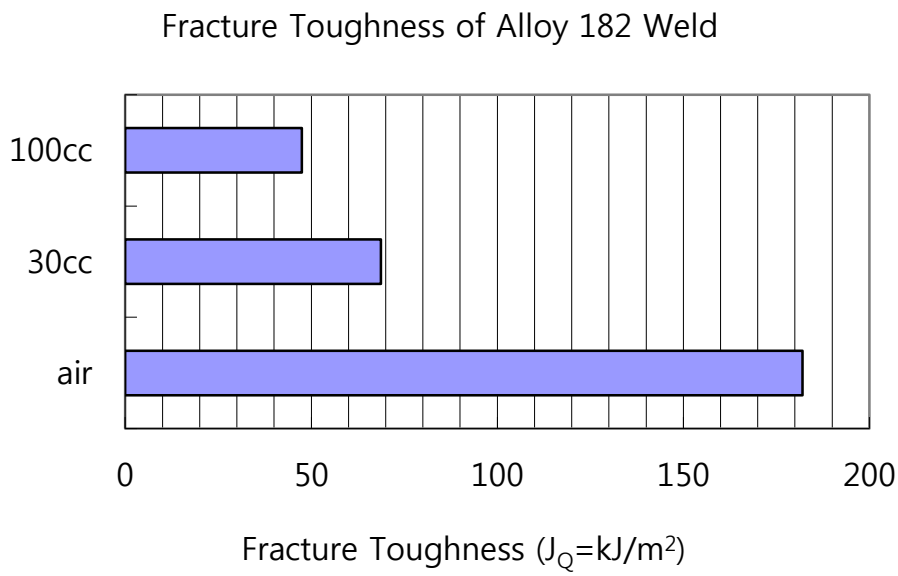

Figure 2.10 Average fracture toughness (J_Q) values for alloy 182 weld tested in 55℃ water (200 ppm H_3BO_3 and 2.1 ppm LiOH) with hydrogen contents of 100 and 30 cc H_2/kg H_2O [10].

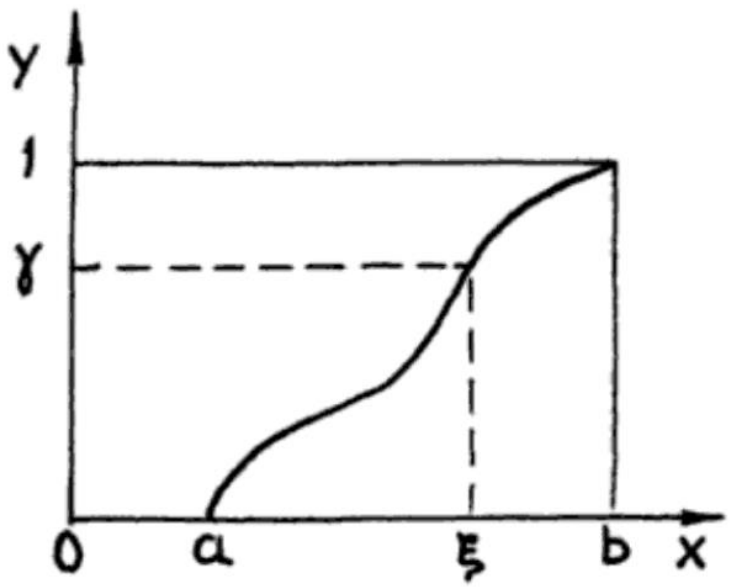

Figure 2.11 The function $y = \int_a^x p(x)dx$ for modeling of a continuous random variable [14].

Chapter 3 Rationale and Approach

3.1 Problem Statement

Alloy 182 is widely used as a dissimilar metal weld material between pressure vessels fabricated with LAS and high-temperature piping fabricated with SS [15]. In particular, the fracture toughness of alloy 182 welds was found to be drastically reduced by hydrogen embrittlement in a low-temperature water environment in a laboratory-scale experiment [6].

Cracks in alloy 182 welds have been detected in the Davis-Besse reactor pressure vessel head and the V. C. Summer hot-leg nozzle-to-pipe weld. Therefore, accurate assessment of the fatigue of alloy 182 welds is required [5].

Structural integrity is evaluated by fatigue crack growth curves during in-service inspection in accordance with ASME Boiler and Pressure Vessel Code Section XI [2]. Curves that are suitable for South Korean NPPs are required, especially since the mechanical properties of the welding region are likely to vary according to the welding conditions and the surrounding environment. Therefore, a way to reduce the uncertainty in the constants of the Paris law model with a stochastic method is needed.

3.2 Goals

There are two main goals of this study. First, to investigate the effect of hydrogen embrittlement on the fatigue crack growth behavior of alloy 182 dissimilar metal welds in a low-temperature water environment with an applied potential as compared to the

fatigue crack growth behavior in air at room temperature. Second, to reduce the uncertainty of fatigue crack growth rate model constants (Paris law constants) of alloy 182 welds in a low-temperature water environment probabilistically using Bayesian inference.

In other words, the most important goal is to update the Paris law constants using Bayesian inference to evaluate the reliability of alloy 182 welds under NPP shutdown conditions. Also, because lowering the fatigue loading frequency increases corrosion, the fatigue crack growth behavior will be checked in NPP shutdown conditions.

3.3 Approach

First, a dissimilar metal weld using welding alloy 182 was made between a low-alloy steel and stainless steel. A single-edge notched (SEN) specimen was fabricated by electrical discharge machining (EDM) wire cutting to eliminate thermal effect [16-19].

To measure crack growth optically with a travelling microscope, the specimen's centerline region was polished. The crack propagation length was measured using the direct current potential drop (DCPD) method and the travelling microscope. The test was performed under constant load fatigue in air at 25℃. With this fatigue crack growth rate data, the Paris law constants were obtained. To simulate NPP shutdown conditions, cathodic polarization, in which the dissolved hydrogen concentration was 30 cc H_2/kg H_2O and the water temperature was 54℃, was used. Obtaining the Paris law constants in low-temperature water was carried out the same way as in air.

Given the uncertainty of whether the constants obtained from the Paris' law follow a normal (Gaussian) distribution, the Paris law constants can be expressed by a function, and this distribution is the prior distribution. A constant ΔK test is then carried out to obtain a likelihood distribution. Random sampling of the values is done by the cumulative distribution function of the Paris law constants using Monte Carlo simulation. The posterior distribution can be solved by multiplying each value of the normalized prior probability density and normalized likelihood. Bayesian updating of the Paris law constants can be done with this method. These updated constants can be updated continuously using new constant ΔK test data. This process is repeated until the standard deviation (STD) is acceptable. A summary of this process is shown in Figure 3.1. After Bayesian updating, the test is carried out at a low loading frequency to determine the effect of corrosion.

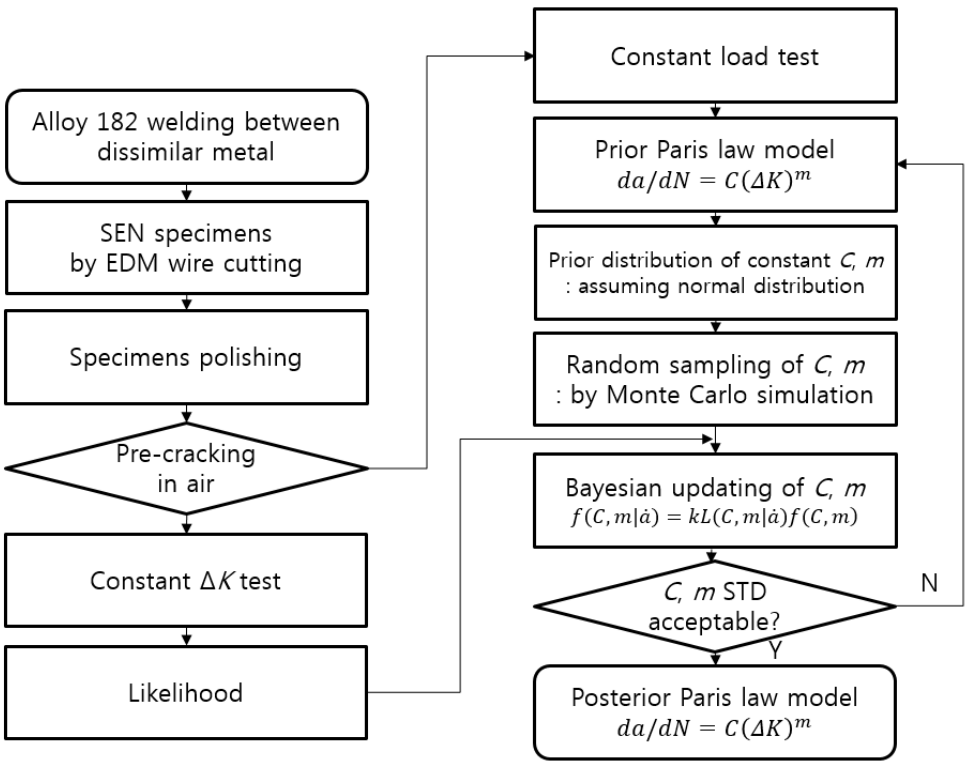

Figure 3.1 Overall approach for Bayesian updating.

Chapter 4 Experiment

4.1 Materials

The material used in this study was that remaining after carrying out a Korea Institute of Energy Technology Evaluation and Planning (KETEP) project. SA508 Gr.3 Cl.1 LAS and TP304 SS base metals were selected by reference to the surge line nozzle weld used in South Korean Kori NPP Unit 1. The chemical compositions of the two base metals are shown in Table 4.1 and their mechanical properties are presented in Table 4.2 [20].

Alloy 182 dissimilar metal welding between LAS and SS was done by the welding procedure specification (WPS) applied to an actual NPP facility nozzle. Welding was carried out using shielding metal arc welding (SMAW). After buttering with alloy 182, post-welding heat treatment (PWHT) was carried out for 41 h at 605℃ to eliminate the residual stress. The PWHT conditions are shown in Table 4.3. After using the alloy 182 welding rod, V-groove welding was carried out. A schematic diagram of the dissimilar metal weld of a single V-groove is shown in Figure 4.1. The welding procedure is described in Appendix A [20].

The chemical composition of the weld was analyzed using glow discharge spectrometer (GDS) at the cross section of the welding region. The chemical composition was measured at four positions, as shown in Figure 4.2. The results are shown in Table 4.4 [20].

4.2 Experimental Procedure

4.2.1 Tensile test procedure

The procedure for performing a tensile test in order to obtain the yield strength of the alloy 182 weld for the fatigue crack growth test conditions is as follows.

The tensile test was carried out in accordance with ASTM E8/E8M−15a [21]. Tensile specimens were taken from the same location as the fatigue crack growth test specimens, as shown in Figure 4.3, and rectangular tension test specimens were made, as shown in Figure 4.4. The drawings were made using the CATIA V5R18 program.

The tensile test was performed using an Instron® 8516 servo−hydraulic−controlled machine with a load capacity of 100 kN (calibration date: 23−July−2015) and strain was measured by a Reliant Technology extensometer calibrated by ASTM E83 (calibration date: 15−Feb.−2013, First use: 05−Sept.−2014). These instruments were controlled by computer using the Series X9 program. The tests were performed in air at 25℃ and the strain rate was 0.75 mm/min. The tensile testing machine and specimen are shown in Figure 4.5.

4.2.2 Fatigue crack growth rate (FCGR) test specimen and requirements

Fatigue specimens were made in accordance with references 16−19, as shown in Figure 4.6 [16−19]. Specimens were taken from the positions shown in Figure 4.3; the crack plane had a T−L

orientation. The letter T means the direction of the principal tensile stress and the letter L means the direction of crack propagation, as shown in Figure 4.7 [22]. Specimens were fabricated using EDM wire cutting to avoid the influence of heat.

The fatigue crack growth rate testing specimen shown in Figure 4.6 had a relationship with the stress intensity factor, K, the load, and other geometrical factors as per the following equation (4.1) [17]:

$$K = \frac{P\sqrt{a}}{BW}\left[1.986 + 1.782\left(\frac{a}{W}\right) + 6.998\left(\frac{a}{W}\right)^2 - 21.505\left(\frac{a}{W}\right)^3 + 45.351\left(\frac{a}{W}\right)^4\right] \quad (4.1)$$

where K is the stress intensity factor ($\mathrm{MPa}\sqrt{m}$), P is the applied load (N), a is the crack length (mm), B is the thickness of the specimens (mm), and W is the width of specimens (mm). A comparison of this equation (4.1) to the theoretical data shows a maximum difference of 6% at a/W = 0.621 [17]. Therefore, for the accuracy of the test results, cracks were generated until each specimen's crack length (a) was 40.24 mm because its width (W) was 64.8 mm.

A fatigue crack growth rate test specimen should maintain a predominantly elastic condition. Then, the crack-tip stress intensity, defined by the linear-elastic theory, can be measured by using linear elastic fracture mechanics (LEFM). With this stress intensity factor, the Paris law model can be determined. For this reason, there are two constraints. First, the stress applied to the uncracked ligament has to maintain a value less than the yield strength of the material. Therefore, the following equation should be satisfied [17]:

$$\sigma_{\max} = \frac{P_{\max}}{B(W-a)} \leq \sigma_y \tag{4.2}$$

The second constraint is that the monotonic plastic zone size ($2r_p$) should be below 25% of the specimen's ligament. The value r_p is shown in equation (4.3) [17, 18].

$$r_p = \frac{1}{2\pi}\left(\frac{K_{\max}}{\sigma_y}\right)^2 \tag{4.3}$$

Therefore, the following constraint can be obtained:

$$W-a \geq \frac{4}{\pi}\left(\frac{K_{\max}}{\sigma_y}\right)^2 \tag{4.4}$$

Thus, $K_{\max}$ can be written as equation (4.5).

$$K_{\max} \leq \sqrt{\frac{(W-a)\pi\sigma_y{}^2}{4}} \tag{4.5}$$

In other words, to maintain elastic condition, equations (4.2) and (4.5) should be satisfied. In this study, equation (4.2) was always satisfied. The loading condition of the fatigue test was $P_{\max}$ = 11 kN. Equation (4.5) was satisfied until a = 32.86 mm and ΔK = 48.30 $\mathrm{MPa}\sqrt{m}$.

Polishing was performed on the centerline of the specimen from the point where the crack started to the expected crack finishing point because the crack length was measured visually using a travelling microscope. Polishing was carried out with silicon carbide

paper (Allied High Tech Products, Inc.) of grit 320, 400, 600, 800, and 1200. After each polishing step, 5 min degassing and 10 min sonic cleaning were performed in 99.9% ethyl alcohol by using the Branson 3210 ultrasonic cleaner shown in Figure 4.8 [23]. After polishing, transparent adhesive ruler sticker was attached on the specimen along the crack growth centerline region to measure specimen's crack length before the area outside the centerline region, which is exposed to water, was protected by using MICCROShield stop-off lacquer produced by Tolber Chemical Division.

4.2.3 Crack length measurement method

The crack length of the specimens was measured optically using a travelling microscope and the direct potential drop (DCPD) method using an Agilent 34420A nano digital voltmeter. The relationship between DCPD and the crack length is shown in equation (4.6) [24].

$$a = \frac{2W}{\pi}\cos^{-1}\left(\frac{\cosh\left(\frac{\pi y}{2W}\right)}{\cosh\left\{\frac{U}{U_0}\cosh^{-1}\left(\frac{\cosh\left(\frac{\pi y}{2W}\right)}{\cos\left(\frac{\pi a_0}{2W}\right)}\right)\right\}}\right) \tag{4.6}$$

where U is the potential drop (V), U_0 is the reference potential drop (V), a is the crack length (mm), a_0 is the reference crack length

(mm), y is the length between the notch centerline and the voltage measurement point (mm), and W is the width of the specimen (mm), as shown in Figure 4.9.

Platinum wire (ø = 1 mm) to carry direct current and alloy 600 wire (ø = 0.5 mm) to detect voltage were spot welded with energies of 100% and 38%, respectively, onto the specimen, as shown in Figure 4.9. Spot welding was performed by using a UNITEK PECO™ dual-pulse 125 stored energy power supply, as shown in Figure 4.10. The platinum wire was protected by using heat-shrink tubing to prevent the current from flowing to other instruments.

4.2.4 Environment control method

To create the low-temperature water environment, a cell was fabricated as shown in Figures 4.11 and 4.12 in accordance with references 17-19 [17-19]. The specimen was placed in the cell and fixed on the top and bottom of the lower part of the cell body, as shown in Figure 4.12. Water leakage was prevented by using O-rings. Water flowed through the cell from the lower right side of the cell through the pipe nipple thread and discharged through the upper left side of the cell. A fritted glass immersion disk was inserted from the left side of the cell and nitrogen gas was bubbled through the fine holes to make deaerated water. A Luggin probe was attached at the right side of the cell to minimize IR drop by the probe being closer to the specimen, which was a working electrode [19]. Cathodic polarization was applied to the working electrode and platinum wire (ø = 0.5 mm) counter electrode, as shown in Figure 4.12. The prepared fatigue crack growth test specimen and cell is

shown in Figure 4.13. A drawing of the cell is given in Appendix B.

An electrochemical corrosion potential (ECP) was applied to create shutdown conditions under atmospheric pressure of 1 atm. ECP was calculated as follows by the Nernst equation to arrive at a dissolved hydrogen concentration of 30 cc H_2/kg H_2O at a water temperature of 54℃ [25]:

$$E = E_0 - \frac{RT}{nF}\ln\left(\frac{f(H_2)}{a_{H^+}^{\ 2}}\right) \text{ for } 2H^+ + 2e \rightarrow H_2 \tag{4.7}$$

where E is the electrode potential (V), T is the absolute temperature (K), R is the universal gas constant (J/mol/K), n is the number of electrons (= 2) used in reaction, F is the faraday constant (C/mol), f is the fugacity of gas, and a is the activity of the ions. pH is given as $pH = -\log_{10}(a_{H^+})$ and Henry's law is $f(H_2) = k_{H^2} X_{H^2}$ (X_{H^2} is mole fraction). Thus, the Nernst equation can be written as equation (4.8).

$$E = E_0 - \frac{RT}{nF} \times 2.303 \times \left[\log_{10}\left(k_{H^2} X_{H^2}\right) + 2 \times pH\right] \tag{4.8}$$

Putting shutdown conditions into equation (4.8) is shown in equation (4.9). Henry's constant was selected by using solubility graphs of helium in water, as shown in Figure 4.14. The value for Henry's constant is 7.6×10^{-4} atm/mole fraction [26].

$$\begin{aligned} E(vs.SHE\ at\ 25°C) = &-\frac{8.31415(J/mol/K)\times 328.15(\mathrm{K})}{2\times 96500(C/mol)} \times 2.303 \\ &\times\left[\log_{10}\left(7.6\times10^{-4}(atm/mole\ fraction)\times\left(\frac{30(cc)/(22400cc/mol)}{1(kg)\times1000(g/kg)/18(g/mol)}\right)\right)+2\times7\right] \end{aligned} \tag{4.9}$$

Therefore, the applied potential was E (vs. SHE at 25℃) = −203.9 mV by using a standard hydrogen electrode (SHE) as the reference electrode and E (vs. SCE at 25℃) = −444.9 mV by using a standard calomel electrode (SCE) as the reference electrode.

4.2.5 Description of fatigue crack growth test system

A schematic diagram of the fatigue crack growth test system is shown as Figure 4.15 and the actual testing system is shown in Figure 4.16. To prevent water from entering into the Instron® 8516, a large polyethylene plastic film was placed on the upper side of the bottom pillar, as shown in Figure 4.16. The water tank used was a 25 L Nalgene® carboy with a spigot made of low−density polyethylene (LDPE). Ultrapure water with a resistivity is over 18 MΩ·cm and 0.01 M sodium sulfate (Na_2SO_4) for the electrolyte were added to the tank to facilitate cathodic polarization.

To create deaerated water, nitrogen gas was bubbled through the glass in the water bath and cell, as shown in Figure 4.18 and Figure 4.25. The bubbling rate was 100 cc/min, as shown in Figure 4.17. All tubing was used Tygon S3™ E−3603 laboratory tubing to reduce the contamination of water.

The water flow system was as follows. First, water was sent from the water tank at a rate of 25 mL/min, flowing into the glass in the water bath using an EYELA NTT−2000 system. Water was boiled at 80℃, as shown in Figure 4.18, then sent into the fatigue crack growth test cell and discharged to another water tank using a Nalgene® carboy with a handle. The water bath temperature remained within ±0.05℃.

The temperature of the water in the cell and the air outside the cell was measured by using K-type thermocouples, as shown in Figure 4.19. The buffer system was made using a salt bridge to protect the SCE from the effect of chloride (Cl) ions.

The salt bridge shown in Figure 4.20 was made as follows. First, 100 mL of ultrapure water in the water bath was heated. 12 g of potassium sulfate (K_2SO_4) was then added to make saturated potassium sulfate water. 3 g of agar was then slowly added and the mixture was heated for 10 min. After heating, the mixture was put into a U-tube with a syringe and both ends were occluded with cotton wool, allowing the mixture to cool slowly at room temperature in air [27].

To apply ECP, a Solartron SI 1287 potentiostat was used, as shown in Figure 4.21. The potentiostat was controlled by computer using CorrWare® software [17].

The light source of the travelling microscope was an Excelitas X-strobe stroboscope, as shown in Figure 4.22. Light went through the optical fiber to the travelling microscope. The power supply for the DCPD method was an Agilent N6705B analyzer with an Agilent N6753A module, as shown in Figure 4.23. Voltage measurements for the DCPD method were taken using an Agilent 34970A data acquisition and switch unit and Agilent 34420A nano volt/micro ohm meter, as shown in Figure 4.24.

4.2.6 Fatigue crack growth rate test procedure

The fatigue crack growth test used an Instron® 8516, the same as for the tensile test. The fatigue test was controlled by computer using Instron® Fatigue Crack Propagation -Da/DN- software. The

fabricated specimen and cell were mounted on the grip of the Instron® 8516 machine. The grip was insulated by Teflon® to prevent leakage current. Drawings of the grips, pins, and insulation are given in Appendix C. The set-ups for the specimen and cell are shown in Figures 4.25 and 4.26. Fatigue pre-cracking was carried out at 25℃ in air, and the fatigue pre-cracking conditions are given in Table 4.5. Fatigue pre-cracking photographs taken with the travelling microscope are shown in Figure 4.27. Five fatigue tests were performed in this study. The detailed conditions are given in Table 4.6.

Table 4.1 Chemical composition of base metals

Element	Chemical composition (%)	
	SA508 Gr.3 Cl.1	TP304
C	0.2	0.044
Si	0.17	0.47
Mn	1.36	1.15
P	0.007	0.038
S	0.002	0.002
Ni	0.73	8.00
Cr	0.12	18.14
Mo	0.48	0.22
V	0.008	-
N	-	0.023
Cu	-	0.34
Fe	Balance	Balance

Table 4.2 Mechanical properties of base metals

Material	SA508 Gr. 3 Cl. 1	TP304
Yield Strength (MPa)	510	277
Tensile Strength (MPa)	648	578
Elongation (%)	28	50

Table 4.3 Post-welding heat treatment (PWHT) conditions

Type of Heat Treatment	PWHT
Loading Temperature (℃)	245
Heating Rate (℃/h)	50
Holding Temperature (℃)	600-610
Holding Time	41 h 05 min
Cooling Rate (℃/h)	50
Unloading Temperature (℃)	240

Table 4.4 Chemical composition of alloy 182 dissimilar metal weld in Figure 4.2 by glow discharge spectrometer (GDS) [20]

Elements	Chemical Composition (%)			
	1	2	3	4
C	0.058	0.06	0.061	0.057
Si	0.61	0.6	0.59	0.58
Mn	6.98	7.04	6.96	6.67
P	0.010	0.011	0.011	0.011
S	0.005	0.005	0.005	0.005
Cr	14.5	14.5	14.4	14.7
Mo	0.59	0.59	0.59	0.58
Fe	6.99	6.81	6.93	8.83
Ti	0.41	0.46	0.36	0.39
Nb	1.73	1.56	1.56	1.59
Ni	Balance	Balance	Balance	Balance

Table 4.5 Fatigue pre-cracking conditions

Mode	Constant ΔK
ΔK (MPa$\sqrt{m}$)	25
R ($\sigma_{min}/\sigma_{max}$)	0.1
Frequency (Hz)	20
Environment	Air
Temperature	Room Temperature
Pre-crack Length (mm)	2

Table 4.6 Fatigue crack growth test conditions

Fatigue Test Number		1	2	3	4	5
Load Control	Mode	Constant Load		Constant ΔK		Constant Load
	ΔP (kN)	9	9.9	–	–	9.9
	ΔK (MPa$\sqrt{m}$)	–	–	30	35	–
	R ($\sigma_{min}/\sigma_{max}$)	0.1				
	Frequency (Hz)	10				1
Environment Control	Environment	Air	0.01 M Na_2SO_4 Deaerated Water			
	Temperature (℃)	25	54			
	Applied ECP (mV vs. SCE 25℃) (OCP = −217.5 mV)	–	−444.9			

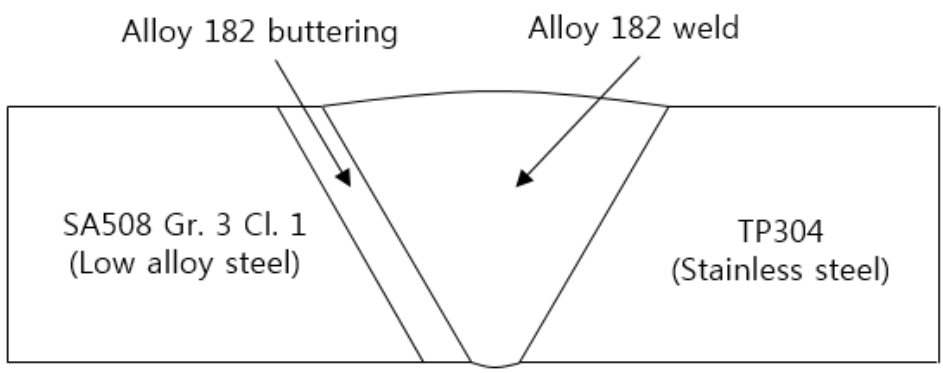

Figure 4.1 Schematic diagram of the dissimilar metal weld of single V-groove design.

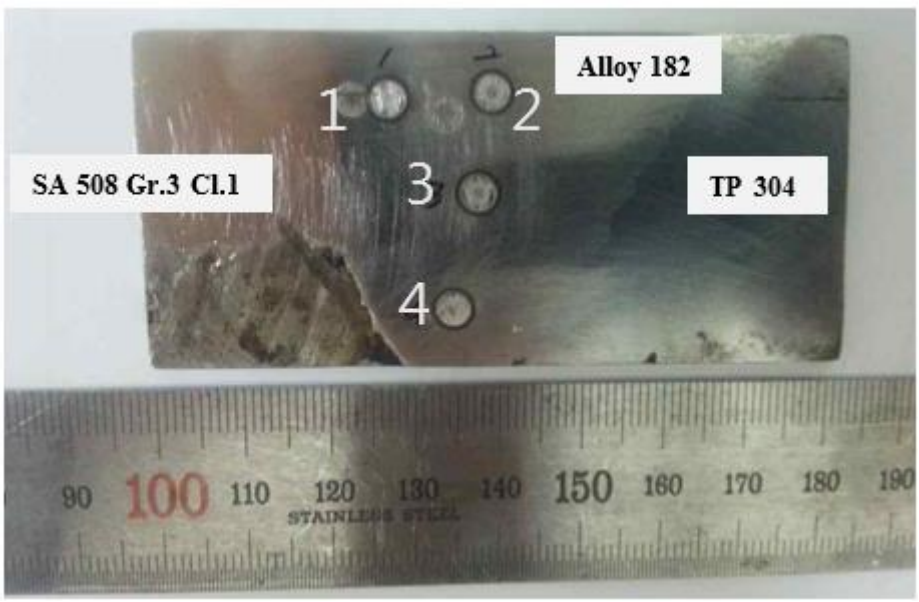

Figure 4.2 Photographs of alloy 182 dissimilar metal weld cross section for glow discharge spectrometer (GDS) [20].

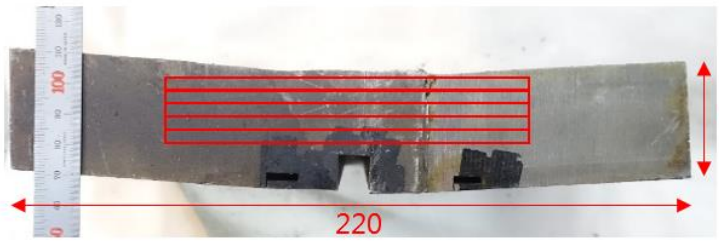

(a)

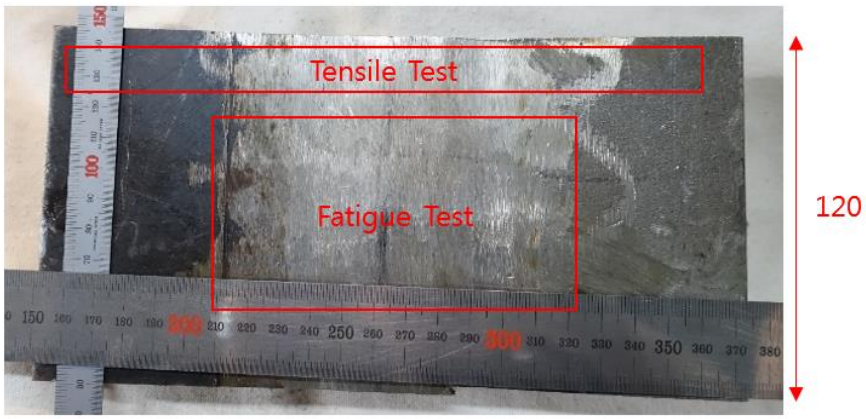

(b)

Figure 4.3 Photographs of alloy 182 dissimilar metal weld: (a) side view and (b) top view (units: mm).

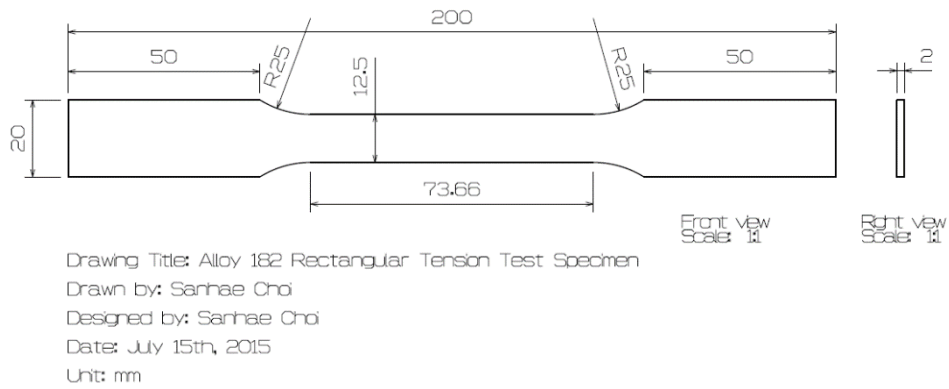

Figure 4.4 Schematic diagram of alloy 182 rectangular tension test specimen for tensile test (units: mm).

Figure 4.5 Photographs of tensile testing machine and specimen.

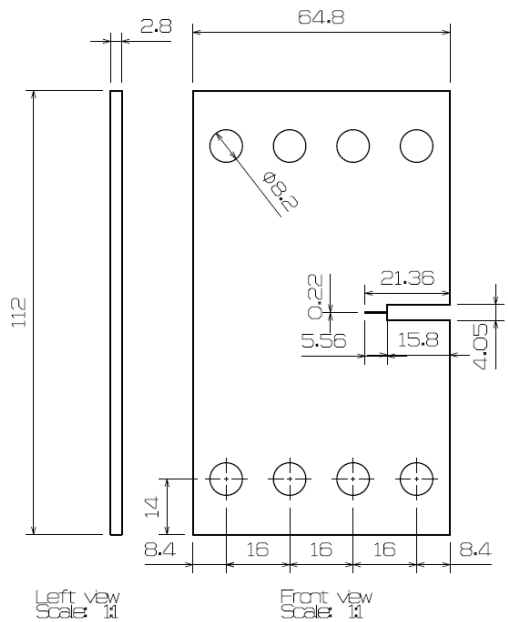

Drawing Title: Alloy 182 SEN Specimen Design for Fatigue Crack Growth Rate Testing
Drawn by: Sanhae Choi
Designed by: Sanhae Choi
Date: July 15th, 2015
Unit: mm

Figure 4.6 Schematic diagram of alloy 182 single-edge notch (SEN) specimen for fatigue crack growth rate testing (units: mm).

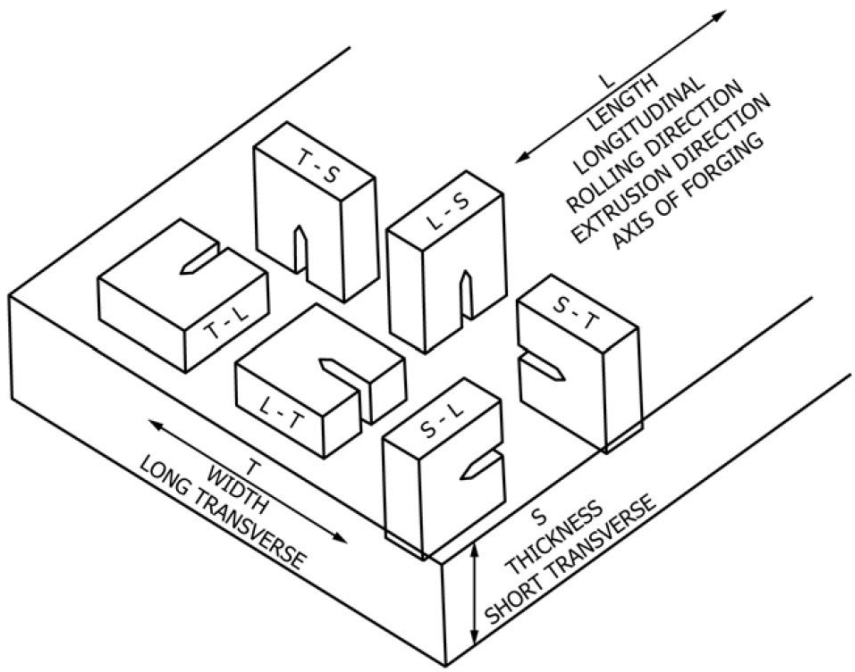

Figure 4.7 Crack plane identification of rectangular sections [22].

Figure 4.8 Branson 3210 ultrasonic cleaner and alloy 182 specimen.

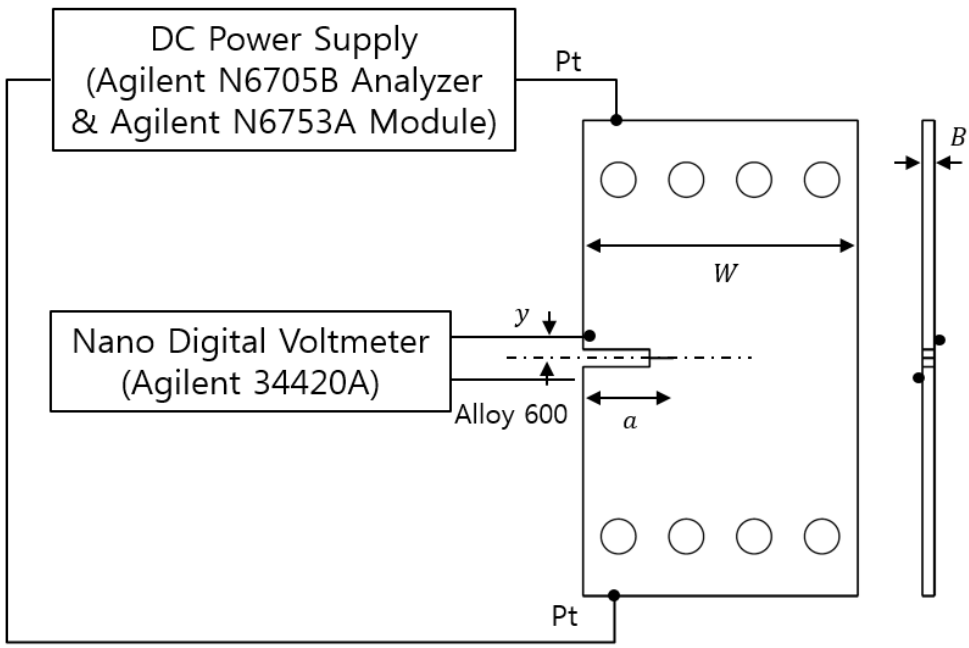

Figure 4.9 Wire attachment positions on the specimens.

Figure 4.10 UNITEK PECO™ dual-pulse 125 stored energy power supply for spot welding.

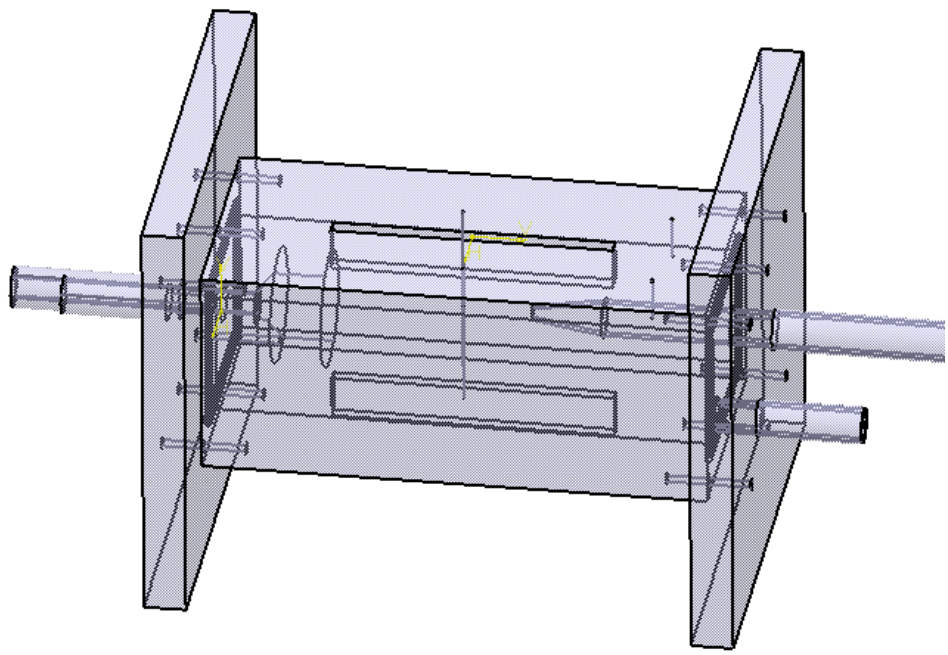

Figure 4.11 Schematic diagram of acrylic test cell (isometric view).

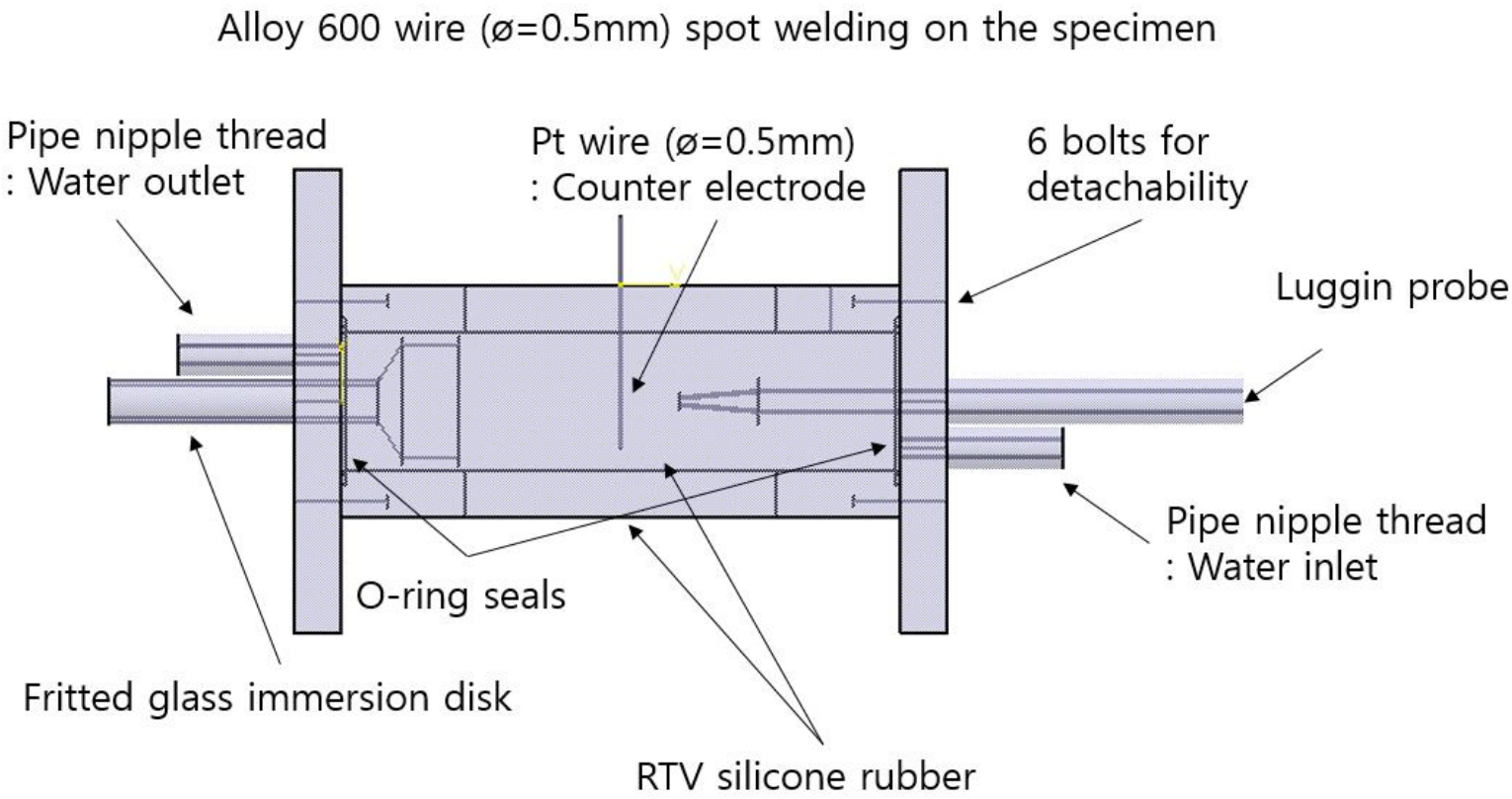

Figure 4.12 Schematic diagram of acrylic test cell (front view).

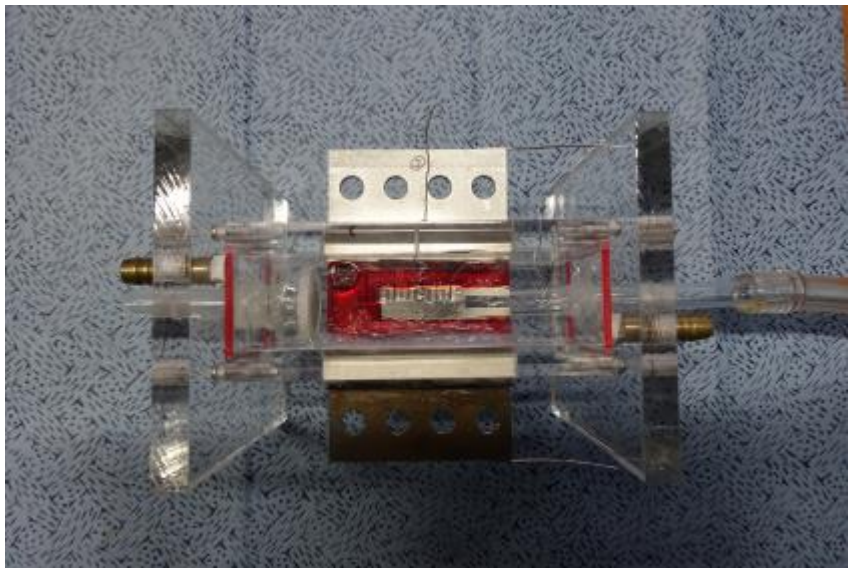

(a)

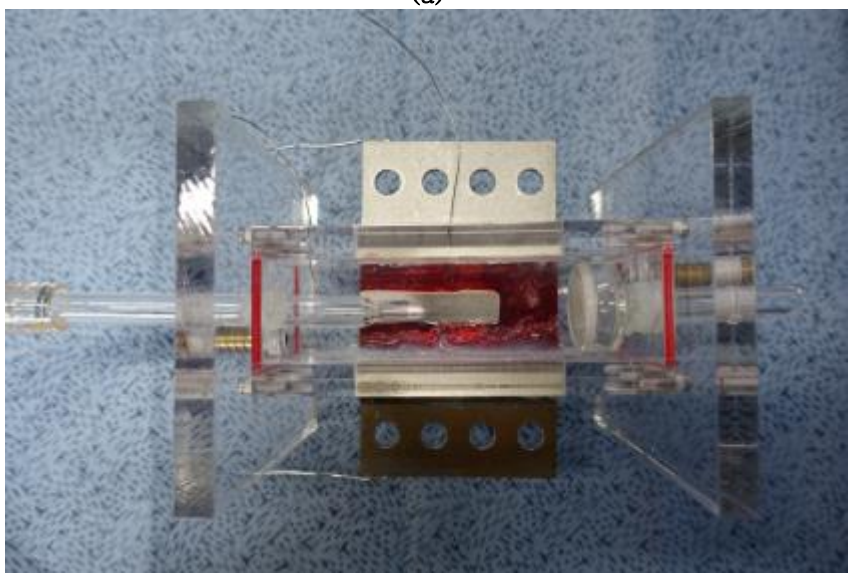

(b)

Figure 4.13 Photograph of a prepared fatigue crack growth test specimen and cell: (a) front view and (b) back view.

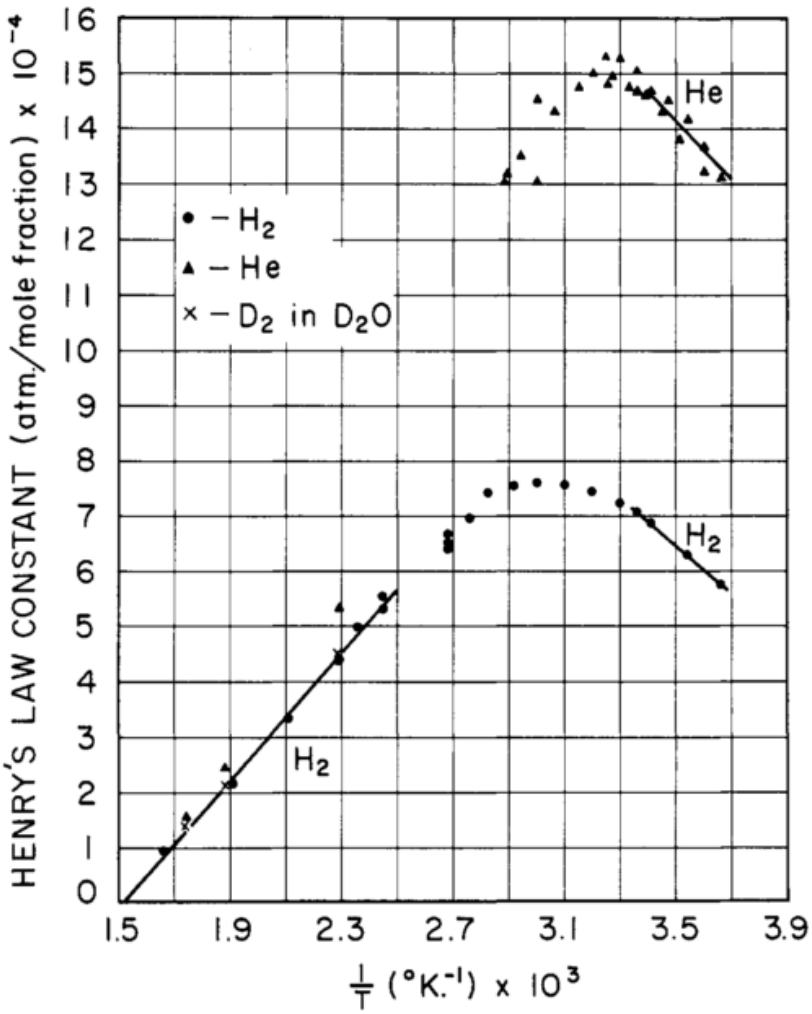

Figure 4.14 Solubility of hydrogen and helium in water [26].

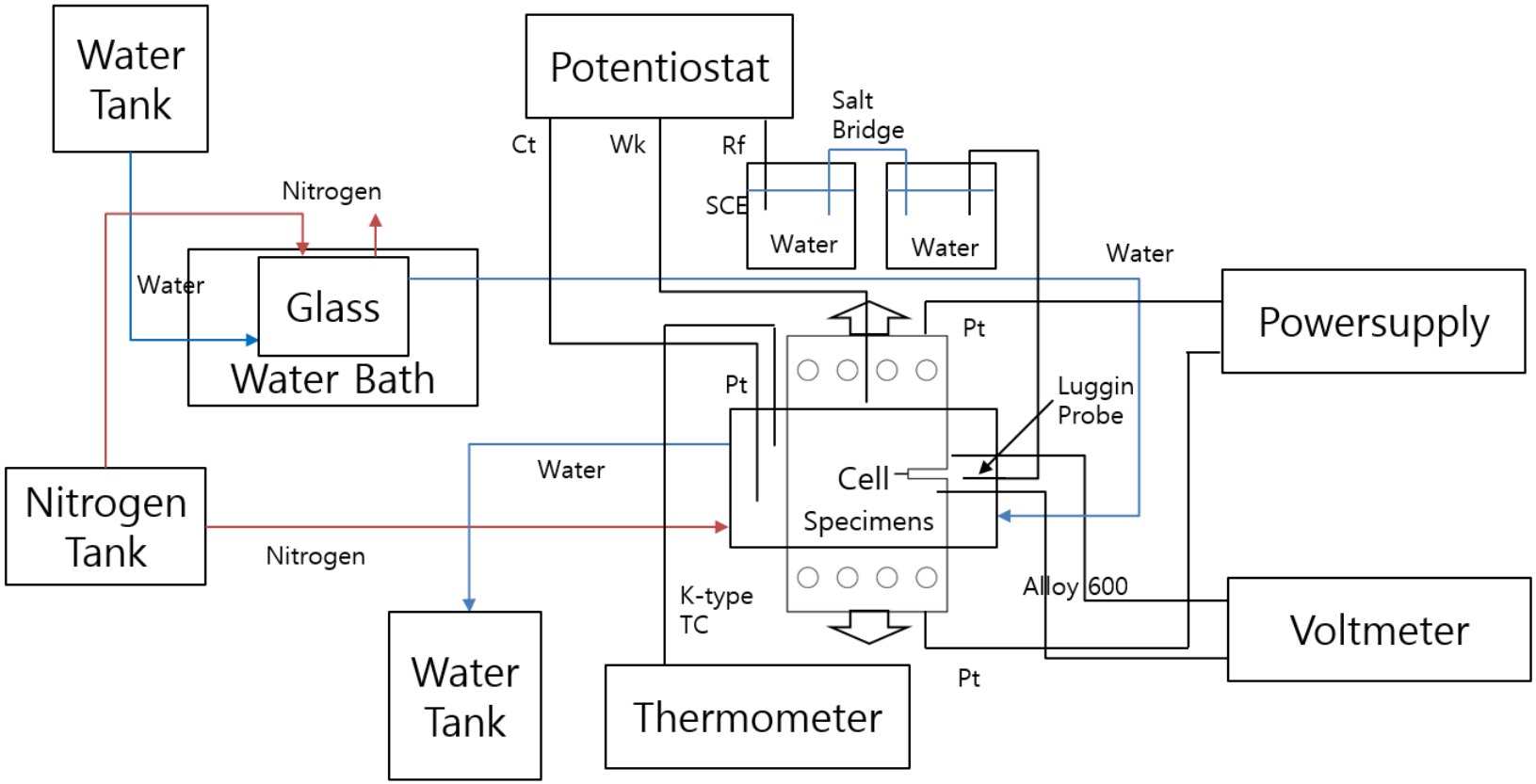

Figure 4.15 Schematic diagram of fatigue crack growth test in low-temperature water.

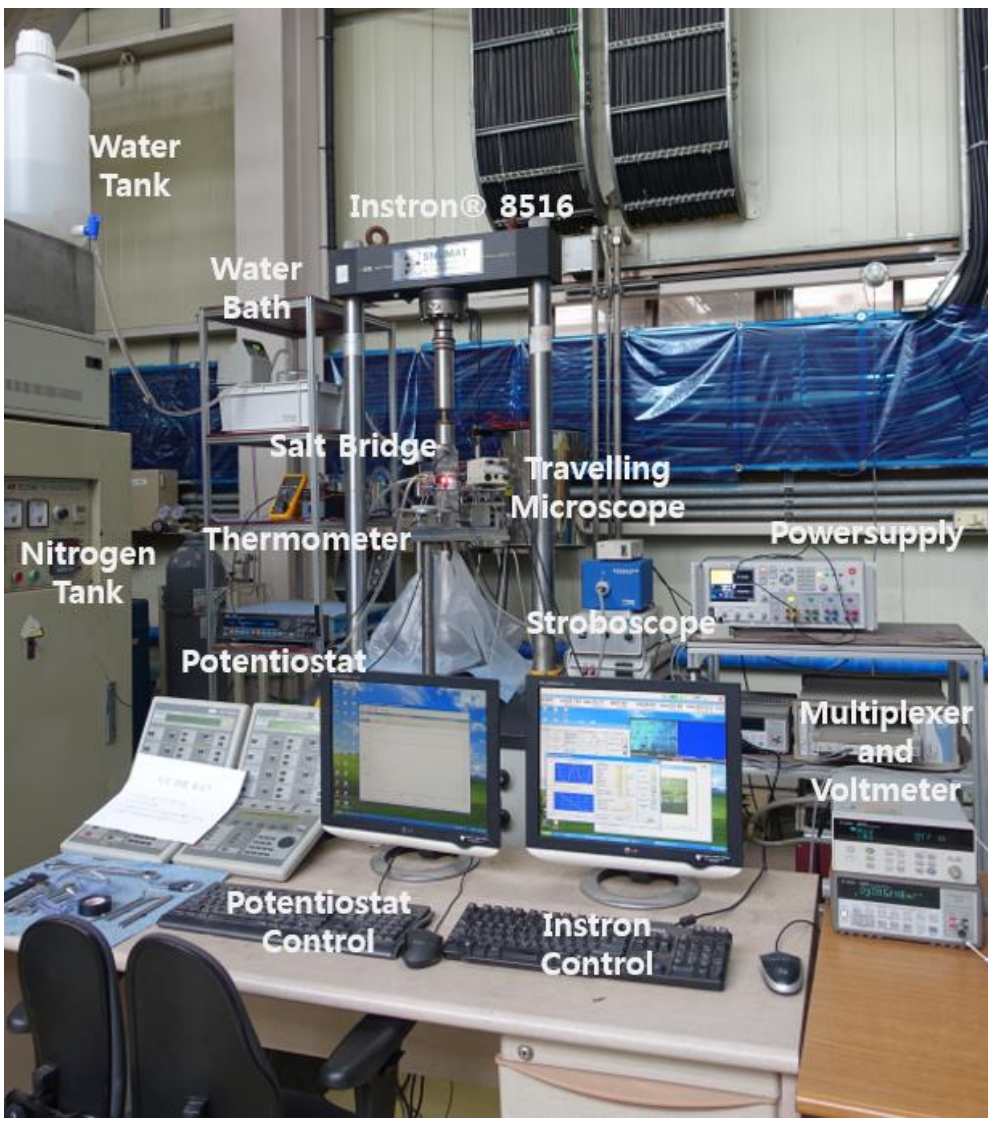

Figure 4.16 Photograph of the fatigue crack growth test system in low-temperature water.

Figure 4.17 Photograph of nitrogen tank and gas bubbling system.

Figure 4.18 Photograph of EYELA NTT-2200 water bath system.

Figure 4.19 Photograph of temperature measurement system: (left) temperature inside of the cell and (right) temperature outside of the cell.

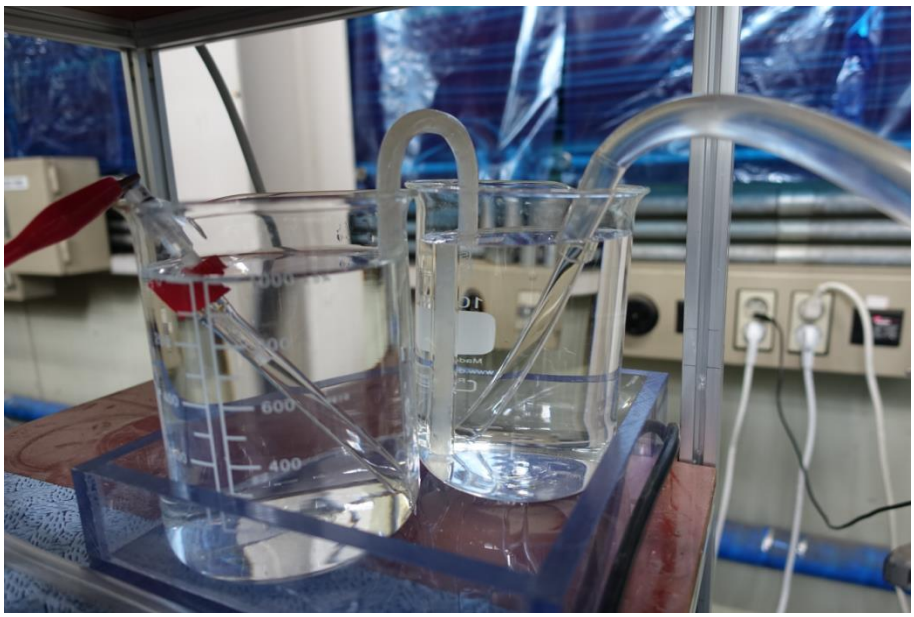

Figure 4.20 Reference electrode buffer system and salt bridge.

Figure 4.21 Photograph of Solartron SI 1287 potentiostat.

Figure 4.22 Photograph of Excelitas X-strobe stroboscope.

Figure 4.23 Photograph of Agilent N6705B power supply.

Figure 4.24 Photograph of Agilent 34970A data acquisition and switch unit and Agilent 34420A nano volt/micro ohm meter.

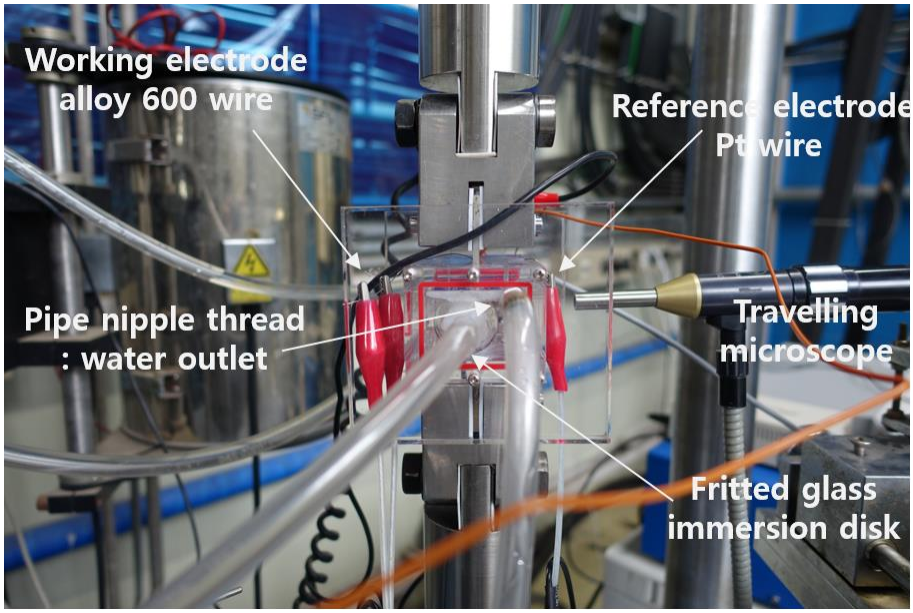

Figure 4.25 Photograph of test specimen and cell (left view).

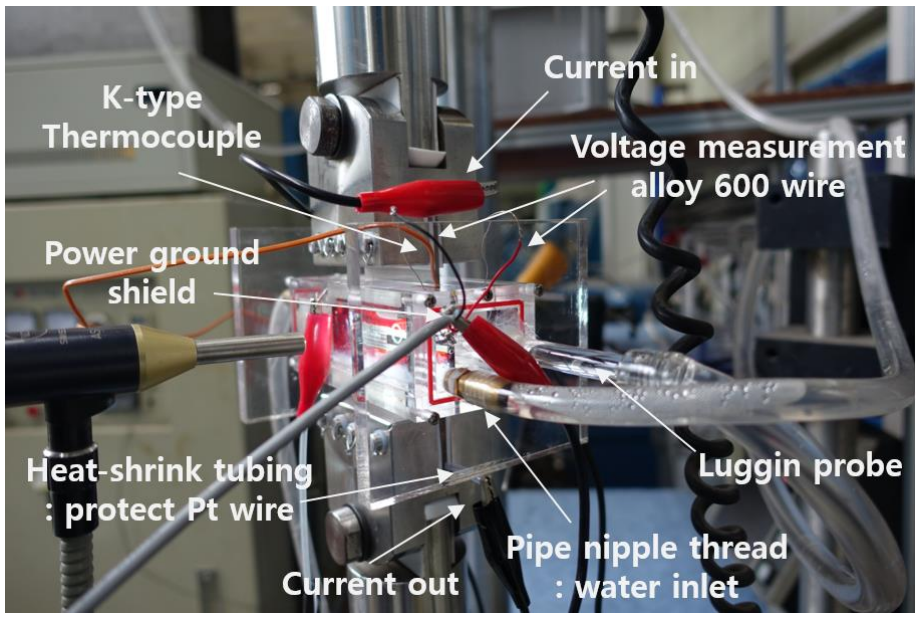

Figure 4.26 Photograph of test specimen and cell (right view).

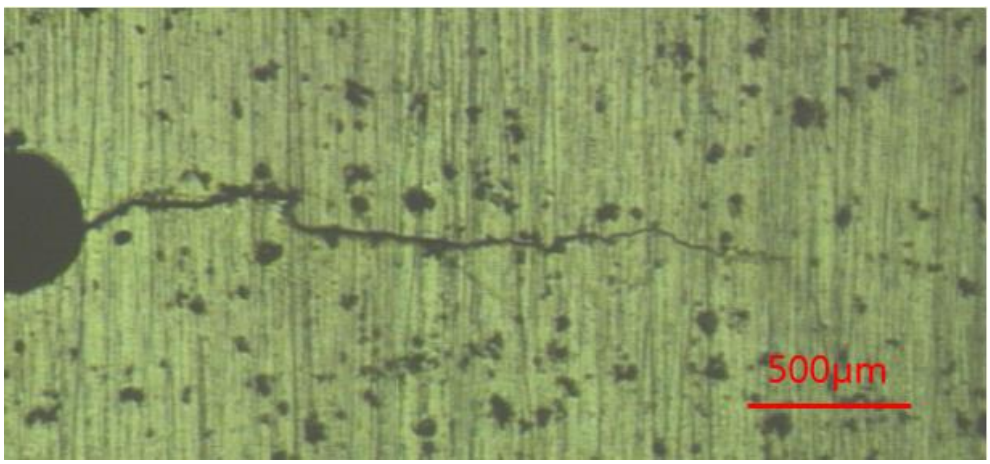

Figure 4.27 Photograph of fatigue pre-cracking of alloy 182 dissimilar metal weld specimen with travelling microscope.

Chapter 5 Finite Element Method Analysis

5.1 Preprocessing of Finite Element Method

Before the experiment, type 304 stainless steel stress and fatigue life were simulated under the same conditions as the alloy 182 weld fatigue test in air with finite element method (FEM) analysis using the ANSYS 14.0 program. Type 304 stainless steel was selected because it had the lowest yield strength of the three alloys used. An S–N curve (alternating stress amplitude (S) versus number of cycles (N) to failure) was used in this analysis as per Hayashi [28]. The curve was plotted as shown in Figure 5.1 using the MATLAB R2013b program. The specimen was modeled and the maximum load of 10 kN was placed on the upper and lower holes of the specimen, as shown in Figure 5.2. The mesh of the specimen had 24439 nodes and 4204 elements, as shown in Figure 5.3.

5.2 Results of Finite Element Method Analysis

Normal stress analysis of the y–axis direction results are shown in Figure 5.4. In most of the region, except the stress concentration on the notch region, it was confirmed that the stress was applied below the yield strength. It was predicted that the specimen would not fail until reaching 10^8 fatigue cycles, which is the maximum input cycle of the S–N curve, as shown in Figure 5.5. Of course, the real test is somewhat different because of the grips. However, this simple case was analyzed with FEM. The stress distribution and fatigue life are shown in this study.

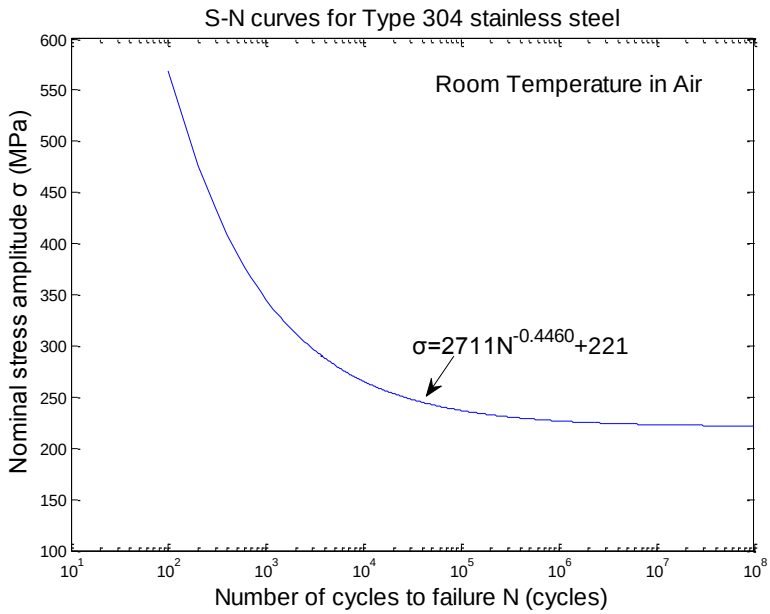

Figure 5.1 S–N curves for type 304 stainless steel.

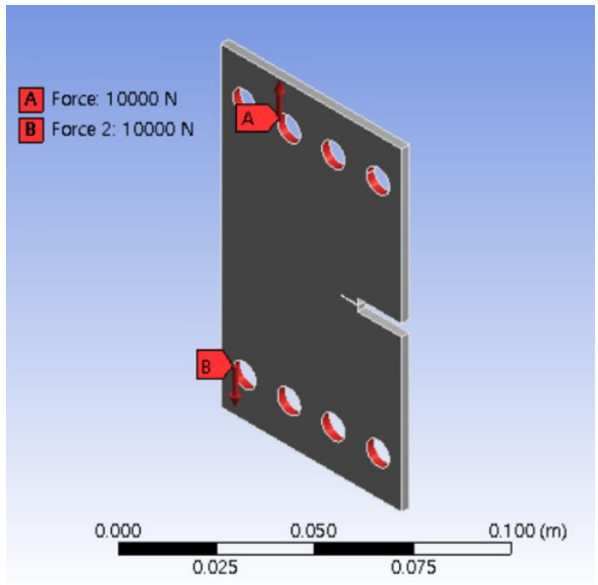

Figure 5.2 Load condition of the fatigue crack growth test specimen.

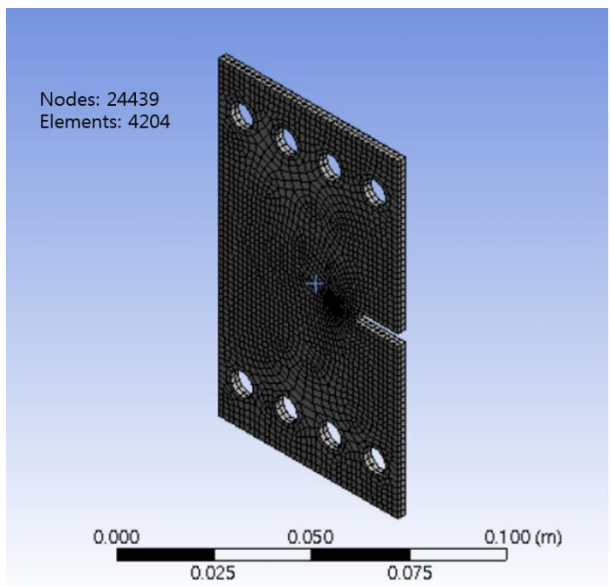

Figure 5.3 Mesh condition of the fatigue crack growth test specimen.

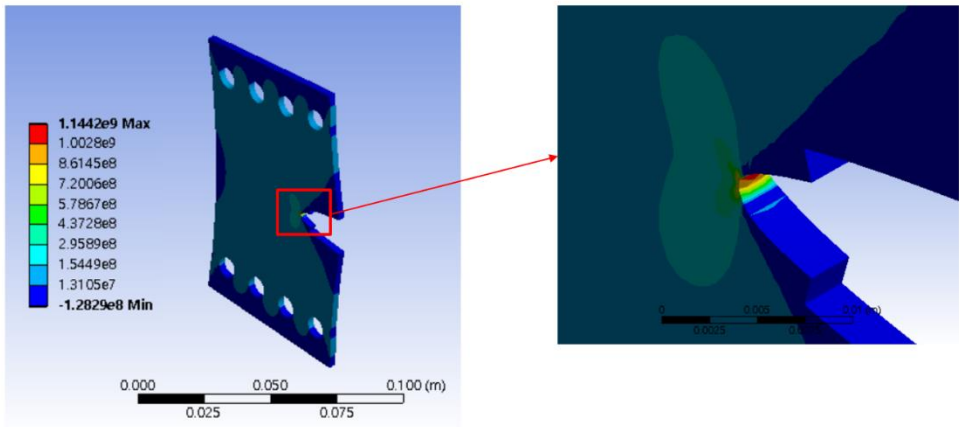

Figure 5.4 Normal stress of the y-axis direction of type 304 stainless steel specimen.

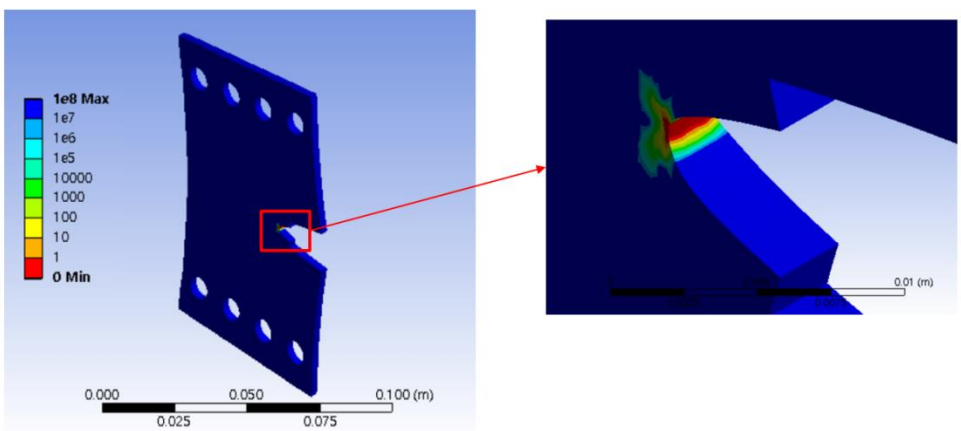

Figure 5.5 Fatigue life of type 304 stainless steel specimen.

Chapter 6 Results

6.1 Tensile and Hardness Test Results

6.1.1 Tensile test results

Tensile specimens before and after performing the experiment are shown in Figure 6.1, and the stress-strain curves of the alloy 182 dissimilar metal weld are shown in Figure 6.2. The mechanical properties of alloy 182 weld are listed in Table 6.1. Among them, the yield strength of the alloy 182 dissimilar metal weld was 342.6 MPa.

6.1.2 Hardness test results

A 10 × 10 × 2.8 mm specimen was made by using the remaining part of the alloy 182 dissimilar metal weld. The specimen was taken by using EDM wire cutting from the upper side of the material. The hardness of the specimen was measured with a Mitutoyo hardness testing machine 810-353K, as shown in Figure 6.3, after polishing in the same way as the fatigue growth test specimen. The test was controlled by using the Leopard 2009 program, as shown in Figure 6.4. Vickers hardness was measured with an applied load of 0.1 kgf. The hardness of the alloy 182 dissimilar metal weld was 203.9 kgf/mm^2. These results are listed in Table 4.1.

6.2 Fatigue Crack Growth Test Results

6.2.1 Effect of low-temperature water chemistry

Two tests were carried out to determine the effect of hydrogen embrittlement on the low-temperature fatigue crack growth rate. Test 1 was performed under constant load at 25℃ in air. Test 2 was carried out under constant load at 54℃ in 0.01 M sodium sulfate (Na_2SO_4) deaerated water and an applied ECP of −444.9 mV (vs. SCE at 25℃). The results of the tests were plotted as the log scale of the fatigue crack growth rate versus the log scale of the stress intensity factor range, as shown in Figure 6.5. Paris law fitting was obtained as follows in air:

$$\frac{da}{dN} = 4.82 \times 10^{-11} \times (\Delta K)^{4.09} \text{ in air} \qquad (6.1)$$

In the same way, the Paris law for 0.01 M sodium sulfate deaerated low-temperature water environment was obtained as follows:

$$\frac{da}{dN} = 3.41 \times 10^{-11} (\Delta K)^{4.28} \text{ in water} \qquad (6.2)$$

As seen from this graph, it was confirmed that the fatigue crack growth rate of the alloy 182 dissimilar metal weld in the presence of dissolved hydrogen and in low-temperature water was faster than that in air.

6.2.2 Constant ΔK test results for Bayesian updating

Tests 3 and 4 were carried out under constant ΔK and the same condition of constant load in water to obtain the likelihood distribution. Likelihood is used to reduce the uncertainty of the Paris law constants by using Bayesian inference. The test results of fatigue crack growth rate versus crack length for the two tests are shown in Figure 6.6. 34 fatigue crack growth rate data points were measured whenever the crack exceeded 0.5 mm in length in order to use the normal distribution conjugate of the likelihood function. The mean of the fatigue crack growth rate was 5.55×10^{-5} mm/cycle and the standard deviation was 8.18×10^{-6} mm/cycle at a constant ΔK = 30 $\mathrm{MPa}\sqrt{m}$. The mean of the fatigue crack growth rate was 1.04×10^{-4} mm/cycle and standard deviation was 1.30×10^{-5} mm/cycle at a constant ΔK = 35 $\mathrm{MPa}\sqrt{m}$. The results from tests 2−4 are plotted in Figure 6.7.

6.2.3 Effect of cyclic frequency

Test 5 was carried out to determine the effect of corrosion. The frequency condition of the constant load test in low-temperature water was changed from 10 Hz to 1 Hz. The results of the test are plotted in Figure 6.8 and the Paris law is shown in equation (6.3).

$$\frac{da}{dN} = 4.15\times10^{-9}\times(\Delta K)^{3.06} \text{ at 1 Hz loading frequency in water} \qquad (6.3)$$

With these test results, the fatigue crack growth rate increased

at low loading frequencies. Especially ΔK was small, the difference in the fatigue crack growth rate of the two tests was high. This is because corrosions effects were applied more than fatigue crack growth rate at high ΔK. However, the difference of the fatigue crack growth rate was small at high ΔK because corrosion effects were less important. With this test, alloy 182 dissimilar metal weld was affected more by corrosion at low loading frequencies.

6.2.4 Crack length results between the optical and the DCPD methods

When the constant ΔK = 35 $\mathrm{MPa}\sqrt{m}$ test was performed, the crack length measured optically by using the travelling microscope and the crack length measured by the DCPD method were compared and the results are shown in Figure 6.9. The results show that the slope is approximately 0.98. It was found that the crack length measured by the DCPD method was somewhat smaller than that by travelling microscope. The fractograph of the specimen, as shown in Figure 6.15, shows that the front of the specimen crack growth was longer than back of it. This may be because the chemical composition of the weld region in the front may have been different from that of the back because the specimen was made by V-groove welding. Therefore, the chemical composition between the front and back was different because of diffusion. Thus, the fatigue crack growth rate of the front and back of the specimen was different. Therefore, the DCPD method was more accurate than the optical method.

6.3 Fracture Morphology of Fatigue Crack Growth Test Analysis

To determine the fracture morphology of the fatigue crack growth test specimen, heat tinting was performed in accordance with ASTM E1820 after the fatigue test was over. Heat tinting was done in a furnace, as shown in Figure 6.10, for 30 min at 300℃ [29].

Fatigue crack growth testing of the specimen after heat tinting was carried out in air and then tensile stress was applied to separate the specimen. The lower part of the specimen was cut using a saw in order to analyze the specimen's fracture morphology with a field emission scanning electron microscope (FE-SEM). The specimen before the test, after the test, after heat tinting and specimen separation, and after saw cutting is shown in Figure 6.11.

Fracture morphologies of the four specimens under a constant load in air, a constant load in low-temperature water, a constant ΔK = 35 $\mathrm{MPa}\sqrt{m}$ in low-temperature water, and a constant load in low-temperature water at 1 Hz were taken by SIGMA FE-SEM, as shown in Figure 6.12.

Fractographs of the specimens were taken using the mosaic imaging method of FE-SEM, as shown in Figures 6.13-6.16. The pre-crack region, fatigue test region, post-fatigue region after testing, and tension region can be classified by crack length and the morphology of the fracture surface.

Striation markings were detected in the fatigue test region of the specimen under constant load in air, as shown in Figure 6.17. Because one striation length was approximately 1 μm and the fatigue crack growth rate was approximately 10^{-5} to 10^{-4} mm/cycle, it was confirmed that each cycle of the striation grew every 10 to 100 cycles of fatigue loading. The fracture morphology of the

fatigue test region near the notch tested under low-temperature water showed that the striations were blunted by corrosion, as shown in Figure 6.18. Also, as seen in Figure 6.19, the fracture morphology of the fatigue test region far from the notch at high ΔK showed that it followed a plastic blunt mechanism. Its morphology showed microvoid coalescence (MVC).

Striation markings were detected again in the post-fatigue region in air after the constant load fatigue test in water, as shown in Figure 6.20. The fracture morphology of the tension region is shown in Figure 6.21. It too shows significant MVC.

The fracture morphologies of the specimens at constant ΔK = 35 $\mathrm{MPa}\sqrt{m}$ and those of the constant load test at 1 Hz in low-temperature water are shown in Figure 6.22 and Figure 6.23, respectively. The specimen of the 1 Hz test was blunted more than the other samples, which confirms that corrosion had more of an effect at low loading frequencies.

The 10 × 10 × 2.8 mm specimen for measuring hardness, the fatigue specimens of the constant load test in air, constant ΔK = 35 $\mathrm{MPa}\sqrt{m}$ in low-temperature water, and constant load in low-temperature water at 1 Hz were analyzed by using energy dispersive X-ray spectroscopy (EDS). The results are shown in Figures 6.24 to 6.27. The difference in these figures was that the titanium (Ti) content was smaller and oxygen was detected after the fatigue test in water. It was thought that oxygen (O) was the result of oxidation of the specimen surface when in the furnace for heat tinting.

Inductively coupled plasma (ICP) mass spectrometer analysis of 0.01 M sodium sulfate deaerated low-temperature water before and after the fatigue test was carried out and the results are listed in Table 6.2. 0.02 mg/L of manganese (Mn) was detected before

and after the test. The sulfur (S) content increased approximately 0.6 mg/L from 345.681 mg/L to 346.265 mg/L.

Table 6.1 Mechanical properties of alloy 182 dissimilar metal weld

Yield Strength (MPa)	342.6
Tensile Strength (MPa)	622.4
Elastic Modulus (GPa)	205.1
Elongation (%)	28.57
Hardness (HV)	203.9

Table 6.2 Inductively coupled plasma (ICP) mass spectrometer results of 0.01 M sodium sulfate deaerated low-temperature water before and after fatigue test

Element	Before (mg/L)	After (mg/L)
Cu	ND	ND
Ni	ND	ND
Cr	ND	ND
Mn	0.002	0.002
Fe	ND	ND
P	ND	ND
Al	ND	ND
Si	ND	ND
S	345.681	346.265
Co	ND	ND
Ti	ND	ND

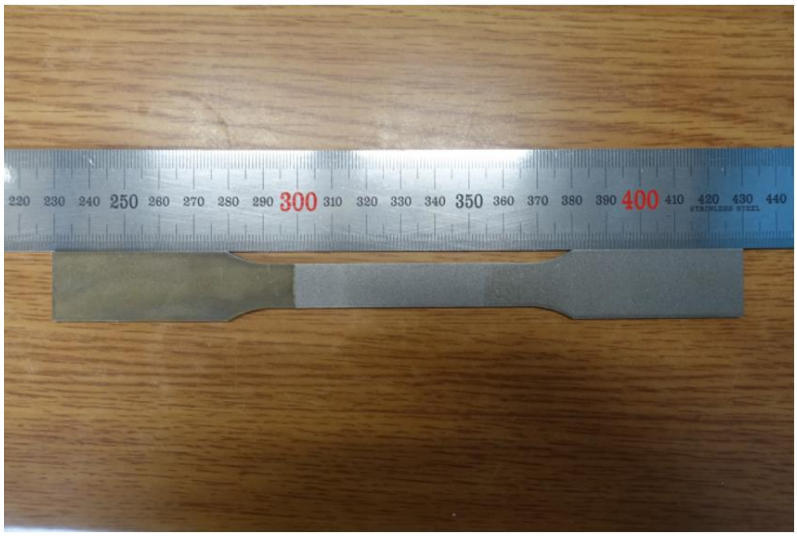

(a)

(b)

Figure 6.1 Tensile test specimen (a) before and (b) after fatigue test.

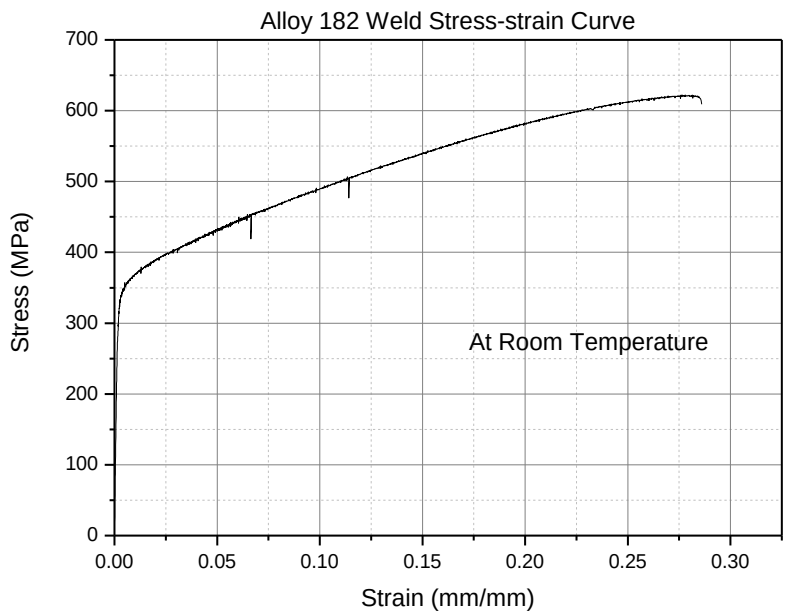

Figure 6.2 Stress-strain curve of alloy 182 dissimilar metal weld in air.

(a)

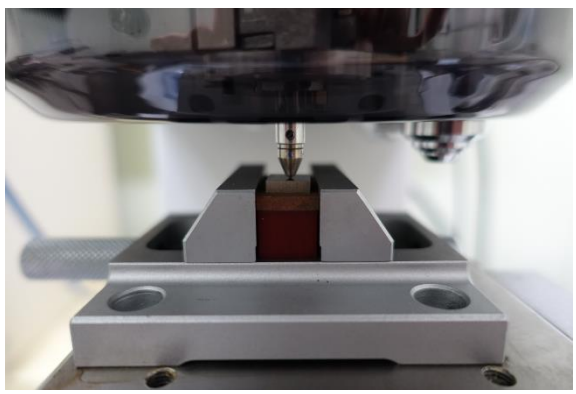

(b)

Figure 6.3 Photograph of Mitutoyo hardness testing machine: (a) testing machine and (b) hardness testing region.

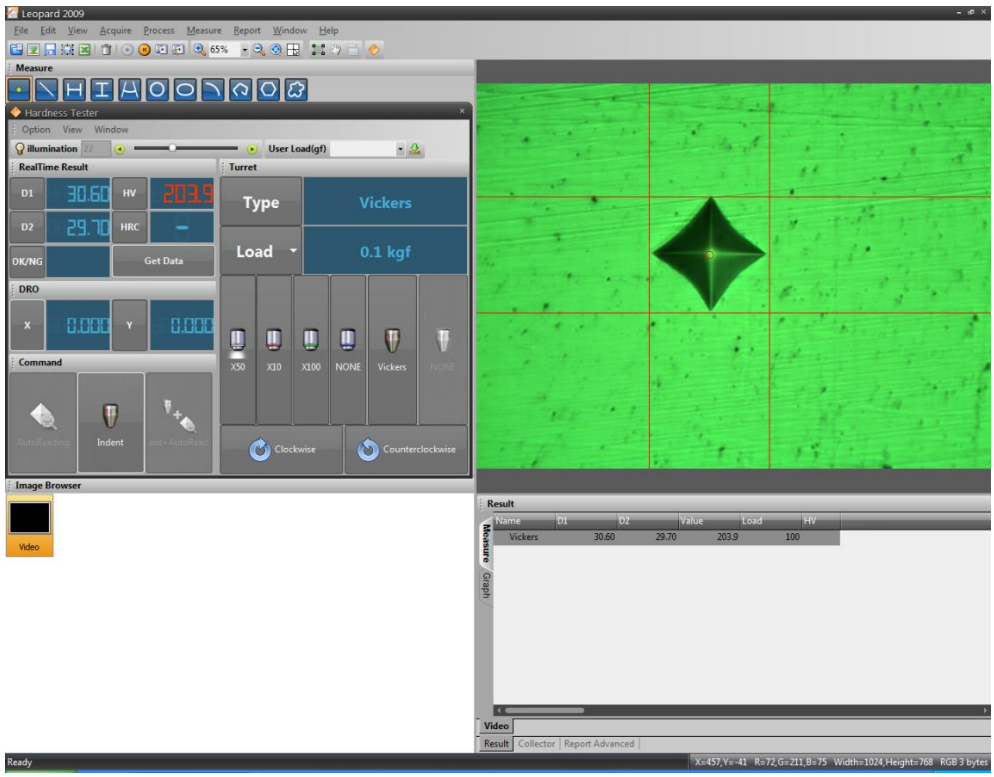

Figure 6.4 Leopard 2009 hardness measurement program.

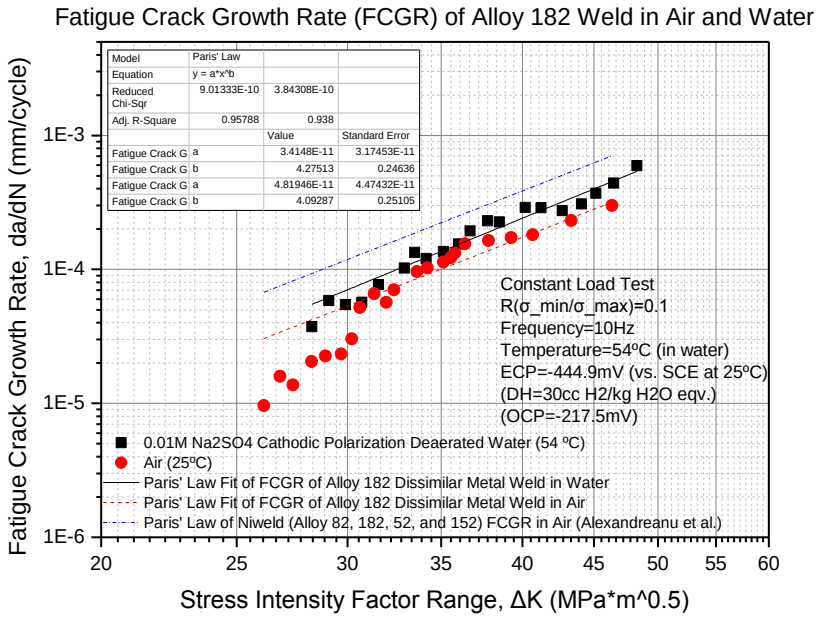

Figure 6.5 Effect of test low-temperature water chemistry on the fatigue crack growth behavior of alloy 182 dissimilar metal weld in 54℃ 0.01 M sodium sulfate deaerated water at an applied potential of -444.9 mV (vs. SCE at 25℃).

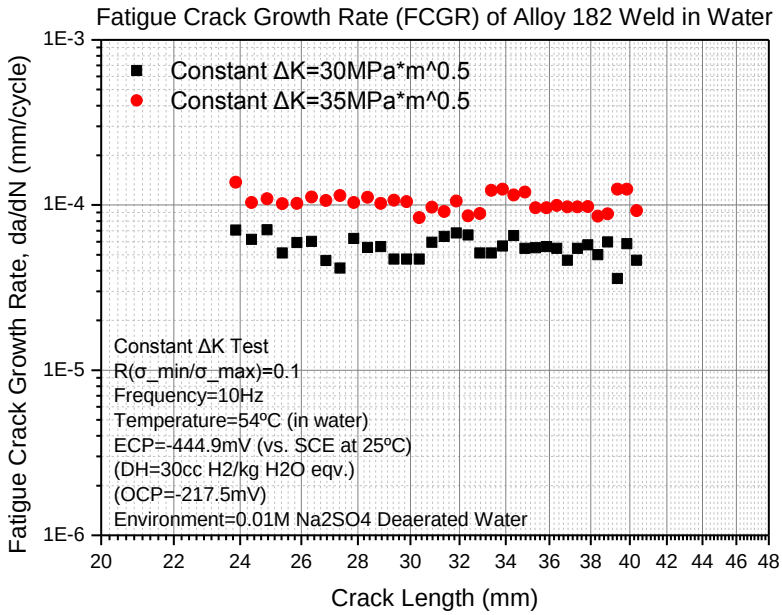

Figure 6.6 Fatigue crack growth rate versus crack length by constant ΔK test for Bayesian updating in low-temperature water chemistry of alloy 182 dissimilar metal weld in 54℃ 0.01 M sodium sulfate deaerated water at an applied potential of −444.9 mV (vs. SCE at 25℃).

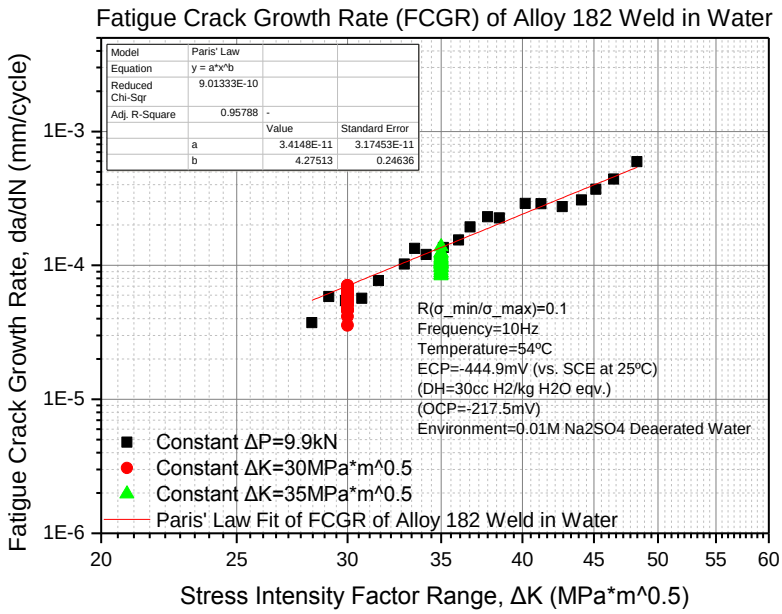

Figure 6.7 Fatigue crack growth rate versus stress intensity factor range of alloy 182 dissimilar metal weld by constant load test and constant ΔK test in 54℃ 0.01 M sodium sulfate deaerated water at an applied potential of −444.9 mV (vs. SCE at 25℃).

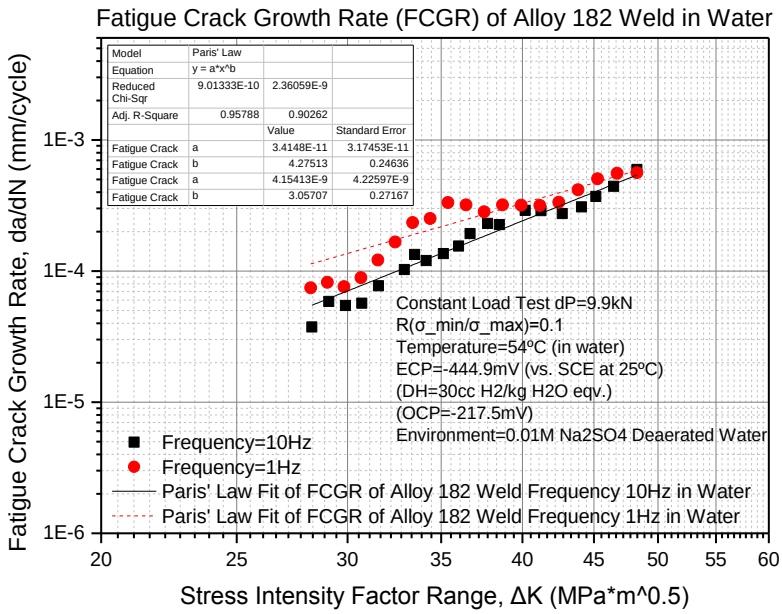

Figure 6.8 Effect of test frequency on the fatigue crack growth behavior of alloy 182 dissimilar metal weld in 54℃ 0.01 M sodium sulfate deaerated water at an applied potential of -444.9 mV (vs. SCE at 25℃).

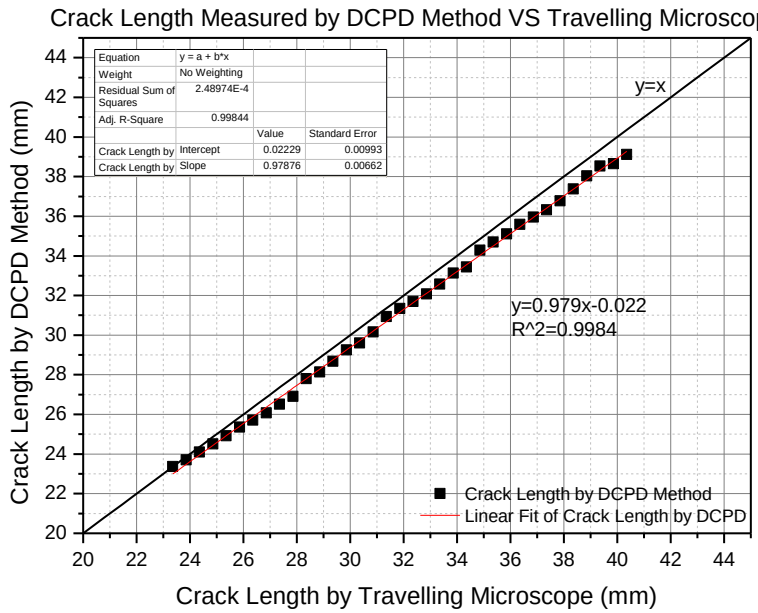

Figure 6.9 Crack length measured by direct current potential drop (DCPD) method versus crack length measured optically by travelling microscope.

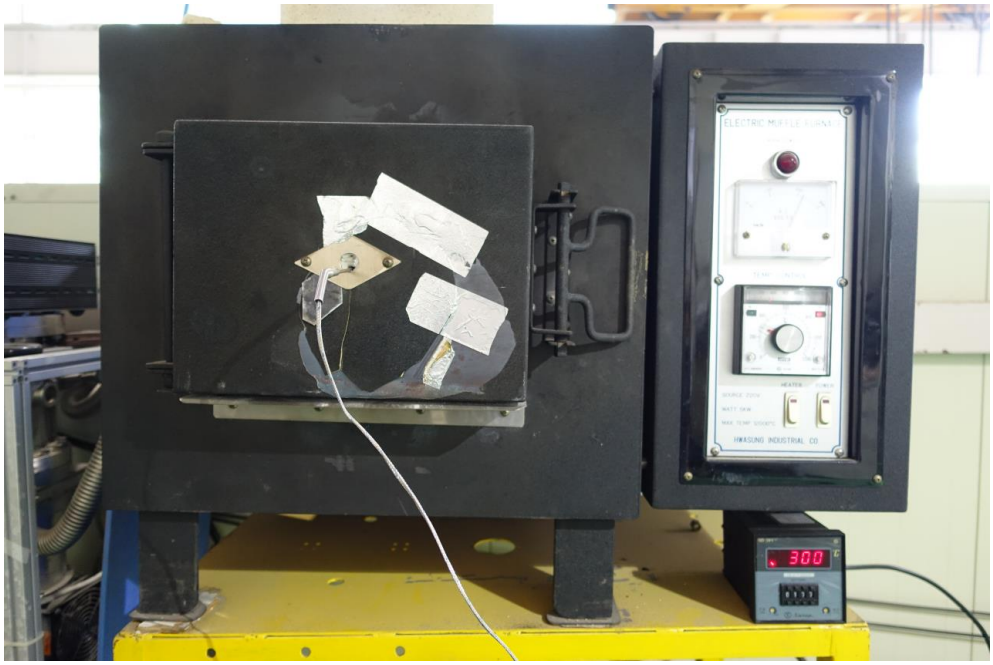

Figure 6.10 Furnace for heat tinting of specimen after fatigue testing.

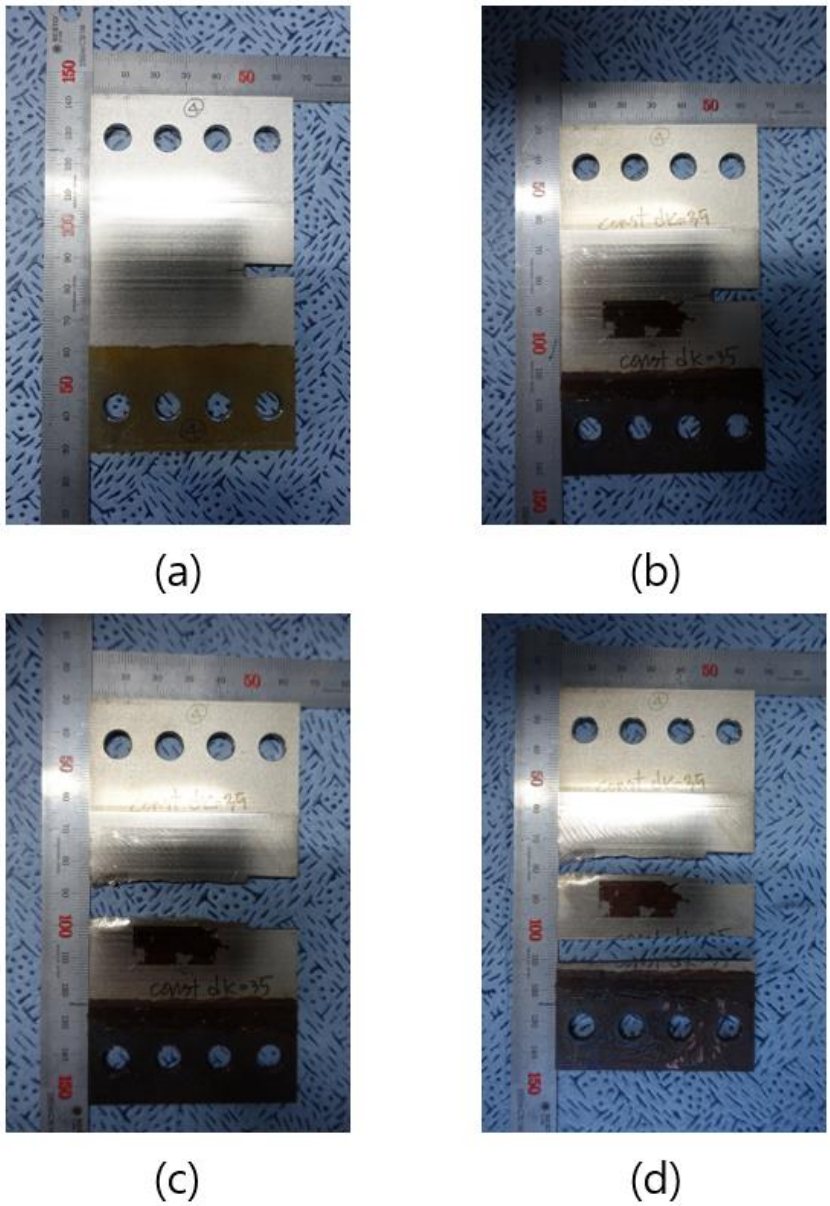

Figure 6.11 Testing specimen (a) before test, (b) after test, (c) after heat tinting and specimen separation, and (d) after saw cutting for FE-SEM analysis.

Figure 6.12 SIGMA field emission scanning electron microscope (FE-SEM).

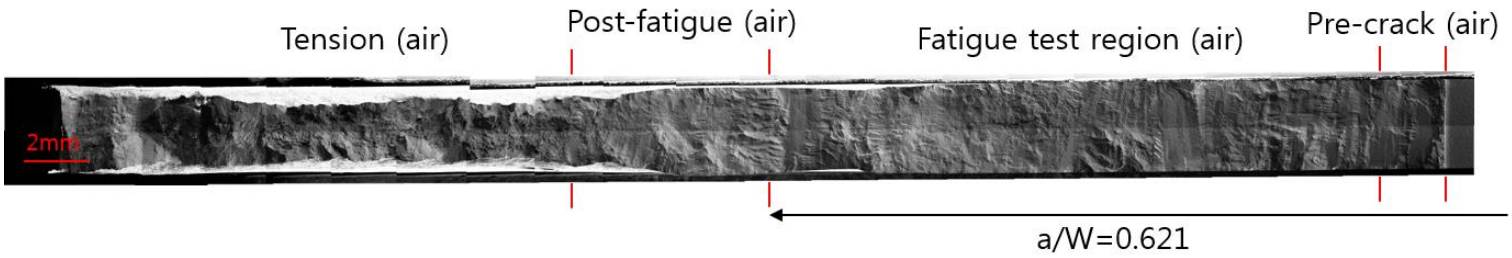

Figure 6.13 Fractograph of alloy 182 dissimilar metal weld in 25℃ air by constant load test by FE-SEM mosaic imaging (crack growth direction was right to left).

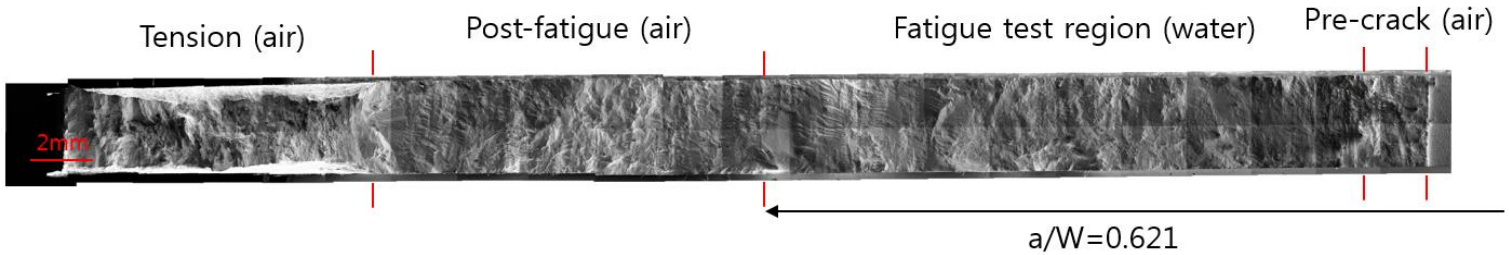

Figure 6.14 Fractograph of alloy 182 dissimilar metal weld in 54℃ water and an applied potential of -444.9 mV (vs. SCE at 25℃) by constant load test by mosaic imaging with FE-SEM (crack growth direction was right to left).

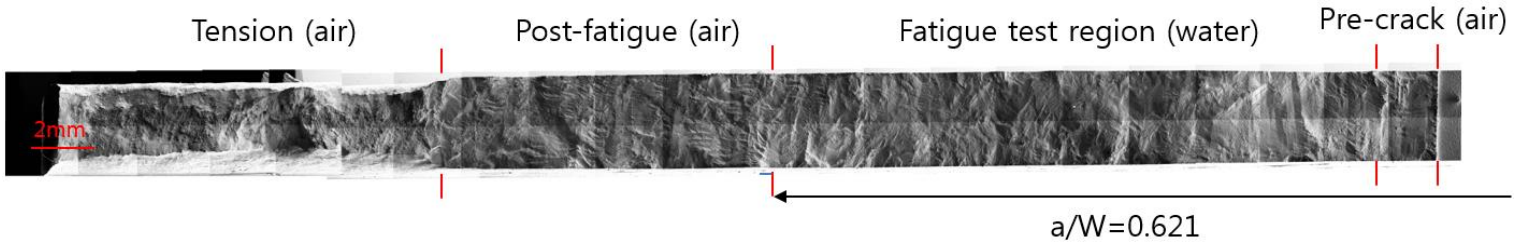

Figure 6.15 Fractograph of alloy 182 dissimilar metal weld in 54℃ water and an applied potential of -444.9 mV (vs. SCE at 25℃) by constant ΔK = 35 $\mathbf{MPa}\sqrt{m}$ test by mosaic imaging with FE-SEM (crack growth direction was right to left).

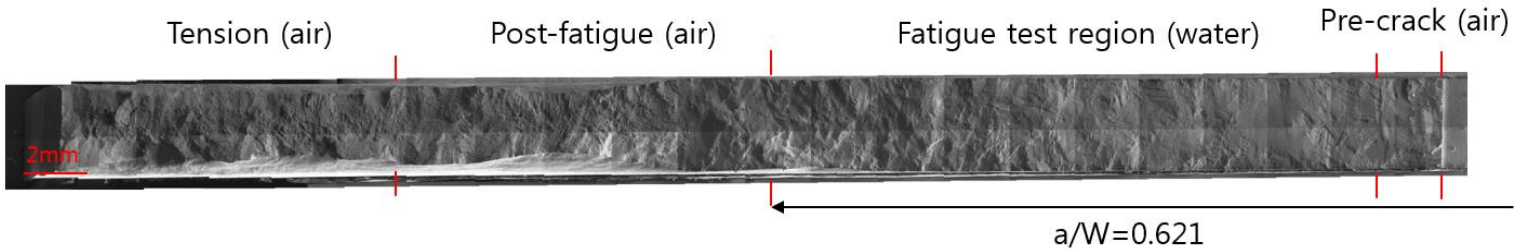

Figure 6.16 Fractograph of alloy 182 dissimilar metal weld of loading frequency 1 Hz in 54℃ water and an applied potential of -444.9 mV (vs. SCE at 25℃) by constant load test by mosaic imaging with FE-SEM (crack growth direction was right to left).

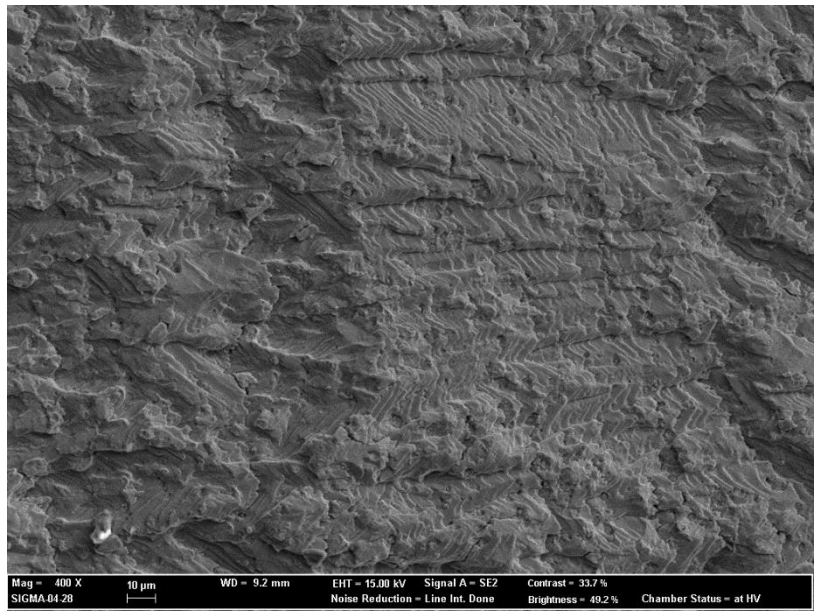

(a)

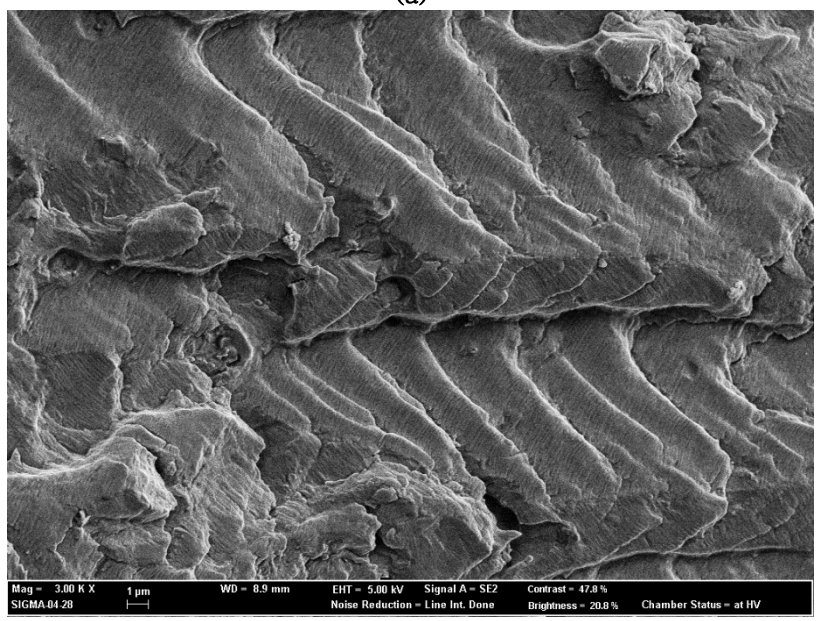

(b)

Figure 6.17 Fracture morphologies of alloy 182 dissimilar metal weld fatigue test region tested by constant load at 10 Hz in 25℃ air (crack growth direction was right to left): (a) 400x and (b) 3000x.

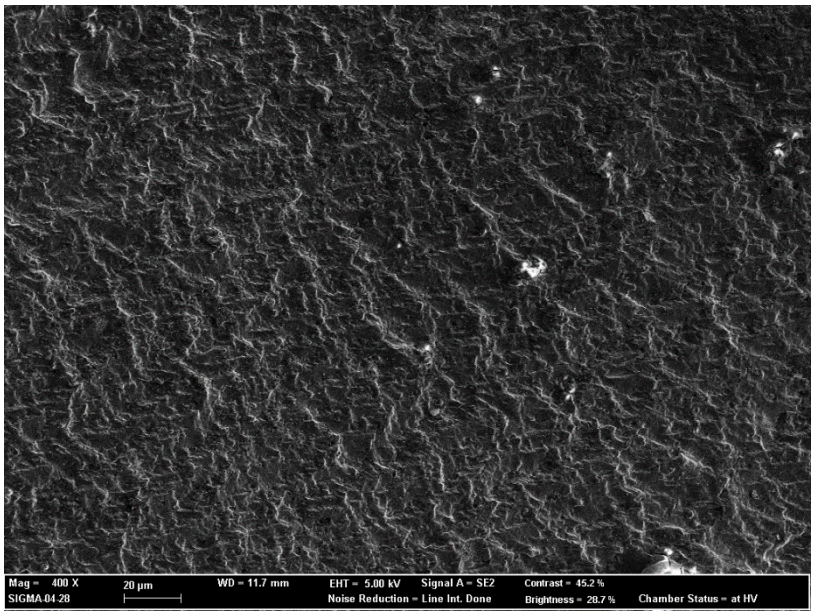

(a)

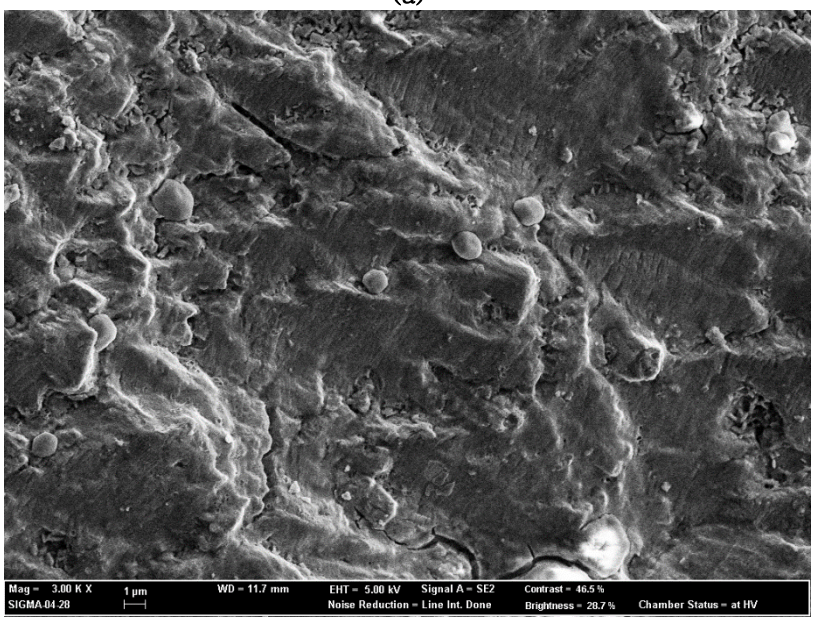

(b)

Figure 6.18 Fracture morphologies of alloy 182 dissimilar metal weld fatigue test region (near notch) tested by constant load at -444.9 mV (vs. SCE at 25℃) and 10 Hz in 54℃ 0.01 M sodium sulfate deaerated water (crack growth direction was right to left): (a) 400x and (b) 3000x.

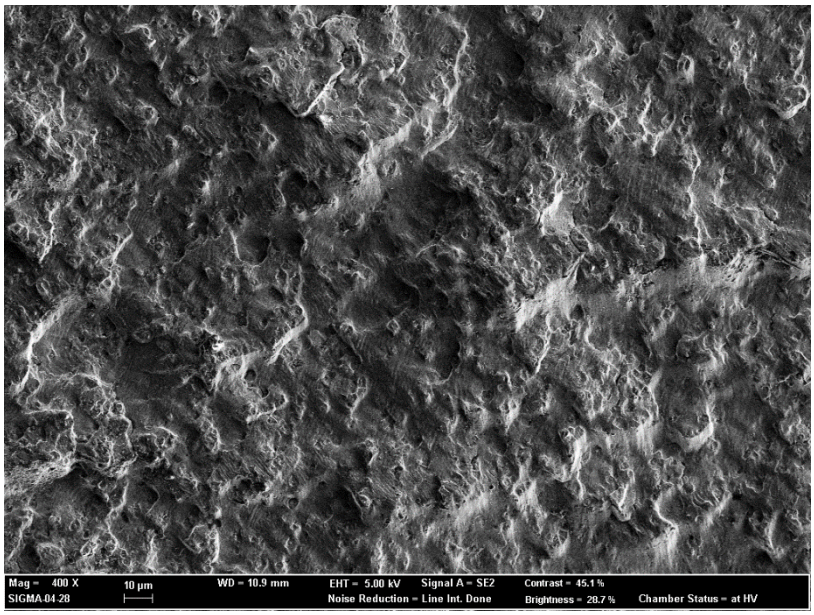

(a)

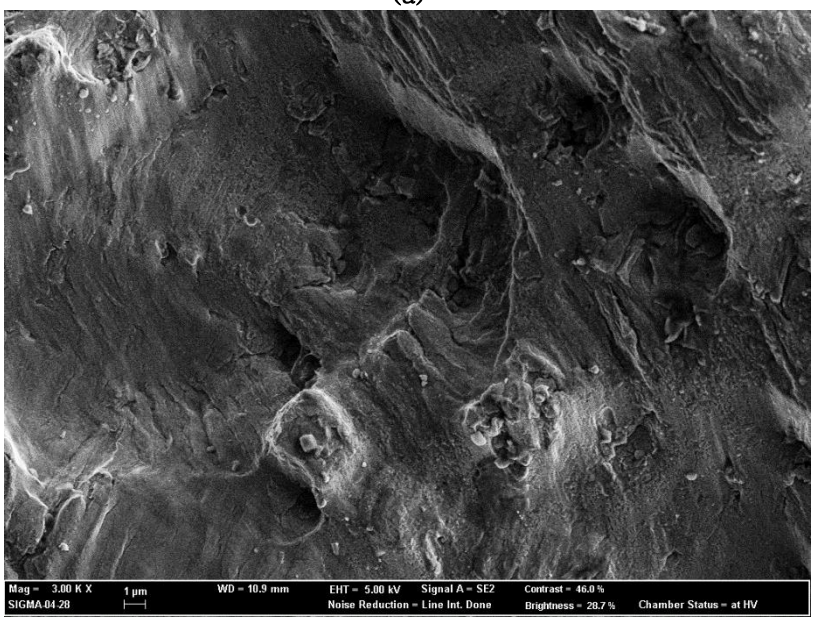

(b)

Figure 6.19 Fracture morphologies of alloy 182 dissimilar metal weld fatigue test region (far from notch) tested by constant load at -444.9 mV (vs. SCE at 25℃) and 10 Hz in 54℃ 0.01 M sodium sulfate deaerated water (crack growth direction was right to left): (a) 400x and (b) 3000x.

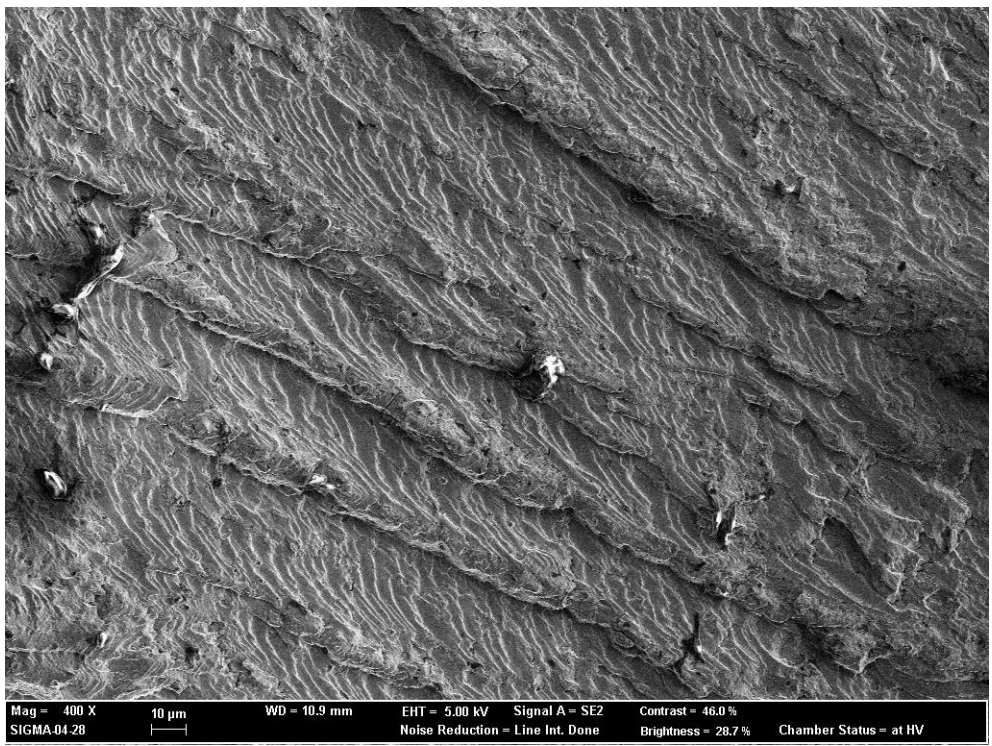

Figure 6.20 Fracture morphologies of alloy 182 dissimilar metal weld post-fatigue region in 25℃ air after the constant load fatigue test at 10 Hz in 54℃ water (crack growth direction was right to left).

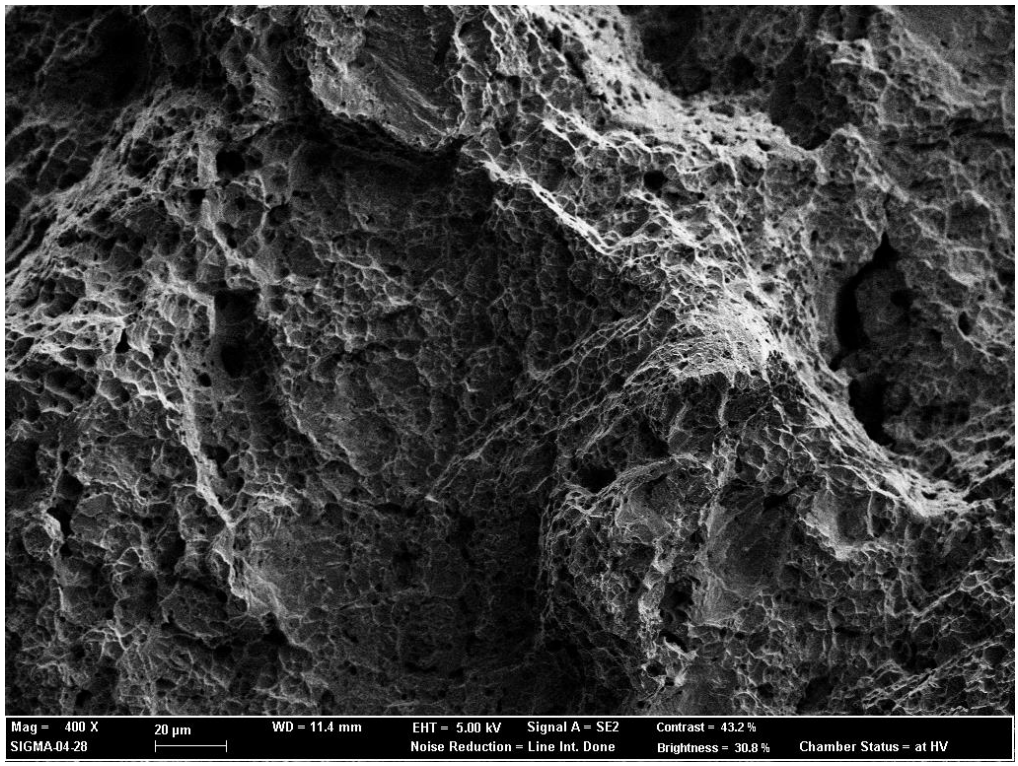

Figure 6.21 Fracture morphologies of alloy 182 dissimilar metal weld tensile region in 25℃ air after the constant load fatigue test at 10 Hz in 54℃ water (crack growth direction was right to left).

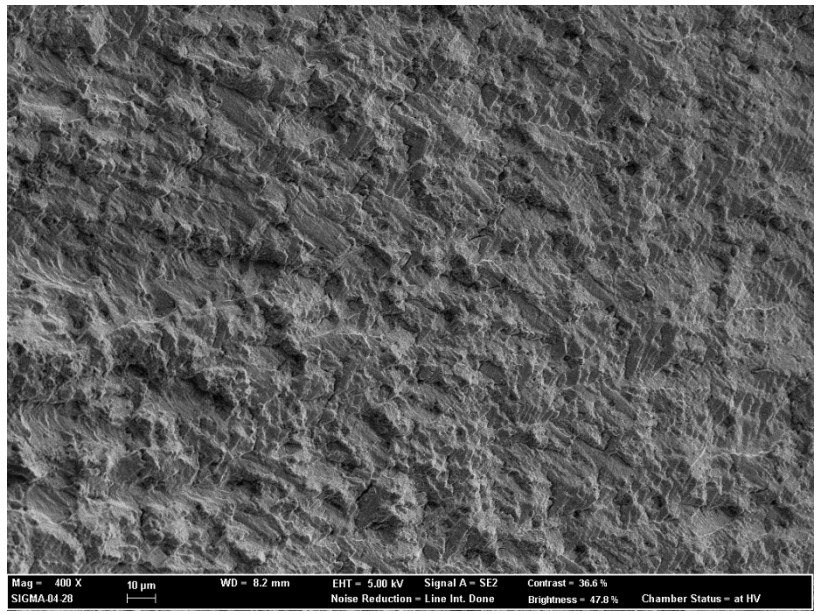

(a)

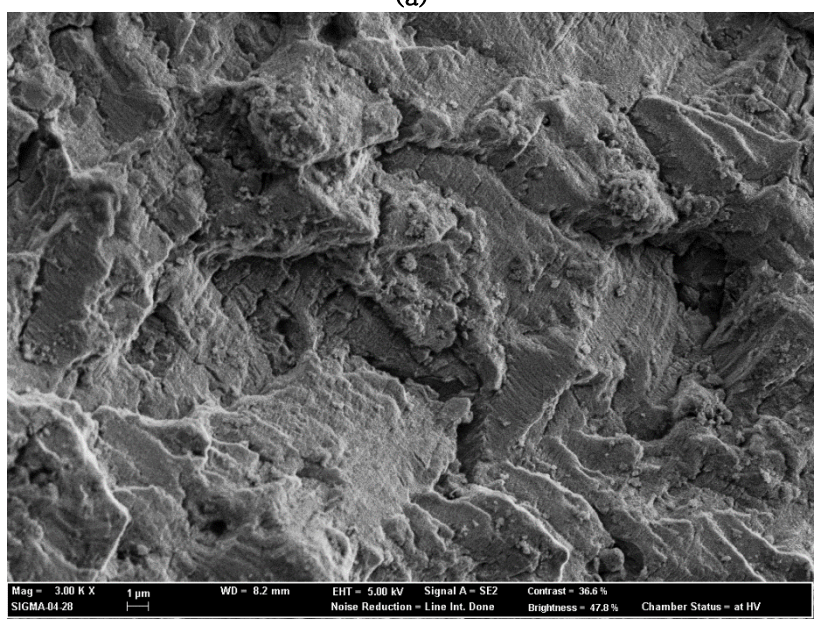

(a)

Figure 6.22 Fracture morphologies of alloy 182 dissimilar metal weld fatigue test region tested by constant ΔK = 35 $\mathbf{MPa}\sqrt{\boldsymbol{m}}$ at −444.9 mV (vs. SCE at 25℃) and 10 Hz in 54℃ 0.01 M sodium sulfate deaerated water (crack growth direction was right to left): (a) 400x and (b) 3000x.

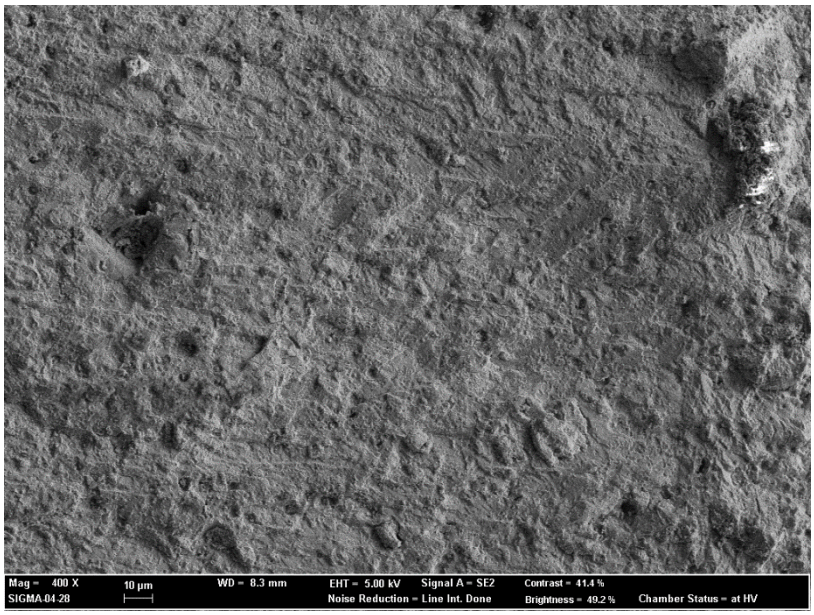

(a)

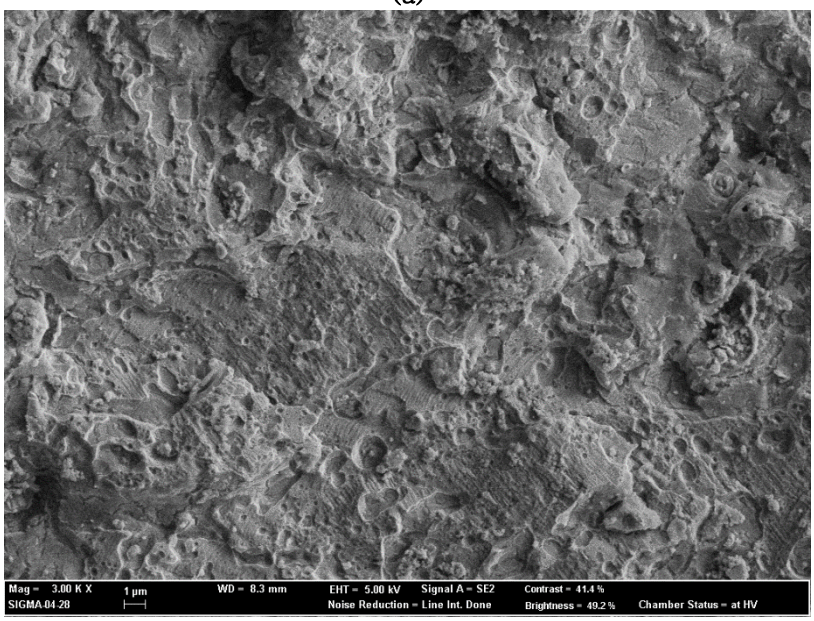

(b)

Figure 6.23 Fracture morphologies of alloy 182 dissimilar metal weld fatigue test region tested by constant load at -444.9 mV (vs. SCE at 25℃) and 1 Hz in 54℃ 0.01 M sodium sulfate deaerated water (crack growth direction was right to left): (a) 400x and (b) 3000x.

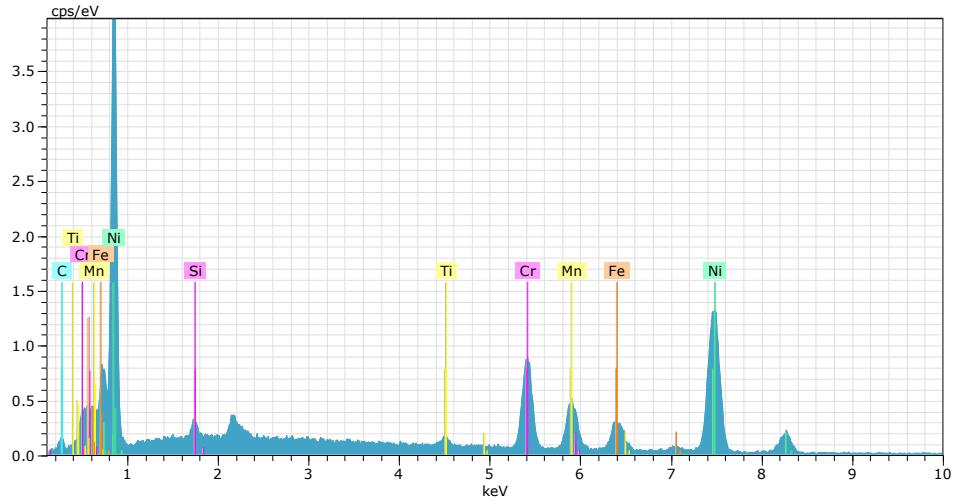

Figure 6.24 Energy dispersive X-ray spectroscopy (EDS) results of alloy 182 dissimilar metal weld before testing.

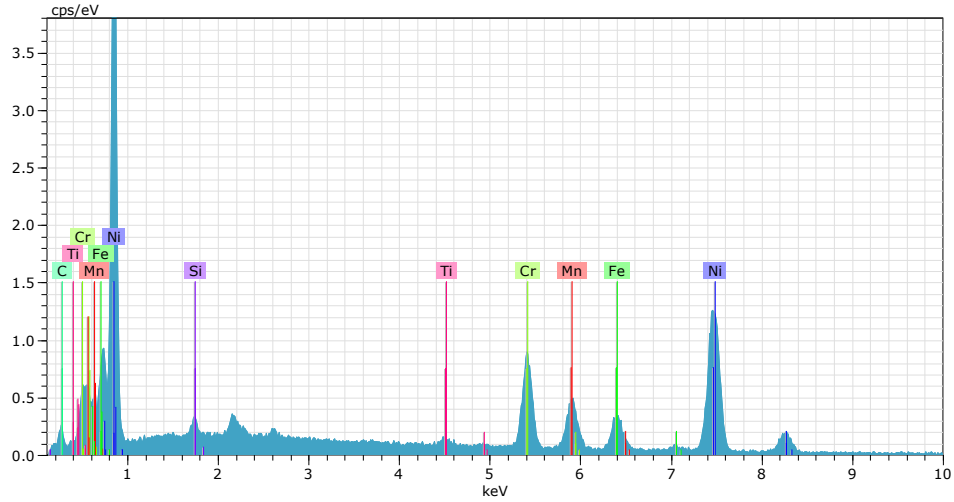

Figure 6.25 Energy dispersive X-ray spectroscopy (EDS) results of alloy 182 dissimilar metal weld after constant load testing in 25℃ air.

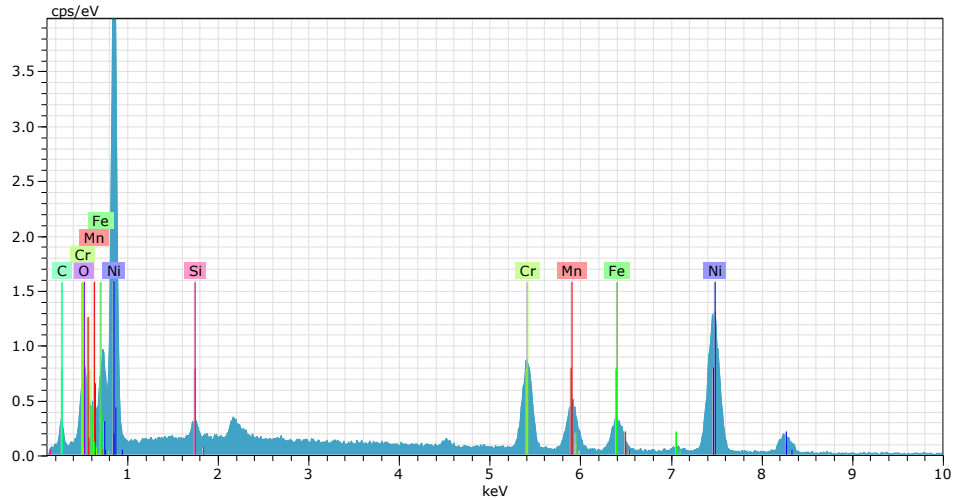

Figure 6.26 Energy dispersive X-ray spectroscopy (EDS) results of alloy 182 dissimilar metal weld after constant ΔK = 35 $\mathbf{MPa}\sqrt{m}$ testing at -444.9 mV (vs. SCE at 25℃) and 10 Hz in 54℃ 0.01 M sodium sulfate deaerated water.

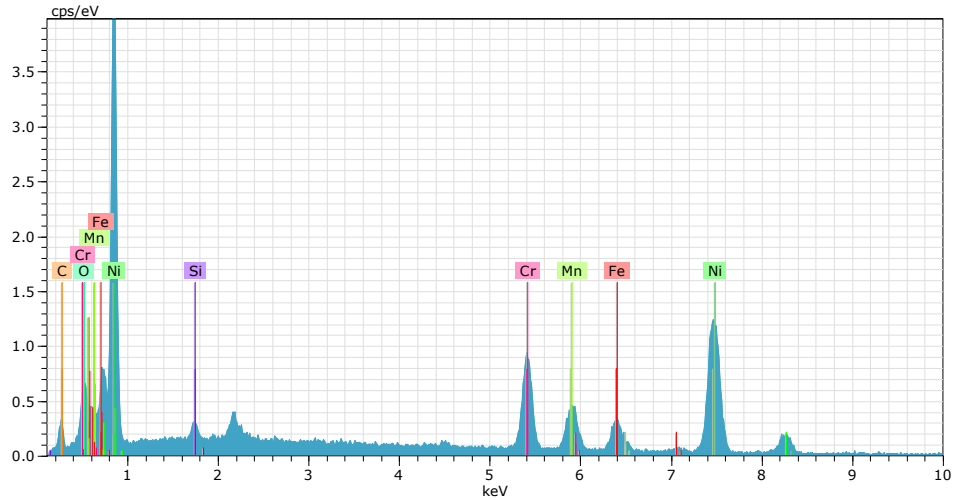

Figure 6.27 Energy dispersive X-ray spectroscopy (EDS) results of alloy 182 dissimilar metal weld after constant load testing at -444.9 mV (vs. SCE at 25℃) and 1 Hz in 54℃ 0.01 M sodium sulfate deaerated water.

Chapter 7 Bayesian Updating

The Bayesian theorem can be written as equation (7.1) to update the Paris law constants from the constant load test in low-temperature water and the likelihood from the constant ΔK test under the same conditions.

$$f(C,m|\dot{a}) = kL(C,m|\dot{a})f(C,m) \tag{7.1}$$

where $f(C,m)$ is the prior distribution of constants C and m, $f(C,m|\dot{a})$ is the posterior distribution of constants C and m, $L(C,m|\dot{a})$ is the likelihood function, and k is the normalizing constant.

In order to use equation (7.1), the uncertainty of the Paris law constants are assumed by normal (Gaussian) distribution because they can be derived several times in the same way. Then, the uncertainty distribution of constants C and m can be obtained using the probability density function (PDF). The PDF of a normal distribution is given in equation (7.2) [30].

$$f(C,m) = \frac{1}{\sigma\sqrt{2\pi}} e^{-\frac{(C,m-\mu_{C,m})^2}{2\sigma_{C,m}{}^2}} \tag{7.2}$$

where μ is the mean and σ is the standard deviation. Constants C and m were randomly sampled by Monte Carlo simulation using the cumulative distribution function (CDF) shown in equation (7.3) [30].

$$F(C,m) = \Phi\left(\frac{C,m-\mu_{C,m}}{\sigma_{C,m}}\right) = \frac{1}{2}\left[1+erf\left(\frac{C,m-\mu_{C,m}}{\sigma_{C,m}\sqrt{2}}\right)\right] \tag{7.3}$$

where $\Phi(x)=\frac{1}{2}\left[1+erf\left(\frac{x}{\sqrt{2}}\right)\right]$, $erf(x)=\frac{1}{\sqrt{\pi}}\int_{-x}^{x}e^{-t^2}dt$.

$L(C,m|\dot{a})=f(\dot{a}|\mathrm{C},\mathrm{m})$ used in equation (7.1) is the likelihood function. It was assumed that the distribution of $x_i-\dot{a}(C,m)$ was $N(0,\sigma^2)$ in this study, where x_i is the i−th fatigue crack growth rate obtained through the constant ΔK test in low−temperature water. The likelihood function is given as equation (7.4).

$$L(C,m\,|\,\dot{a})=\prod_{i=1}^{n}\frac{1}{\sigma\sqrt{2\pi}}e^{-\frac{\left[\left(x_i-\dot{a}(C,m)\right)-0\right]^2}{2\sigma^2}} \tag{7.4}$$

where σ is the standard deviation of $x_i-\dot{a}$.

Through equation (7.2), the normalized sampled uncertainty distribution of the Paris law constants C and m under the constant load test in low−temperature water at 10 Hz is shown in Figure 7.1.

The normalized likelihood using equation (7.4) of each of the sampled values of the Paris law constant C under the constant ΔK = 30 $\mathrm{MPa}\sqrt{m}$ test in low−temperature water at 10 Hz is shown in Figure 7.2(a). The posterior probability density was solved by multiplying the corresponding probability density of the prior distribution and the likelihood of each value of C. The normalized posterior distribution and prior distribution is shown in Figure 7.2(b). After updating C, the constant m was updated in the same way with the likelihood obtained by the fatigue crack growth rate data of the constant ΔK = 35 $\mathrm{MPa}\sqrt{m}$ test. The normalized likelihood distribution and normalized prior and posterior distribution of constant m are shown in Figure 7.3.

The Bayesian updating program was made by using the MATLAB program. The initial constant C value was updated by the

fatigue crack growth rate data of the constant ΔK = 30 $\mathrm{MPa}\sqrt{m}$ test with the value of the constant m fixed. Then, the constant m was updated using the fatigue crack growth rate data of the constant ΔK = 35 $\mathrm{MPa}\sqrt{m}$ test with the value of the constant C fixed. Also, the Paris law constants of the first update of constant m with the data of constant ΔK = 30 $\mathrm{MPa}\sqrt{m}$ and the second update of constant C with the data of constant ΔK = 35 $\mathrm{MPa}\sqrt{m}$ were calculated. All the updated Paris law constants are listed in Table 7.1.

In Table 7.1, “prior” is the initial mean and standard deviation of the Paris law constants. “Sampled prior” is the mean and standard deviation of the random sampled values using Monte Carlo simulation. In the table, updating C before m is shown in the dark blue region, in which $C = 2.69\times10^{-11}$ and m = 4.27. Updating m before C is shown in the bright green region, in which $C = 3.37\times10^{-11}$ and m = 4.20. The two updated Paris law plot of the constant C and m values were almost the same. The standard deviation of the updated Bayesian results decreased dramatically, as shown in Table 7.1. The Paris law plot of the updated constant C and that of the updated C and m is shown in Figure 7.4.

Table 7.1 Bayesian updated Paris law constants C and m using constant ΔK test

Step 1	C by ΔK = 30 $\text{MPa}\sqrt{m}$		m by ΔK = 30 $\text{MPa}\sqrt{m}$	
	Mean	STD	Mean	STD
Prior	3.41×10^{-11}	3.17×10^{-11}	4.28	2.46×10^{-1}
Sampled Prior	3.42×10^{-11}	3.18×10^{-11}	4.28	2.47×10^{-1}
Posterior (m fixed)	2.69×10^{-11}	2.08×10^{-24}	4.28	2.46×10^{-1}
Posterior (C fixed)	3.41×10^{-11}	3.17×10^{-11}	4.20	2.49×10^{-4}
Step 2	m after C by ΔK = 35 $\text{MPa}\sqrt{m}$		C after m by ΔK = 35 $\text{MPa}\sqrt{m}$	
	Mean	STD	Mean	STD
Prior	4.28	2.46×10^{-1}	3.41×10^{-11}	3.17×10^{-11}
Sampled Prior	4.28	2.47×10^{-1}	3.42×10^{-11}	3.18×10^{-11}
Posterior (m fixed)	4.28	2.46×10^{-1}	3.37×10^{-11}	5.15×10^{-25}
Posterior (C fixed)	4.27	3.75×10^{-5}	3.41×10^{-11}	3.17×10^{-11}

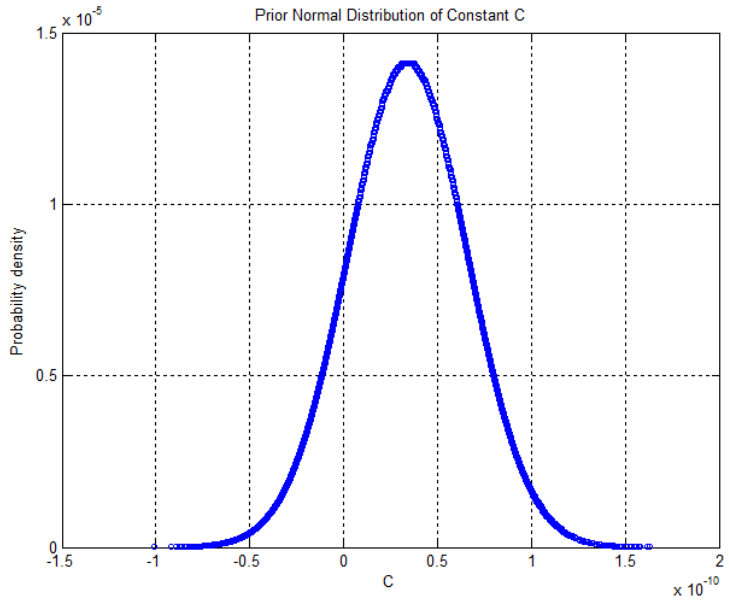

(a)

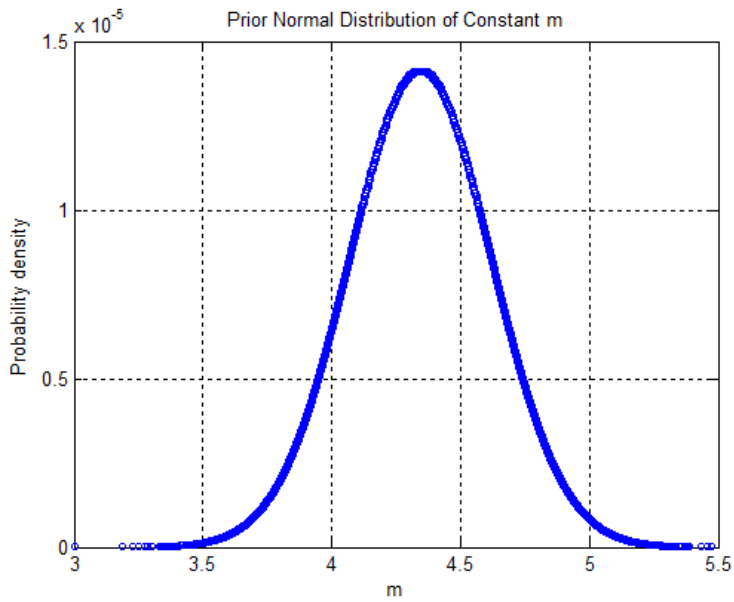

(b)

Figure 7.1 Prior distribution of Paris law constants (a) C and (b) m.

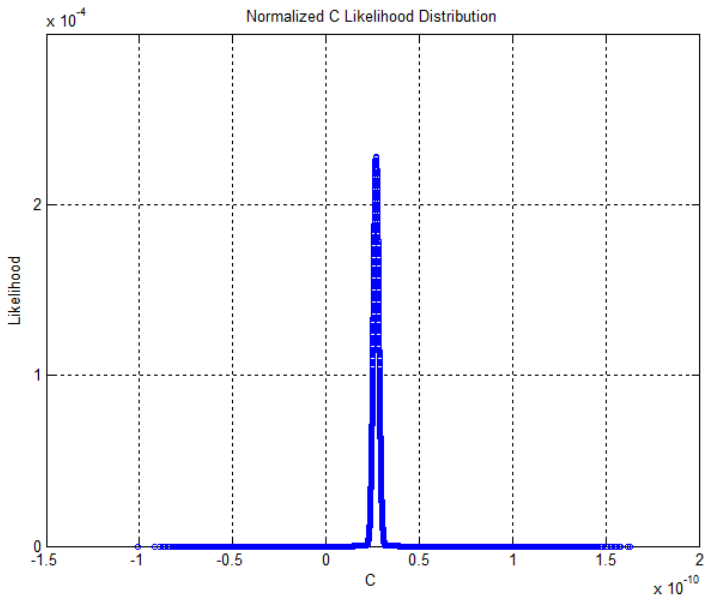

(a)

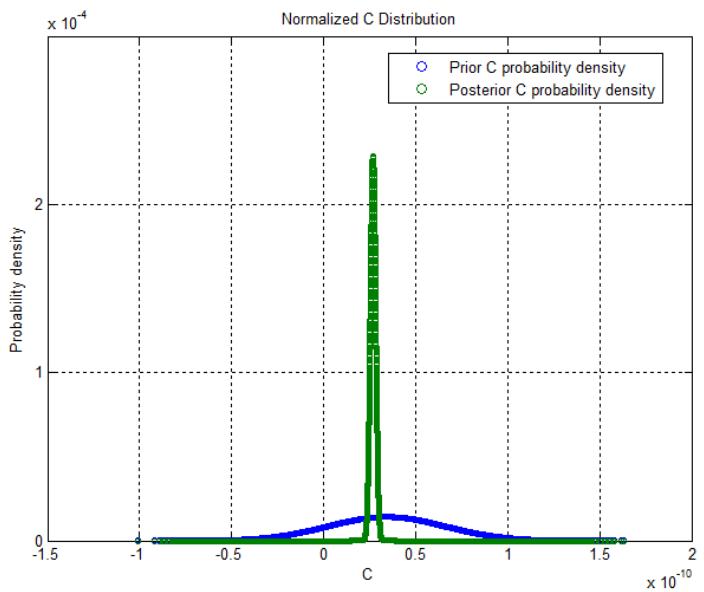

(b)

Figure 7.2 Likelihood, prior, and posterior distribution of constant C updated with $\Delta K = 30\ \mathbf{MPa}\sqrt{\boldsymbol{m}}$ test data: (a) likelihood distribution and (b) prior and posterior distribution.

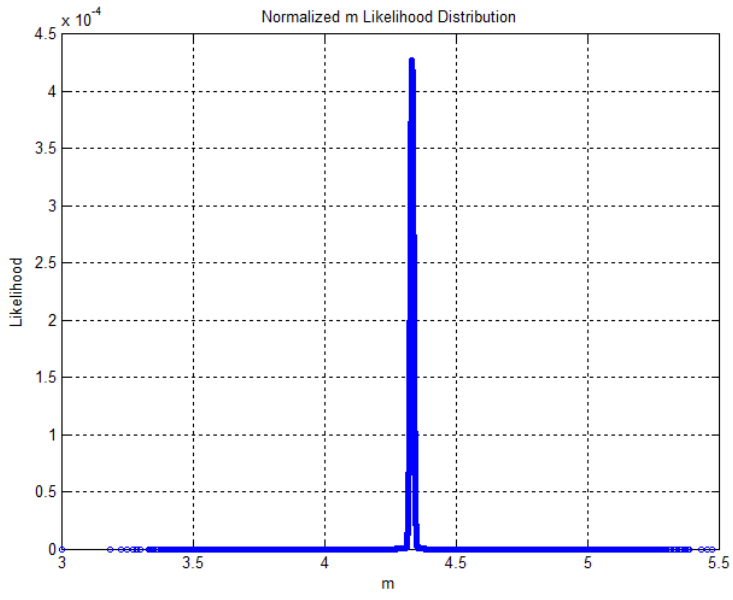

(a)

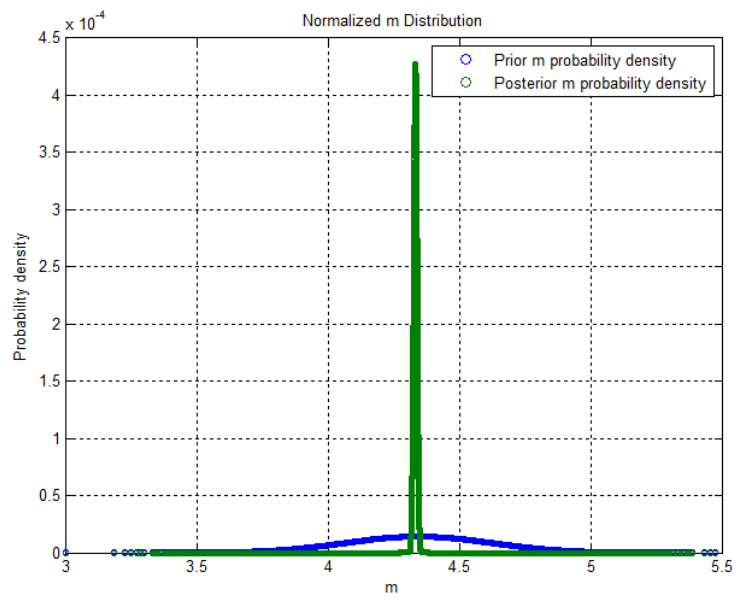

(b)

Figure 7.3 Likelihood, prior, and posterior distribution of constant m updated with $\Delta K = 35$ **MPa**$\sqrt{m}$ test data: (a) likelihood distribution and (b) prior and posterior distribution.

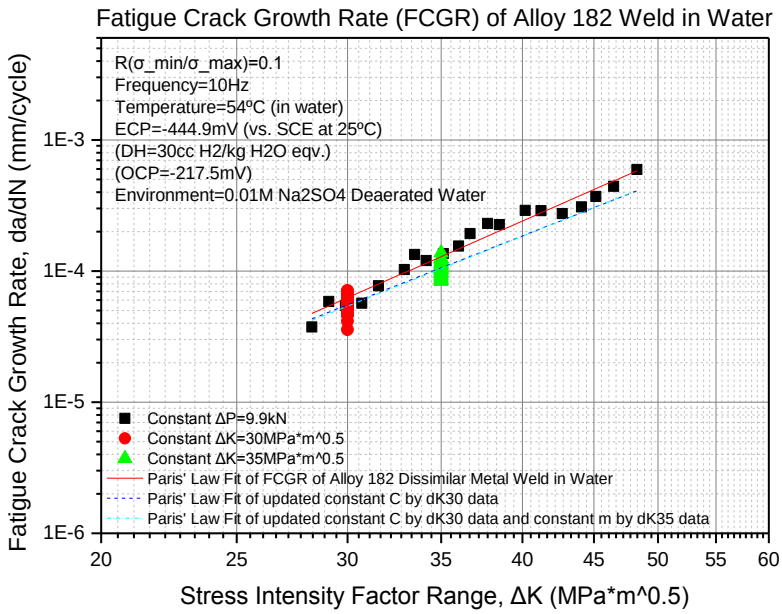

Figure 7.4 Bayesian-updated Paris law model at -444.9 mV (vs. SCE at 25℃) and 10 Hz in 54℃ 0.01 M sodium sulfate deaerated water. Blue dash line is constant C updated by the likelihood derived from the constant ΔK = 30 $\mathbf{MPa}\sqrt{\boldsymbol{m}}$ test, the cyan dash-dot line is constant C updated by the likelihood derived from the constant ΔK = 30 $\mathbf{MPa}\sqrt{\boldsymbol{m}}$ test and constant m by the likelihood derived from the constant ΔK = 35 $\mathbf{MPa}\sqrt{\boldsymbol{m}}$ test.

Chapter 8 Conclusions and Future Work

8.1 Conclusions

Through this thesis, it was confirmed that the fatigue crack growth rate of an alloy 182 dissimilar metal weld increased in low-temperature water with dissolved hydrogen.

It was confirmed that the uncertainty of the Paris law constants of the alloy 182 dissimilar metal weld was affected by the welding conditions and surrounding environment. The uncertainty was reduced dramatically by using a probabilistic method using Bayesian inference. The results showed that even when data for the Paris law model are scarce, the constants can be accurately updated by a laboratory-scale experiment considering welding conditions and the surrounding environment.

In addition, Striation markings were confirmed in the fracture morphology taken by using FE-SEM when the fatigue crack grew. Also, corrosion had more of an effect when the fatigue loading frequency was lower.

It was confirmed that it is possible to update a value that is difficult to measure directly by the probabilistic method using Bayesian inference. The new method therefore gives updated results that take into consideration the material and the surrounding environment as a conventionally calculated deterministic method.

If data is scarce, the Paris law constants for a domestic nuclear power plant can be updated accurately in accordance with ASME Boiler and Pressure Vessel Code Section XI using this probabilistic method with data from a laboratory-scale experiment. Especially, the mechanical properties of the welding region can vary depending

on the welding conditions and the surrounding environment. Therefore, this method is a very useful tool for long-term nuclear safety and evaluation of the integrity of the structural materials of nuclear power plants.

8.2 Future Work

A dissolved hydrogen environment was created by an applied potential of −444.9 mV equivalent to 30 cc H_2/kg H_2O in this study. Experiments increasing or decreasing the concentration of dissolved hydrogen in the water by changing the applied potential could be done to determine the effect of dissolved hydrogen.

To find out the effect of loading frequency, a 1 Hz test was performed in this study; loading frequencies of 0.1 Hz or 0.01 Hz could be used in the future to determine the effect of low frequencies on corrosion. The effect of wave-form, stress ratio R, thermal treatment, etc. could also be checked to see how the results change.

Governing equations similar to the Paris law model can be checked to see if Bayesian inference can be applied to them or not.

Finally, Bayesian updating could be done with other than normal distributions to determine how to choose the appropriate distribution and how to do a conformity assessment of the distribution.

Bibliography

[1] IAEA PRIS. (2015, Nov., 8th). *Operational Reactors by Age* Available: https://www.iaea.org/PRIS/WorldStatistics/OperationalByAge.aspx

[2] ASME, "Boiler and Pressure Vessel Code Section XI: Rules for Inservice Inspection of Nuclear Power Plant Components," *The American Society of Mechanical Engineers,* 1992.

[3] J. W. Kim, K. S. Lee, and C. Y. Park, "Evaluation of Mechanical Properties of Alloy 82/182 Weld Joint Between SA508 Gr. 3 Nozzle and F316L Safe-End," 2010.

[4] K. S. Lee, S. H. Lee, and J. W. Kim, "A Study for Experiment to Measure Mechanical Properties of Pressurizer Nozzle and Safety-Ends in Nuclear Power Plant," *Journal of the Korean Society for Nondestructive Testing,* vol. 33, pp. 147-153, 2013.

[5] B. Alexandreanu, O. K. Chopra, and W. J. Shack, "Crack Growth Rates in a PWR Environment of Nickel Alloys from the Davis-Besse and V. C. Summer Power Plants (NUREG/CR-6921)," 2006.

[6] A. Demma, A. Mellree, and M. Herrera, "Low Temperature Crack Propagation Evaluation in Pressurized Water Reactor Service," in *12th International Symposium on Environmental Degradation of Materials in Nuclear Systems*, 2005, pp. 623-637.

[7] M. A. Meyers and K. K. Chawla, *Mechanical Behavior of Materials*, 2nd ed. Cambridge; New York: Cambridge University Press, 2009.

[8] C. Amzallag, G. Baudry, and J. Bernard, "Effects of PWR Environment on the Fatigue Crack Growth of Different Stainless Steels and Inconel Type Alloy," 1983.

[9] B. Alexandreanu, O. K. Chopra, and W. J. Shack, "Crack Growth Rates and Metallographic Examinations of Alloy 600 and Alloy 82/182 from Field Components and Laboratory Materials Tested in PWR Environments (NUREG/CR-6964)," 2008.

[10] M. Ahonen, "Collation of LTCP Test Results Obtained in Years 2008-2012," 2013.

[11] EPRI, "Program on Technology Innovation: Scoping Study of Low Temperature Crack Propagation for 182 Weld Metal in BWR Environments and for Cast Austenitic Stainless Steel in PWR Environments (Revision 1)," EPRI, Palo Alto, CA, 2010.

[12] K. M. Ramachandran and C. P. Tsokos, *Mathematical Statistics with Applications*. Amsterdam: Academic Press/Elsevier, 2009.

[13] A. Gelman, J. B. Carlin, H. S. Stern, D. B. Dunson, A. Vehtari, and D. B. Rubin, *Bayesian Data Analysis*, 3rd ed. Boca Raton; London; New York: CRC Press, 2013.

[14] I. M. Sobol, *A Primer for the Monte Carlo Method*. Boca Raton: CRC press, 1994.
[15] C. Jang, J. Lee, J. S. Kim, and T. E. Jin, "Mechanical Property Variation within Inconel 82/182 Dissimilar Metal Weld between Low Alloy Steel and 316 Stainless Steel," *International Journal of Pressure Vessels and Piping,* vol. 85, pp. 635-646, 2008.
[16] ASTM. E647-13ae1, Standard Test Method for Measurement of Fatigue Crack Growth Rates [Online]. Available: www.astm.org
[17] G. S. Was and R. G. Ballinger, "Hydrogen Induced Cracking under Cyclic Loading of Nickel Base Alloys Used for PWR Steam Generator Tubing," *Fourth Semi-annual Progress Report, EPRI NP-4613,* 1980.
[18] I. S. Hwang, "Embrittlement Mechanisms of Nickel-base Alloys in Water," Dissertation, Department of Nuclear Engineering, Massachusetts Institute of Technology, Boston, 1987.
[19] J. Y. Yoon, "Modeling of the Corrosion Fatigue Crack Growth Rate for Ni-base Alloy X-750," Thesis, Seoul National University, Seoul, 2012.
[20] KETEP, I. S. Hwang, and J. Y. Yoon, "Development of Array Probe DCPD (Direct Current Potential Drop) Technique for Online Monitoring of Nuclear Piping Welds," KETEP (Korea Institute of Energy Technology Evaluation and Planning), 2015.
[21] ASTM. E8/E8M-15a, Standard Test Methods for Tension Testing of Metallic Materials [Online]. Available: www.astm.org
[22] ASTM. E399-12e3, Standard Test Method for Linear-Elastic Plane-Strain Fracture Toughness KIc of Metallic Materials [Online]. Available: www.asme.org
[23] D. C. Zipperian, *Metallographic Handbook*. Tucson, Arizona USA: Pace Technologies, 2011.
[24] K.-H. Schwalbe and D. Hellmann, "Application of the Electrical Potential Method to Crack Length Measurements Using Johnson's Formula," *Journal of Testing and Evaluation, JTEVA,* vol. 9, pp. 218-221, 1981.
[25] D. A. Jones, *Principles and Prevention of Corrosion*, 2nd ed. Upper Saddle River, NJ: Prentice Hall, 1992.
[26] D. Himmelblau, "Solubilities of Inert Gases in Water: 0°C to Near the Critical Point of Water," *Journal of Chemical and Engineering Data,* vol. 5, pp. 10-15, 1960.
[27] D. C. Harris, *Quantitative Chemical Analysis*, 7th ed. New York: W. H. Freeman and Company, 2007.
[28] M. Hayashi, "Thermal Fatigue Strength of Type 304 Stainless Steel in Simulated BWR Environment," *Nuclear Engineering and Design,*

vol. 184, pp. 135-144, 1998.
[29] ASTM. E1820-13e1, Standard Test Method for Measurement of Fracture Toughness [Online]. Available: www.astm.org
[30] B. M. Ayyub and R. H. McCuen, *Probability, Statistics, and Reliability for Engineers and Scientists*, 3rd ed. Boca Raton, FL: CRC Press, 2011.

Appendix A Welding Record of Procedure Qualification of Alloy 182 Dissimilar Metal Weld

WELDING RECORD OF PROCEDURE QUALIFICATION
시 험 용 접 기 록 서

Pass No.	Filler Metal Type	Heat or Lot No.	Size (Φ)	Temp. Max.(℃)	Peak Amps	Base Amps (A)	Volts (V)	Wire Feeding (cm/min)	Speed (cm/min)
1	ENiCrFe-3	K60	3.2	135	-	90~100	23~26	-	11~13
2	"	"	"	126	-	"	"	-	"
3	"	"	"	137	-	"	"	-	"
4	"	"	"	145	-	"	"	-	"
5	"	"	"	148	-	"	"	-	"
6	"	"	"	158	-	"	"	-	"
7	"	"	"	166	-	"	"	-	"
8	"	"	"	170	-	"	"	-	"
9	"	"	"	158	-	"	"	-	"
10	"	"	"	143	-	"	"	-	"
11	"	"	"	160	-	"	"	-	"
12	"	"	"	125	-	"	"	-	"
13	"	"	"	136	-	"	"	-	"
14	"	"	"	149	-	"	"	-	"
15	"	"	"	168	-	"	"	-	"
16	"	"	"	152	-	"	"	-	"
17	"	"	"	143	-	"	"	-	"
18	"	"	"	154	-	"	"	-	"
19	"	"	"	165	-	"	"	-	"
20	"	"	"	171	-	"	"	-	"
21	"	"	"	123	-	"	"	-	"
22	"	"	"	135	-	"	"	-	"
23	"	"	"	150	-	"	"	-	"

보성기업

Test No.	:	S-Buttering
Page :	:	1 of 2

Pass Sequence

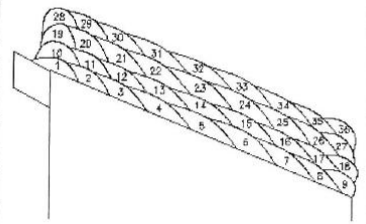

Process	:	SMAW
Coupon Size	:	t40x200Wx400L
Position	:	1G
Material Spec.	:	SA508Gr 3Cl.1
Frequency	:	N/A
Polarity	:	DCRP
Shielding Gas	:	N/A
Gas Flow Rate	:	N/A
Tungsten Electrode	:	N/A
Filler Matal	:	WEL DC 182(Nippon Welding)
Flux	:	N/A
Welding Engineer	:	Y.H Lee
Welder	:	S.W.Sung
Date	:	2013.4.20~4.21

WELDING RECORD OF PROCEDURE QUALIFICATION

시 험 용 접 기 록 서

Pass No.	Filler Metal Type	Heat or Lot No.	Size (Φ)	Temp. Max.(℃)	Peak Amps	Base Amps (A)	Volts (V)	Wire Feeding (cm/min)	Speed (cm/min)
24	ENiCrFe-3	K60	3.2	162	-	90~100	23~26	-	11~13
25	"	"	"	147	-	"	"	-	"
26	"	"	"	135	-	"	"	-	"
27	"	"	"	145	-	"	"	-	"
28	"	"	"	151	-	"	"	-	"
29	"	"	"	167	-	"	"	-	"
30	"	"	"	171	-	"	"	-	"
31	"	"	"	137	-	"	"	-	"
32	"	"	"	143	-	"	"	-	"
33	"	"	"	153	-	"	"	-	"
34	"	"	"	147	-	"	"	-	"
35	"	"	"	160	-	"	"	-	"
36	"	"	"	165	-	"	"	-	"

후열 : 210~290℃x2hrs

이하여백

Test No. : S-Buttering

Page : : 2 of 2

Pass Sequence

Process :

Coupon Size :

Position :

Material Spec. :

Frequency :

Polarity :

Shielding Gas :

Gas Flow Rate :

Tungsten Electrode :

Filler Matal :

Flux :

Welding Engineer :

Welder :

Date :

보성기업

WELDING RECORD OF PROCEDURE QUALIFICATION

시 험 용 접 기 록 서

Pass No.	Filler Metal Type	Heat or Lot No.	Size (Φ)	Temp. Max.(℃)	Peak Amps	Base Amps (A)	Volts (V)	Wire Feeding (cm/min)	Speed (cm/min)
1	ENiCrFe-3	K60	3.2	45	-	60~70	21~24	-	10~11
2	"	"	"	48	-	70~90	22~25	-	11~12
3	"	"	"	52	-	"	"	-	"
4	"	"	"	64	-	90~100	23~26	-	11~13
5	"	"	"	85	-	"	"	-	"
6	"	"	"	91	-	100~110	24~27	-	14~15
7	"	"	"	94	-	"	"	-	"
8	"	"	"	98	-	"	"	-	"
9	"	"	"	103	-	"	"	-	"
10	"	"	"	106	-	"	"	-	"
11	"	"	"	110	-	"	"	-	"
12	"	"	"	108	-	"	"	-	"
13	"	"	"	113	-	"	"	-	"
14	"	"	"	120	-	"	"	-	"
15	"	"	"	117	-	"	"	-	"
16	"	"	"	120	-	"	"	-	"
17	"	"	"	121	-	"	"	-	"
18	"	"	"	126	-	"	"	-	"
19	"	"	"	116	-	"	"	-	"
20	"	"	"	114	-	"	"	-	"
21	"	"	"	118	-	"	"	-	"
22	"	"	"	107	-	"	"	-	"
23	"	"	"	113	-	"	"	-	"

보성기업

Test No. : S-Groove

Page : : 1 of 4

Pass Sequence

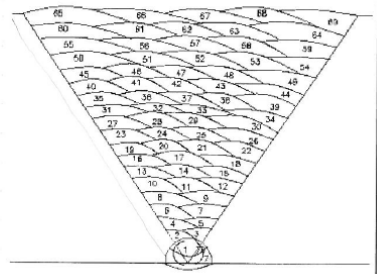

Process	: SMAW
Coupon Size	: t40x400Wx400L
Position	: 1G
Material Spec.	: SA508Gr.3Cl.1+SUS304
Frequency	: N/A
Polarity	: DCRP
Shielding Gas	: N/A
Gas Flow Rate	: N/A
Tungsten Electrode	: N/A
Filler Matal	: WEL DC 182(Nippon Welding)
Flux	: N/A
Welding Engineer	: Y.H.Lee
Welder	: S.W.Sung
Date	: 2013.4.26~4.27

WELDING RECORD OF PROCEDURE QUALIFICATION

시 험 용 접 기 록 서

Test No. : S-Groove

Page : 4 of 4

Pass No.	Filler Metal Type	Heat or Lot No.	Size (Φ)	Temp. Max.(℃)	Peak Amps	Base Amps (A)	Volts (V)	Wire Feeding (cm/min)	Speed (cm/min)	Pass Sequence
70	ENiCrFe-3	K60	3.2	72	-	100~110	24~27	-	14~15	
71	"	"	"	75	-	"	"	-	"	
				이하여백						

Process :

Coupon Size :

Position :

Material Spec. :

Frequency :

Polarity :

Shielding Gas :

Gas Flow Rate :

Tungsten Electrode :

Filler Matal :

Flux :

Welding Engineer :

Welder :

Date :

보성기업

Appendix B Photograph and Drawings of Acrylic Cell

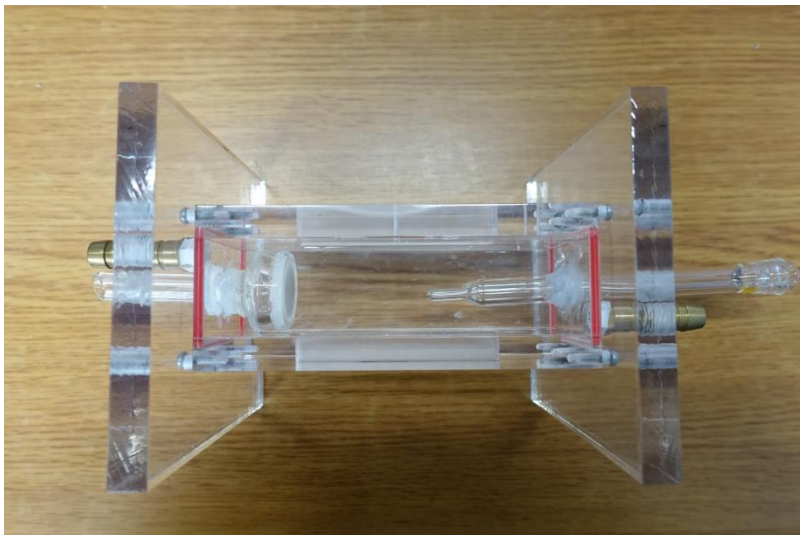

(a)

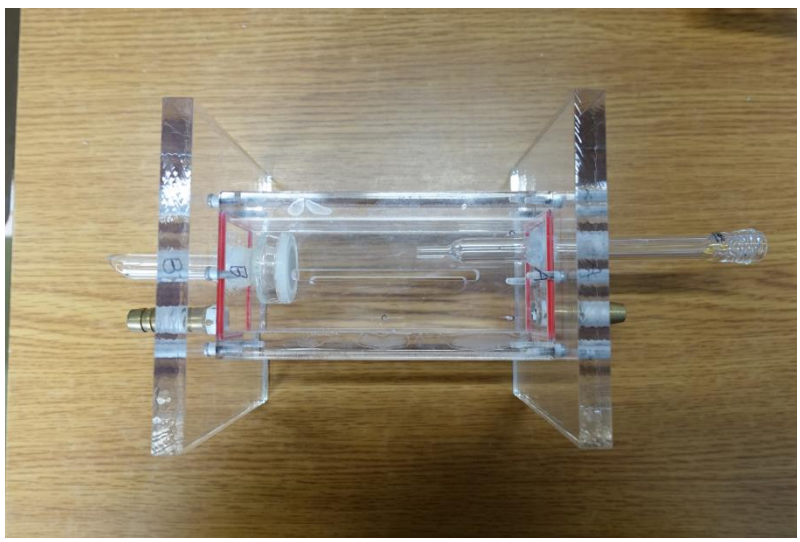

(b)

Figure B.1 Acrylic cell for the fatigue crack growth test: (a) front view and (b) top view.

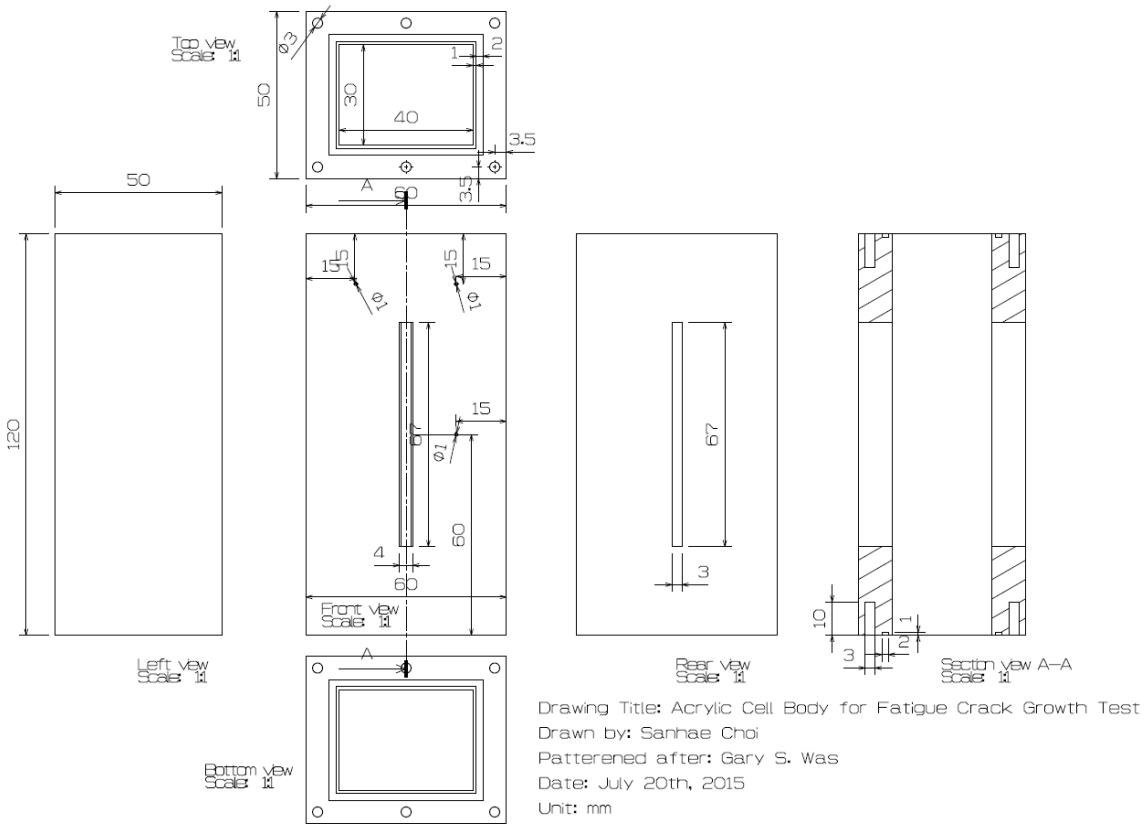

Figure B.2 Drawing of acrylic cell body for fatigue crack growth test.

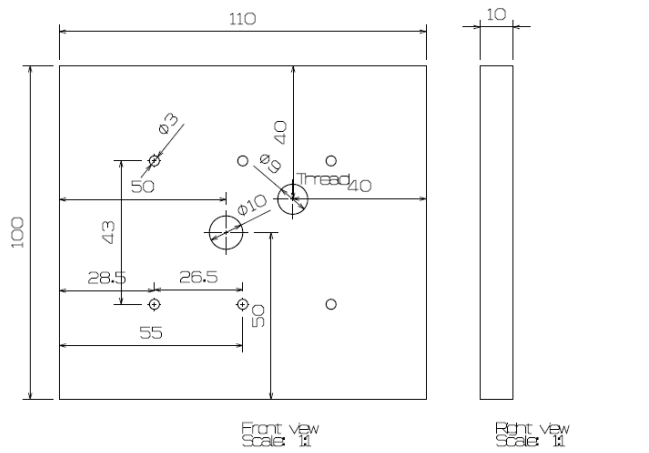

Drawing Title: Acrylic Cell Left Side for Fatigue Crack Growth Test
Drawn by: Sanhae Choi
Patterened after: Gary S. Was
Date: July 20th, 2015
Unit: mm

Figure B.3 Drawing of acrylic cell left side for fatigue crack growth test.

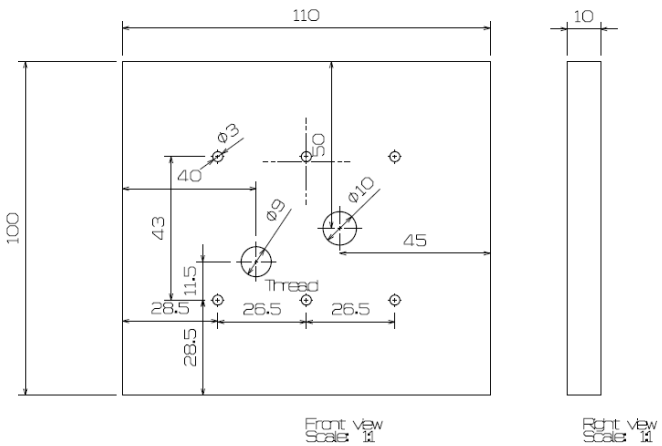

Drawing Title: Acrylic Cell Right Side for Fatigue Crack Growth Test
Drawn by: Sanhae Choi
Patterned after: Gary S. Was
Date: July 20th, 2015
Unit: mm

Figure B.4 Drawing of acrylic cell right side for fatigue crack growth test.

Appendix C Drawings of the Grips, Pins, and Insulation

The bolts that tightened the upper and lower grips were made using alloy 718. To prevent current leakage from the specimen, Teflon® insulation was used between the specimen and the grips.

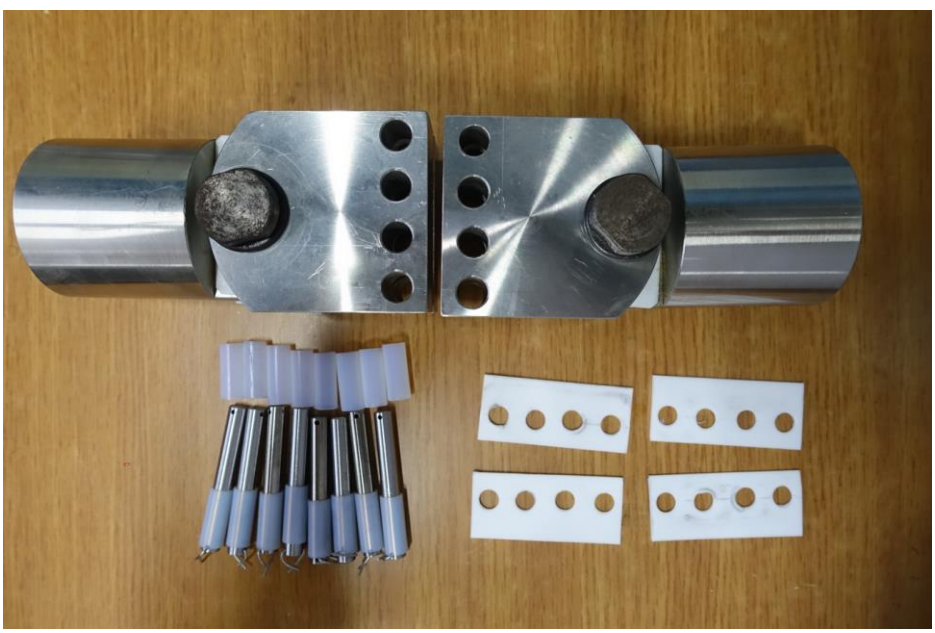

Figure C.1 Photograph of grips, pins, and insulation.

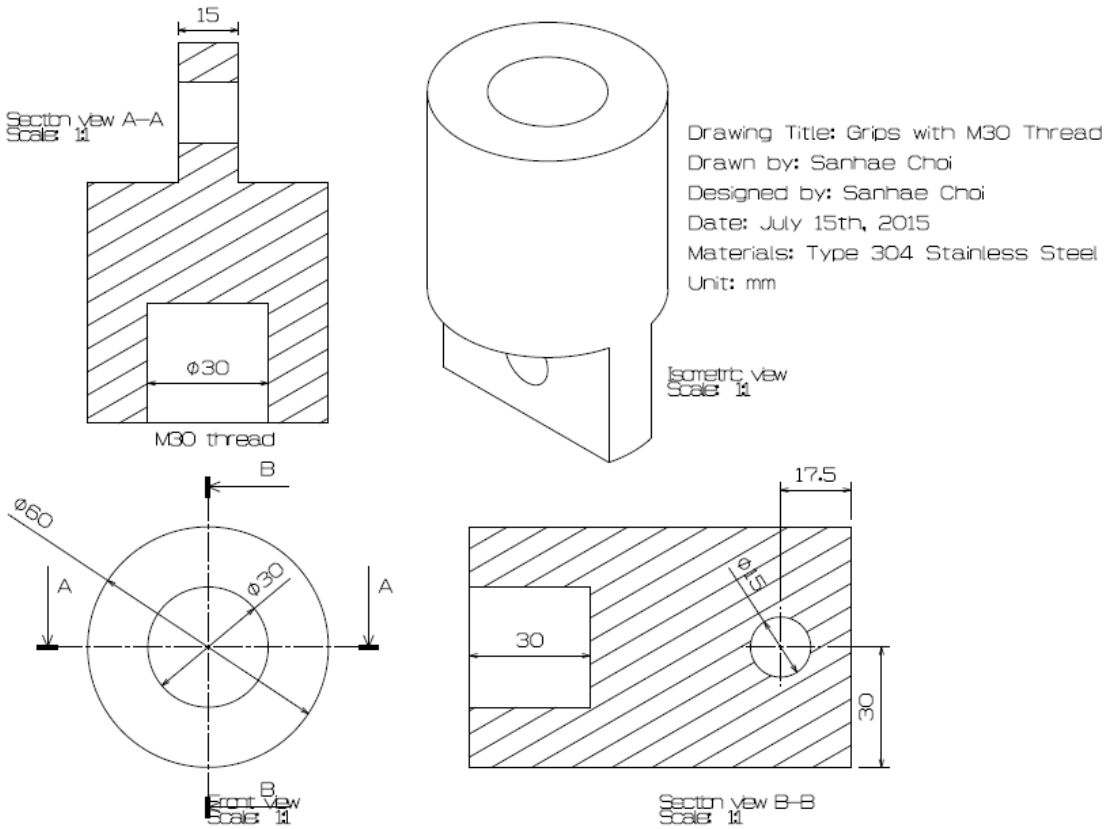

Figure C.2 Grips with M30 threads.

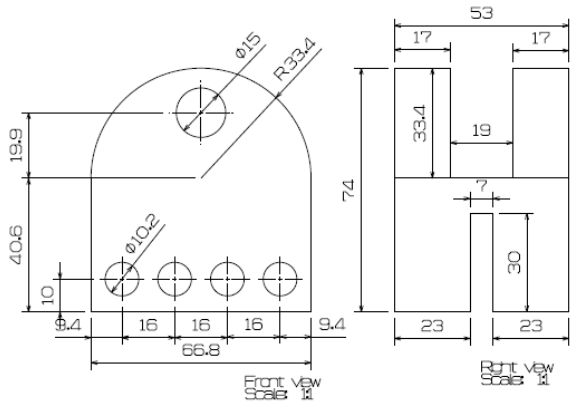

Drawing Title: SEN Specimen Grips
Drawn by: Sanhae Choi
Designed by: Sanhae Choi
Date: July 15th, 2015
Materials: Type 304 Stainless Steel
Unit: mm

Figure C.3 Drawing of SEN specimen grips.

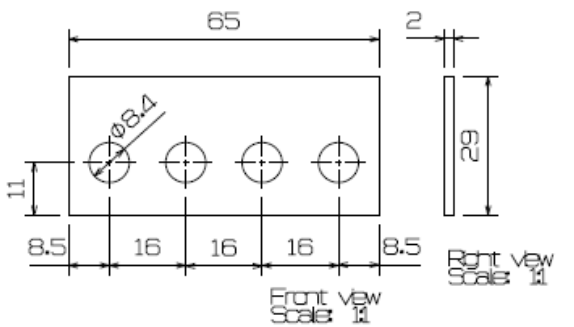

Drawing Title: SEN Specimen Insulation Separator
Drawn by: Sanhae Choi
Designed by: Sanhae Choi
Date: July 15th, 2015
Materials: Teflon
Unit: mm

Figure C.4 Drawing of SEN specimen insulation separator.

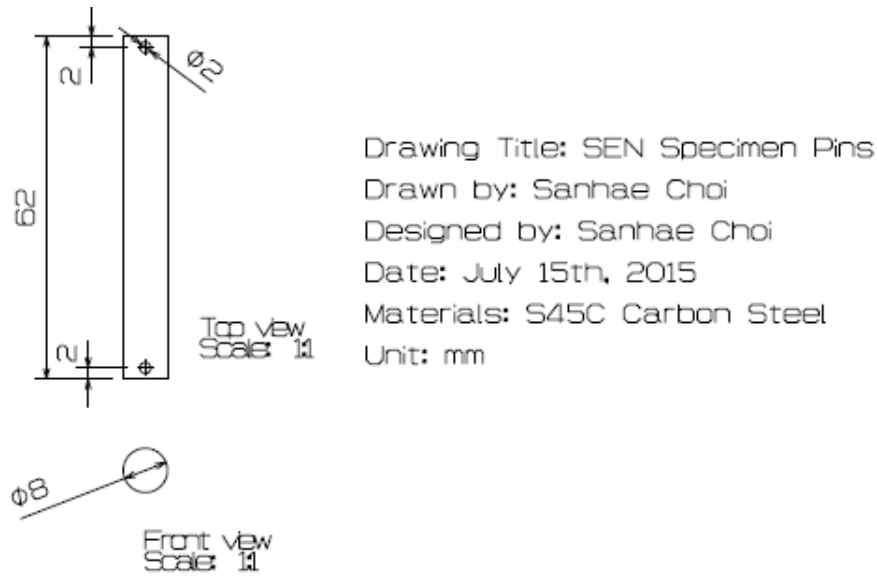

Figure C.5 Drawing of SEN specimen pins.

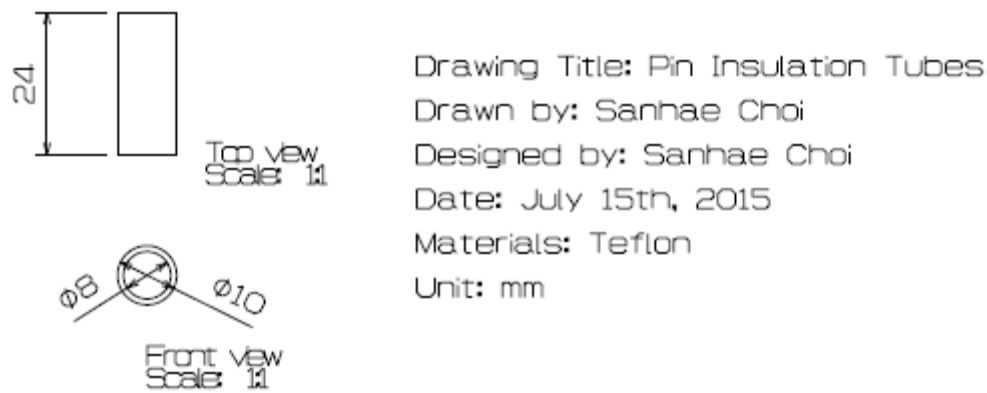

Figure C.6 Drawing of pin insulation tubes.

국문 요약서

앞으로 10년이 지나면, 전 세계 원전의 절반 이상이 설계수명인 40년을 넘게 된다. 따라서 원자력 발전소에 사용되는 재료의 경년열화가 중요한 이슈가 될 것이다. 이에 원자력 발전소에서는 ASME Boiler and Pressure Vessel Code Section XI에 근거한 피로 균열 성장 속도 데이터를 통해 결정론적으로 구한 Paris 법칙을 이용하여 가동 중 검사 시 피로에 대한 원전 구조 재료의 건전성을 평가하고 있다.

원전에서는 경제성을 이유로 압력용기는 저합금강으로 배관은 스테인리스강을 사용하기 때문에 이종 금속 용접부가 많이 사용되고 있다. 용접부는 용접 조건이나 원전 환경에 따라 재료의 기계적 특성이 변하기 쉽다. 특히 이종 금속 용접부 합금 182는 Davis-Besse와 V. C. Summer 원전에서 균열이 발견되기도 했다. 그리고 이 합금은 원전 shutdown 조건인 용존 수소가 존재하고 150℃ 이하의 저온 수화학 환경에서 수소 취화로 인해 파괴인성이 급격하게 감소한다는 것을 실험실 규모의 실험으로 확인된 바 있다.

본 논문에서는 고리 원전 1호기에 사용되는 가압기 밀림관 노즐 용접부를 참조하여 이종 금속 용접부 합금 182를 제작하였다. 이 재료로 피로 균열 성장 속도 실험 시편을 열의 영향을 받지 않도록 하기 위해 electrical discharge machining (EDM) wire cutting 방법으로 제작하였다. 이 시편을 온도가 25℃인 공기 중과 shutdown 조건과 유사한 온도가 54℃이고 음극 분극을 이용하여 대기압 하에서 30 cc H_2/kg H_2O의 용존 수소가 존재하는 저온 수화학 환경을 만들고 일정 하중 피로 균열 성장 속도 실험을 수행하였다. 이 실험을 통해 합금 182 용접부가 수소 취화로 인해 피로 균열 성장 속도가 증가하는 것을 확인하였고 이 데이터를 사용하여 Paris 법칙 상수들을 구하였다.

다음으로 원전 shutdown 조건 하에서 일정 stress intensity factor range (ΔK) 실험을 수행하여 균열 성장에 따른 피로 균열 성장 속도 데이터를 측정하였다. 이 속도 데이터와 Paris 법칙으로 구한 피로 성장

균열 속도와의 차이 값들이 정규분포를 하고 있다고 가정하면 Paris 법칙의 상수 값들에 대한 우도 (likelihood)를 구할 수 있다. 또, 베이지안 추론을 이용하기 위해 Paris 법칙 상수인 C와 m값이 가지고 있는 불확실도를 정규분포로 가정하여 사전 확률분포를 구하였다. 이렇게 정규분포를 가지는 C와 m값들을 몬테칼로 시뮬레이션을 이용해 랜덤 샘플링 하였다. 이렇게 샘플링 된 각각의 상수 값들에 대한 정규화된 우도와 확률밀도를 곱하면 각각의 상수 값들에 대한 사후 확률밀도를 구할 수 있다. 이 사후 확률분포를 통해 상수 값들의 표준편차가 크게 줄어드는 것을 확인할 수 있었다. 즉, 베이지안 추론을 이용한 확률론적 방법으로 Paris 법칙 상수가 가지는 불확실도를 줄일 수 있었다. 이렇게 피로 균열 성장 속도 데이터가 부족한 경우에도 몇 번의 일정 ΔK 실험을 수행하여 상수 값들에 대한 우도를 구할 수 있다면 용접 조건과 주위 환경이 고려되도록 베이지안 추론을 이용해 상수를 업데이트하여 불확실도를 줄일 수 있다.

마지막으로 피로실험의 주파수를 10분의 1로 낮춘 실험을 통해서 주파수가 낮을수록 저온 수화학 환경이 재료 부식에 영향을 더 주어 피로 균열 성장 속도가 더 증가하는 것을 확인할 수 있었다.

본 연구를 통해서 현장 데이터를 통해 Paris 법칙 상수를 구하고 실험실에서 동일한 환경을 조성하여 일정 ΔK 실험을 수행하면 재료의 용접 조건과 주위 환경을 고려한 업데이트된 더 정확한 Paris 법칙 상수를 구할 수 있다는 것을 확인하였다. 따라서 이러한 베이지안 추론을 이용한 확률론적인 방법을 원전 건전성 평가에 도입한다면 피로 균열 성장 속도에 대한 평가를 더욱 정확하게 수행할 수 있을 것이다.

주요어: 이종 금속 용접부 합금 182, 피로 균열 성장 속도, 수소 취화, Paris 법칙, 베이지안 추론, 몬테칼로 시뮬레이션
학 번: 2014-20531